OPTIMIZATION OF ^{129}Xe SPIN-EXCHANGE OPTICAL PUMPING AND APPLICATIONS OF DISSOLVED-PHASE ^{129}Xe IN MAGNETIC RESONANCE

Michael A. Antonacci

A dissertation submitted to the faculty at the University of North Carolina at Chapel Hill in partial fulfillment of the requirements for the degree of Doctor of Philosophy in the Department of Physics and Astronomy.

Chapel Hill
2019

Approved by:

Rosa Tamara Branca

Thomas Clegg

Hugon Karwowski

Jianping Lu

Sean Washburn

ABSTRACT

Michael A. Antonacci: Optimization of ^{129}Xe Spin-exchange Optical Pumping and Applications of Dissolved-phase ^{129}Xe in Magnetic Resonance
(Under the direction of Rosa Tamara Branca)

Improvements in the efficiency of hyperpolarized ^{129}Xe gas produced by spin-exchange optical pumping (SEOP) have opened up exciting new avenues for the application of ^{129}Xe magnetic resonance (MR) spectroscopy techniques. Xenon's inert nature, high solubility in biological materials, and large chemical shift range make it an excellent *in vivo* MR sensor.

Historically, experimental ^{129}Xe polarization values have been well below the theoretical maximum desired for biomedical imaging. In this work, depolarization by Rb nanoclusters and dark Rb vapor during flow-through SEOP of ^{129}Xe is studied with the aid of home-built, ultra-low field NMR and optical spectrometers. *In situ* monitoring of ^{129}Xe polarization and atomic absorption spectroscopy measurements set an upper limit of 8.3×10^{15} cm^{-3} for the density of Rb_2 present in the optical cell during SEOP. Depolarization by dark Rb in the outlet of the cell is also quantified.

Next, the effect of macroscopic susceptibility gradients on the traditional gas-phase referencing method is studied using a human susceptibility model and finite-element analysis calculations. A ^{1}H referencing system is then proposed and demonstrated *in vitro* with high-resolution ^{129}Xe NMR and *in vivo* in rats, which leads to the identification of the origin of previously disputed dissolved-phase ^{129}Xe peaks.

The ^{1}H referencing method is then applied to study the dependencies of the lipid-dissolved ^{129}Xe chemical shift. The lipid-dissolved ^{129}Xe chemical shift is found to be sensitive to triglyceride hydrocarbon chain length and number of double carbon bonds. However, natural variations in composition between human adipose tissue samples do not result in large

variations in ^{129}Xe chemical shift, enabling the calibration of absolute ^{129}Xe MR thermometry in lipids.

Finally, absolute ^{129}Xe MR thermometry is used to study the thermogenesis of brown adipose tissue (BAT) in mice incapable of activating thermogenesis by uncoupling protein 1 (UCP1). Despite UCP1 ablation, an increase of up to 3.0°C is measured in the BAT of these mice following BAT stimulation. The rate of increase in BAT temperature exceeded that of rectal temperature indicating that heat was produced in or very near BAT. These results demonstrate the *in vivo* sensitivity of ^{129}Xe MR thermometry to detect small temperature changes.

For my father,

Jerome Anfio Antonacci.

(1951–2013)

ACKNOWLEDGMENTS

Foremost I would like to thank my advisor, Dr. Rosa Tamara Branca, for her tireless support, instruction, and encouragement throughout my studies. In addition to sharing her knowledge and experience, she gave me the opportunity to grow as an experimentalist, to take chances on exploring new methods, and to learn from failure. Thank you as well to all of my current and former lab mates: Le Zhang, Alex Burant, Drew McCallister, Christian McHugh, and Michele Kelley. It has been an honor to work and study with you!

Thank you as well to my committee members, Dr. Thomas Clegg, Dr. Hugon Karwowski, Dr. Jianping Lu, and Dr. Sean Washburn, for all of your time and helpful feedback throughout the course of this project. None of this work would have been possible without the support of the human imaging and small animal imaging staff at the UNC Biomedical Research Imaging Center and Center for Animal MRI. I would like especially to thank Mr. Jon Frank, whose patient assistance has made much of this work possible. Thank you as well to the staff of the UNC Lineberger Animal Studies Core Facility for their support with the establishment and management of the UCP1-/- and UCP1+/+ mouse colony that was critical to the final stages of this work. I also thank Dr. Karl Koshlap, manager of the UNC Eshelman School of Pharmacy NMR core facility, for his regular support during high resolution NMR experiments.

A number of colleagues from other institutions generously gave of their time and expertise throughout the course of this research. Specifically, many thanks to Dr. Wolfgang Wagner for sharing his engineering and optics expertise. Thank you to Dr. James Wild and Dr. Graham Norquay of the University of Sheffield for helpful discussions while working out our numerical spin-exchange optical pumping model. Also, sincere thanks to Dr. Cynthia Jameson of the University of Illinois at Chicago for helpful discussions on the methodology used for early

spectroscopic measurements of ^{129}Xe chemical shifts. Finally, thank you to Dr. Simone Degan of Duke University for sharing his techniques and expertise with small animal procedures.

Graduate students learn quickly that scientific knowledge is not only hard-won, but also expensive. I would like to acknowledge the financial support of this work by the National Institutes of Health through grant fund R01 DK108231, by Dr. Branca's startup funds, and by a generous Dissertation Completion Fellowship from the Graduate School at the University of North Carolina at Chapel Hill.

I would like to thank especially my parents, the late Jerome and Sheila Antonacci, for their never-tiring love and support. They instilled in me from the beginning the immense value of education and fostered in me a deep curiosity to understand the way things work. I thank also my brother and sister-in-law Jared and Lisa Antonacci for their enthusiasm throughout my studies and their constant support, even in the midst of starting a new life together. Thanks, as well, to my friend and mentor Dr. M. Anis Maize for his help and guidance throughout the course of my undergraduate education and preparation for graduate school.

I express my sincere gratitude for the constant support and prayers of Archabbot Douglas R. Nowicki, O.S.B., Fr. Earl J. Henry, O.S.B., Br. Anthony Kirsch, O.S.B., Fr. Philip M. Kanfush, O.S.B., and all of my Benedictine confreres of Saint Vincent Archabbey. I especially thank Fr. Brian D. Boosel, O.S.B. for his constant encouragement and sound advice throughout the stages of my graduate studies. I also thank these individual monks: Fr. Thomas More Sikora, O.S.B., Fr. Martin Bartel, O.S.B., Fr. Warren Murrman, O.S.B., Br. Elliott Maloney, O.S.B., Fr. Robert Keffer, O.S.B., Br. Hugh Lester, O.S.B., Br. David Kelly, O.S.B., Br. David Carlson, O.S.B., and Fr. Daniel O'Keefe, O.S.B.

It has been a true blessing to share in the life of the local Church while studying here in Chapel Hill. I would especially like to thank Bishop Michael F. Burbidge for his warm welcome to the Diocese of Raleigh and constant support throughout the duration of my studies. I thank as well the priests and deacons of the Diocese of Raleigh for the privilege

of serving alongside you and for your friendship and encouragement. I thank especially Fr. James M. Labosky for his friendship, trustworthy advice, and for making me feel truly at home in Chapel Hill. I sincerely thank Fr. John Kane, Msgr. Jeffrey Ingham, and Deacon Robert Troy, as well, for their friendship and encouragement. To my family in faith, the parishioners of St. Thomas More, I express heartfelt thanks for welcoming me into their community and for their constant prayers. I thank particularly Dr. W. James McCoy, Dr. George Lensing, Dr. Siegfried Wenzel, Dr. and Mrs. Chris and Georgie Clemens, Mr. Roger Petrich, and Drs. Marci and Joel Morganlander.

Finally, I can not help but to give thanks to God who inspired the beginning of this work, sustained it by his grace, and brought it to successful completion.

Ut in omnibus glorifecitur Deus

TABLE OF CONTENTS

LIST OF TABLES

LIST OF FIGURES

LIST OF ABBREVIATIONS

AAS	Atomic absorption spectroscopy
ABS	Acrylonitrile butadiene styrene
AC	Alternating current
ADC	Analog to digital converter
AHCL	Average hydrocarbon chain length
AWG	American wire gauge
BAT	Brown adipose tissue
BW	Bandwidth
CAD	Computer-aided design
CCD	Charge-coupled device
CS	Chemical shift
CSF	Cerebrospinal fluid
CSI	Chemical shift imaging
CT	Computed tomography
DAC	Digital to analog converter
DAQ	Data acquisition
DC	Direct current
DPXe	Dissolved-phase ^{129}Xe
ECG	Electrocardiogram
FDCB	Fraction of double-carbon bonds
FID	Free induction decay
FLASH	Fast low-angle shot
FOV	Field of view
FPGA	Field-programmable gate array
GRE	Gradient echo
HPXe	Hyperpolarized ^{129}Xe gas

HU	Hounsfield units
I/O	Input/Output
IC	Integrated circuit
IP	Intraperitoneal
KO	UCP1-knockout mouse phenotype
LDX	Lipid-dissolved ^{129}Xe
MRI	Magnetic resonance imaging
MRS	Magnetic resonance spectroscopy
NAA	N-acetyl aspartate
NMR	Nuclear magnetic resonance
ppm	Parts per million
PRESS	Point-resolved spectroscopy
PRFS	Proton resonance frequency shift
RBC	Red blood cells
RF	Radio frequency
ROI	Region of interest
RTD	Resistance temperature detector
rLDX	Methylene-referenced lipid-dissolved ^{129}Xe
SC	Subcutaneous
SEOP	Spin-exchange optical pumping
SLM	Standard liters per minute
SNR	Signal to noise ratio
SW	Spectral width
T_1	Longitudinal relaxation time
T_2	Intrinsic transverse dephasing time
$T_2^\star$	Effective transverse dephasing time
T_2'	Transverse dephasing time due to magnetic field inhomogeneities

TE	Echo time
TMS	Tetramethylsilane
TR	Repetition time
TTL	transistor-transistor logic
UCP1	Uncoupling protein 1
VI	Virtual instrument
WAT	White adipose tissue
WT	UCP1 wild-type mouse phenotype
XeMRT	Hyperpolarized ^{129}Xe magnetic resonance thermometry

CHAPTER 1: INTRODUCTION

Since its first demonstration in 1946 by Bloch[1] and Purcell[2], nuclear magnetic resonance (NMR) has developed into a powerful and flexible tool in the laboratory and clinic. NMR spectroscopy has enabled the structural study of molecules in solution and has played an especially important role in deducing the molecular structure of complex proteins[3]. In the clinic, NMR imaging, known as magnetic resonance imaging (MRI) for historical reasons, has enabled *in vivo* 3-dimensional imaging of the human body with good resolution and excellent soft-tissue contrast. Shortly before the first demonstration of MRI in 1973 by Lauterbur[4], Damadian demonstrated that the excellent soft tissue contrast of NMR could be used to differentiate between healthy tissue and tumors[5]. The first *in vivo* image was published shortly thereafter in 1977 by Mansfield and Maudsley[6]. Since then, MRI has become a routine clinical imaging method for a number of applications including the diagnosis of cancerous lesions, surgical planning, and high-resolution anatomical imaging of the brain, to name a few.

1.1 Magnetic Resonance Physics

Fundamentally, magnetic resonance capitalizes on the non-zero nuclear spin of isotopes such as ^{1}H, ^{2}H, ^{13}C, ^{19}F, ^{23}Na, ^{31}P, ^{129}Xe, and others. The most commonly used nuclei are ^{1}H, followed by ^{13}C, because of their abundance in organic molecules and tissues. Each nuclear spin can be characterized by a gyromagnetic ratio (γ) that describes the angular frequency of precession of the nuclear spin when placed in a static magnetic field. The gyromagnetic ratio for some common nuclei used in MRI is given is Table 1.1

Table 1.1: Common isotopes used for nuclear magnetic resonance measurements.

Nucleus	Spin	Natural Abundance (%)	gyromagnetic ratio (MHz/T)
^{1}H	1/2	∼100	42.5763866[7]
^{2}H	1	0.015	6.536[8]
^{13}C	1/2	1.1	10.708[8]
^{15}N	1/2	0.37	−4.317[8]
^{19}F	1/2	∼100	40.078[8]
^{31}P	1/2	∼100	17.251[8]
^{129}Xe	1/2	26.44	−11.7767392[7]

1.1.1 The MR Signal

In practice, single nuclear spins cannot be detected in MR experiments. Instead, in MR experiments we typically measure ensembles of spins in the entire sample (high resolution NMR spectroscopy) or specific volumes or "voxels" within the sample (magnetic resonance imaging and localized MR spectroscopy). Let our sample be composed of an ensemble of N spin-$\frac{1}{2}$ nuclei[1] in a static magnetic field B_0. When an ensemble of spin-$\frac{1}{2}$ nuclei are placed in a magnetic field they will populate two energy levels, one with the spin oriented parallel to the main magnetic field and one with the spin oriented antiparallel to the main magnetic field. For nuclei with a positive gyromagnetic ratio, the parallel configuration is the most favorable one. Polarization is a measure of the difference in population between the upper (antiparallel to field, N_-) and lower (parallel to field, N_+) energy levels given by the Boltzmann distribution, where the probability of a spin being in either state, $P_\pm$, is given by:

$$P_\pm = \frac{e^{\pm\hbar\omega_0/2kT}}{e^{\hbar\omega_0/2kT} + e^{-\hbar\omega_0/2kT}}, \tag{1.1}$$

where $\hbar$ is the Planck constant (6.63×10^{-34} J·s), $\omega_0 = \gamma B_0$ is the nuclear precession (Larmor) frequency, k is the Boltzmann constant (1.38×10^{-23} $\frac{J}{K}$) and T is absolute temperature. The

[1]This semi-classical model does not hold for nuclei with spins $> \frac{1}{2}$; however, since this work is primarily concerned with spin-$\frac{1}{2}$ nuclei, this model will suffice.

polarization can then be expressed in terms of the population difference

$$\Delta N = (N_+ - N_-) = N(P_+ - P_-) = N\left(\frac{e^{\hbar\omega_0/2kT} - e^{-\hbar\omega_0/2kT}}{e^{\hbar\omega_0/2kT} + e^{-\hbar\omega_0/2kT}}\right) = N\tanh\left(\hbar\omega_0/2kT\right). \quad (1.2)$$

For an ensemble of nuclei in a clinical-strength magnetic field (∼1.5 T) the polarization is on the order of 1 ppm. Since the energy separation of the two states $\hbar\omega_0$ is much smaller than the thermal energy kT, the polarization can be well-approximated as

$$N\tanh\left(\hbar\omega_0/2kT\right) \simeq N\hbar\omega_0/2kT. \quad (1.3)$$

The magnetization M_0 of a sample of volume V can then be written as[9]

$$M_0 \simeq \frac{\Delta N\gamma\hbar}{2V} = \frac{N}{V}\frac{\gamma\hbar^2\omega_0}{4kT} = \rho_0\frac{\gamma^2\hbar^2}{4kT}B_0, \quad (1.4)$$

where ρ_0 is the spin density of the sample. Once in the static field, the sample magnetization can be manipulated, in whole or in part, to give rise to the MR signal. The maximum MR signal amplitude ξ that can be obtained from the magnetization M_0, assuming a uniform excitation field B_1 perpendicular to B_0, is then given by[9, 10]

$$\xi = \omega_0 B_1 M_0 V. \quad (1.5)$$

In general, then, since both ω_0 and M_0 are proportional to B_0, the signal strength is proportional to B_0^2.

In a real MR experiment, the measured signal will always be contaminated with a minimum amount of thermal noise from the pickup coil given by[11]

$$\xi_{noise} = \sqrt{4kT \cdot BW \cdot R}, \quad (1.6)$$

where BW is the receiver bandwidth and R is the resistance of the coil. Because of the skin effect of AC signals, the resistance of an MR coil will have a dependence on frequency[9, 11]:

$$R \propto \sqrt{\omega_0}. \tag{1.7}$$

As a result, the signal-to-noise ratio (SNR) for thermally polarized nuclei scales as[9]:

$$SNR = \frac{\xi}{\xi_{noise}} = \frac{\omega_0 B_1 M_0 V}{\sqrt{4kT \cdot BW \cdot R}} \propto \frac{B_0^2}{B_0^{\frac{1}{4}}} \propto B_0^{\frac{7}{4}}. \tag{1.8}$$

1.1.2 The Resonance Condition

A large proportion of magnetic resonance experiments can be completely explained by the classical treatment of a magnetic moment of magnitude M_0 precessing in a static magnetic field. The magnetization vector $\vec{M}_0$ is nothing else than the sum of the individual nuclear spin magnetic moments in our sample. The evolution of the magnetization vector in a magnetic field $\vec{B}$ is described by the Bloch equation:

$$\frac{d\vec{M}_0}{dt} = \gamma \vec{M}_0 \times \vec{B}. \tag{1.9}$$

Now consider the same magnetization $\vec{M}_0$ in a static magnetic field with magnitude B_0 oriented along $\hat{z}$ as shown in Figure 1.1. At equilibrium, the magnetization vector aligns with the static external field $\vec{B_0}$ (*i.e.* $d\vec{M}_0/dt = 0$). However, if we perturb the magnetization vector out of equilibrium (Figure 1.2), Equation (1.9) tells us that the magnetization vector will always precess around the applied magnetic field with a frequency given by

$$\omega_0 = -\gamma B_0. \tag{1.10}$$

At equilibrium, however, when $\vec{M}_0$ is aligned along $\vec{B_0}$, no precession exists. In order to perturb the magnetization, we will need to apply a magnetic field orthogonal to the direction

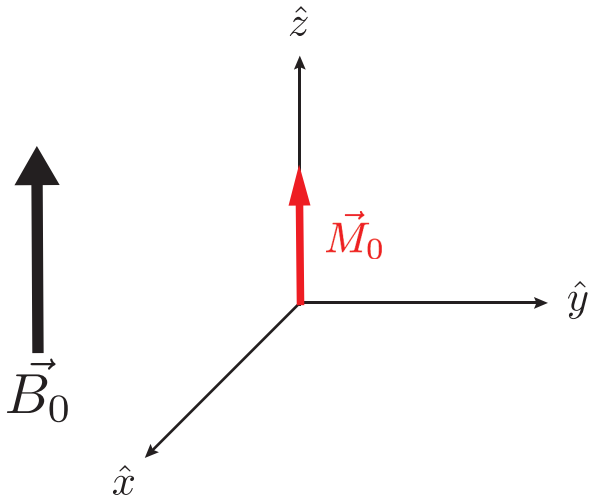

Figure 1.1: The net magnetization vector $\vec{M}_0$ aligns with the static field $\vec{B}_0$.

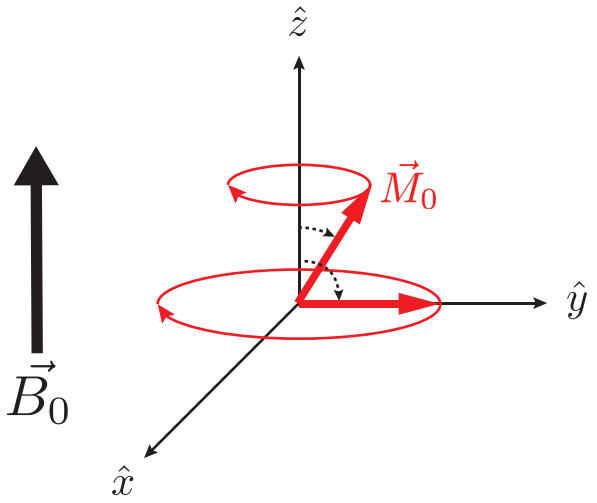

Figure 1.2: A perturbed net magnetization $\vec{M}_0$ will precess about the static field $\vec{B}_0$ with frequency ω_0.

of the polarizing field $\vec{B_0}$. This can be accomplished by applying a linearly polarized $\vec{B_1}$ field with a characteristic frequency ω in the $\hat{x}$-$\hat{y}$ plane. The linearly polarized $\vec{B_1}$ field can then be decomposed into two counter-rotating circularly polarized fields. The component of $\vec{B_1}$ rotating in the same direction as $\vec{M_0}$ will be effective at producing a rotation of the $\vec{M_0}$ magnetization. For convenience, we can look at the precession of the magnetization in a reference frame that rotates around $\vec{B_0}$ with a frequency ω. The $\hat{x}'$ and $\hat{y}'$ coordinates of this new frame of reference, called "the rotating frame of reference", are

$$\hat{x}' = \hat{x}\cos\omega t - \hat{y}\sin\omega t \tag{1.11}$$

and

$$\hat{y}' = \hat{x}\sin\omega t + \hat{y}\cos\omega t. \tag{1.12}$$

In the rotating frame, the expression of the applied field B_1 simplifies to

$$\vec{B_1}(\omega) = B_1\hat{x}'. \tag{1.13}$$

In other words, in the rotating frame the magnetization vector only sees the applied field B_1 and the precession of the magnetization can be described by:

$$\left(\frac{d\vec{M_0}}{dt}\right)' = \vec{M_0} \times (\hat{z}(\omega_0 - \omega) + \hat{x}'\omega_1) = \gamma\vec{M_0} \times \vec{B}_{eff} \tag{1.14}$$

where $\omega_1 \equiv \gamma B_1$ and $\vec{B}_{eff}$ is the effective magnetic field applied to the ensemble. Now we can write the effective applied field in general as

$$\vec{B}_{eff} = \frac{1}{\gamma}[\hat{z}(\omega_0 - \omega) + \hat{x}'\omega_1]. \tag{1.15}$$

The forms of Equation (1.14) and Equation (1.15) beg the question: what if the frequency of the applied field is equal to the Larmor frequency ω_0? In this case, the effective field

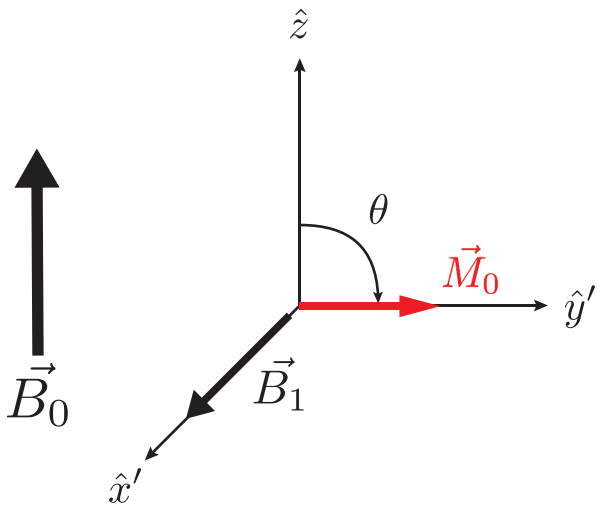

Figure 1.3: Depiction of the magnetization $\vec{M}_0$ being tipped into the transverse plane by applied field $\vec{B}_1$.

reduces to

$$\vec{B}_{eff} = \frac{\hat{x}'\omega_1}{\gamma} \tag{1.16}$$

and the change in orientation of the magnetization $\vec{M}_0$ simplifies to

$$\left(\frac{d\vec{M}_0}{dt}\right)' = \omega_1 \vec{M}_0 \times \hat{x}'. \tag{1.17}$$

Thus in the rotating frame of reference, when the magnetic field is applied at the Larmor frequency of the nucleus, the magnetization vector is most efficiently tipped into the $\hat{x}'$-$\hat{y}'$ plane, as shown in Figure 1.3. The angle θ of the magnetization, relative to $\vec{B}_0$, is commonly referred to as the B_1 flip angle.

1.1.3 Relaxation Mechanisms

After the magnetization vector has been perturbed from equilibrium and transferred to the $\hat{x}'$-$\hat{y}'$ plane, the magnetization vector in the $\hat{z}$ direction, $M_z(t)$, gradually grows according to

$$M_z(t) = M_0\left(1 - e^{-\frac{t}{T_1}}\right), \tag{1.18}$$

where T_1 is the intrinsic longitudinal relaxation time constant[8]. The magnitude of T_1 depends heavily on the molecular structure and motion surrounding the nucleus of interest. Roughly, if the motion of the molecule containing the nucleus of interest is such that magnetic interactions occur at a frequency similar to the Larmor frequency of the nucleus, T_1 tends to be shorter[12]. As the molecular motion gets faster or slower, say with change of temperature or a phase change, T_1 will tend to increase in general. However, the complicated dependence of T_1 on such factors as diffusion rate and nearest-neighbor interactions goes beyond the scope of this work.

Once tipped into the transverse plane, the spins in the ensemble will also begin to precess at slightly different frequencies due to inhomogeneities in the local magnetic field produced by the presence of nearby spins[10]. The loss in spin phase coherence results in a decrease in the M_x and M_y components of the magnetization vector that can be described by:

$$M_x = M_0 \sin(\omega_0 t) e^{-\frac{t}{T_2}} \tag{1.19}$$

and

$$M_y = -M_0 \cos(\omega_0 t) e^{-\frac{t}{T_2}}, \tag{1.20}$$

where T_2 is the intrinsic transverse relaxation time constant.

In addition to the intrinsic T_2 relaxation, further relaxation contributions come from inhomogeneities in the external magnetic field. For example, at the interface of two materials with different magnetic susceptibilities, like fat and muscle, magnetic susceptibility gradients distort the homogeneity of the external magnetic field. These field inhomogeneities shorten the time during which spins precess coherently since spins at different positions "see" very different magnetic fields. Relaxation contributions from such inhomogeneities are characterized by a separate relaxation time T_2' that combines with T_2 to give an effective transverse relaxation time $T_2^\star$ given by

$$\frac{1}{T_2^\star} = \frac{1}{T_2} + \frac{1}{T_2'}. \tag{1.21}$$

Dephasing caused by external field inhomogeneities can be recovered by carefully designed RF pulse sequences[13, 14], whereas the dephasing caused by intrinsic interactions usually cannot. It is important to clarify that the difference between T_2 and T_2' is often very subtle and in general depends on the time scale that one is investigating. Indeed, some of the dephasing mechanisms that characterize T_2 could also be refocused with an appropriately designed pulse sequence. In general, however, the differentiation between the two is made between contributions that can be refocused and those that cannot. The relaxation rates $R_2^\star$, R_2, and R_2' are simply the inverse of the corresponding relaxation times.

1.2 Spin Exchange Optical Pumping of ^{129}Xe Gas

Most magnetic resonance experiments are performed using ^{1}H nuclei since the MR signal from less abundant nuclei is weak. In recent years, to compensate for the low density of some nuclei, various hyperpolarization techniques have been devised. Hyperpolarization increases the spin population difference (Equation (1.2)) and hence the resulting MR signal. This enables measuring nuclei that would otherwise not be detected. For gases, the most common polarization mechanism is spin-exchange optical pumping (SEOP). With SEOP polarization levels 5 orders of magnitude higher than those given by Boltzmann polarization are made possible by transferring the polarization of laser light to an alkali vapor (optical pumping), which in turn transfers atomic polarization to ^{129}Xe nuclear polarization through spin-conserving collisions (spin exchange). In this section, we review the fundamental physics of spin exchange optical pumping (SEOP) and outline the hardware typically used to accomplish continuous-flow SEOP in the lab. For a detailed treatment of the most general cases of optical pumping and spin exchange physics, see Refs. [15] and [16].

1.2.1 Depopulation Optical Pumping of Alkali Metal Vapors

Spin-exchange optical pumping begins with a saturated alkali vapor contained within an optical cell and placed in a magnetic field oriented along the $\hat{z}$ direction. The atomic

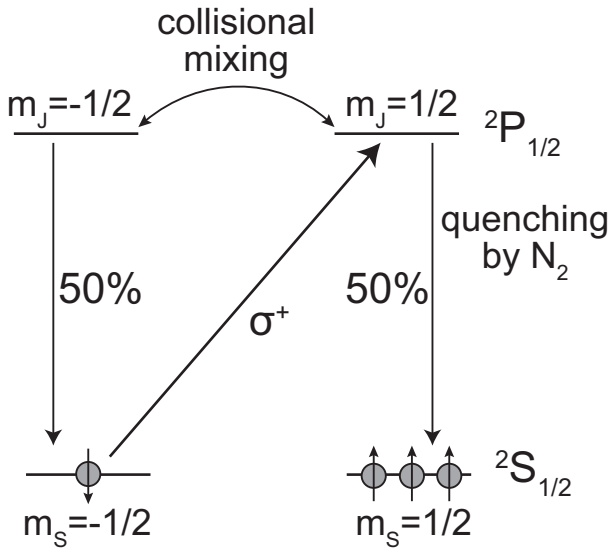

Figure 1.4: Diagram of the relevant energy levels of Rb atoms during SEOP processes.

Hamiltonian can then be written as[16, 17]

$$H_a = A_a \mathbf{I}_a \cdot \mathbf{S} + g_s \mu_B S_z B_0 - \frac{\mu_a}{I_a} I_{az} B_0, \tag{1.22}$$

where A_a is the magnetic dipole coefficient, $\mathbf{I}_a$ is the alkali nuclear spin quantum number, $\mathbf{S}$ is the alkali valence electron spin, g_s is the electronic g-factor, μ_B is the Bohr magneton, S_z is the projection of the electronic spin along the static field B_0, μ_a is the nuclear magnetic moment, and I_{az} is the projection of the nuclear spin along the external magnetic field. In most SEOP setups, the static field is relatively small such that the Zeeman effect is small compared to the hyperfine interaction. Furthermore, a small amount of He buffer gas is added to the cell in order to pressure-broaden the atomic absorption line widths, leaving the hyperfine energy level splitting unresolved. The resulting energy levels are depicted in Figure 1.4.

The first step in a SEOP setup is to polarize the valence electron of the alkali metal atoms using laser light, *i.e.* to force all of the alkali metal atoms into the same $^2\mathrm{S}_{1/2}$ spin state and generate the maximum polarization possible. This can be accomplished by illuminating the Rb vapor with left-handed circularly polarized laser light (σ^+) tuned to the $^2\mathrm{S}_{-1/2} \rightarrow ^2\mathrm{P}_{1/2}$

atomic transition of the alkali metal. Obeying selection rules, the atom absorbs the spin-1 photon and makes a transition to the spin-up excited state $^2P_{1/2}$. Left to its own devices, the alkali atom would relax back to ground state and emit a photon with a random polarization that could in turn be absorbed by another alkali atom. This process can lead to radiation trapping [18–21] that spoils the alkali polarization. Typically, N_2 gas is also placed in the cell in order to quench the alkali excited state without re-emission of a photon. At the same time, alkali atoms collide with noble gas atoms, mixing the excited state sublevels and resulting in an equal probability that an optically excited photon will return to either ground state. Since the $^2S_{-1/2}$ sublevel is being actively depopulated, the final result is that nearly all of the alkali atoms are rapidly polarized into the $^2S_{1/2}$ sublevel.

For ^{129}Xe polarization, optical pumping is typically accomplished with Rb vapor since it has a D1 transition at 794.7 nm that is well separated from other atomic transitions[15] and for which high-power light sources are readily available (*e.g.* dye lasers[16, 18] and, more commonly, laser diode arrays [22–30]).

1.2.2 Spin Exchange

The second stage of SEOP, spin exchange, is responsible for transferring the optically-pumped Rb vapor polarization to the ^{129}Xe nuclei. In general, the spin exchange interaction can occur through Rb atoms binding to ^{129}Xe in either van der Waals molecules or in binary collisions. For typical continuous-flow SEOP polarizers, gas pressures are high enough (> 1 atm) to make the collisional lifetime of van der Waals interactions short to the point where they contribute only negligibly to spin relaxation processes[16].

The spin-dependent interactions $V_1(R)$ responsible for polarization transfer between Rb and ^{129}Xe depend strongly on R, the interatomic separation of Rb and ^{129}Xe atoms, and are typically denoted in the literature by

$$V_1(R) = \gamma(R)\mathbf{N}\cdot\mathbf{S} + A_b(R)\mathbf{I}_b\cdot\mathbf{S}, \tag{1.23}$$

where the first term describes the spin-rotation interaction between the Rb valence electron spin and the rotational angular momentum $\mathbf{N}$ of the Rb-^{129}Xe atomic pair and the second term is the isotropic hyperfine interaction between the Rb valence electron spin and the ^{129}Xe nuclear spin $\mathbf{I}_b$. The constant $A_b(R)$ gives the strength of the isotropic hyperfine interactions and hence of the spin-exchange process. The strength of the spin-rotation interaction, which is responsible for decreasing spin-exchange efficiency by transforming the Rb valence electron polarization into translational motion of the atoms rather than ^{129}Xe nuclear polarization, is given by the constant $\gamma(R)$.

1.2.3 The Continuous-flow SEOP Polarizer

A typical continuous-flow SEOP polarizer arrangement is depicted in Figure 1.5. A lean gas mixture of 1% xenon, 10% N_2, and 89% He flows into a presaturation region heated above oven temperature that contains a relatively large amount of Rb (> 1 g). The gas mixture, ideally, will be fully saturated with Rb vapor and flow a short distance into the optical pumping cell. The optical cell is located within a pair of Helmholtz coils that provide a weak ($\sim$20 G) magnetic field needed for optical pumping and serve as the B_0 for NMR measurements of ^{129}Xe polarization. The optical cell is maintained at a constant temperature by a forced-air heater and temperature controller that warms the entire oven enclosure.

Once the gas mixture enters the optical cell, it is illuminated by left-handed circularly polarized pumping laser light tuned near the Rb D1 transition and directed counter to the gas flow direction. After polarization by SEOP, the polarized ^{129}Xe and buffer gases exit the cell and flow towards the cold finger. The cold finger is submerged in liquid N_2 resulting in the cryogenic collection of polarized xenon and free flow of the rest of the buffer gases out the vent. When cryogenic collection is completed, the vent is closed and the liquid N_2 replaced with warm water, which will sublime solid xenon into gas.

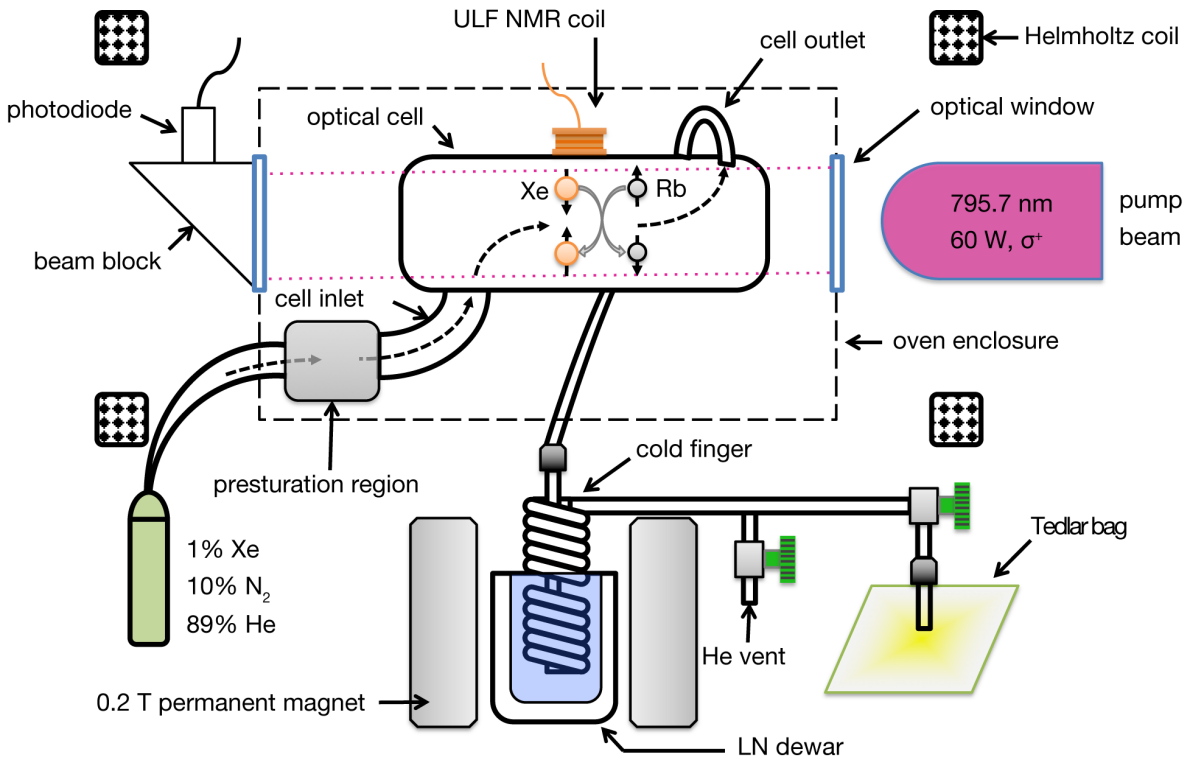

Figure 1.5: Block diagram of the continuous-flow spin-exchange optical pumping ^{129}Xe polarizer.

1.3 Overview of Contents

Overall, this work seeks to understand current limitations in the continuous-flow SEOP process in order to improve final ^{129}Xe polarization efficiency. A higher polarization efficiency means more available ^{129}Xe MR signal, and thus the capacity to utilize ^{129}Xe as a powerful *in vivo* probe.

Chapter 2 presents details of the current limitations of continuous-flow SEOP and the discrepancy between theoretical and experimental polarization values reported in the literature. To address these limitations and better understand the origin of the SEOP inefficiency, ultra-low field NMR and optical spectrometers are designed and constructed in order to enable monitoring of ^{129}Xe polarization and Rb vapor density *in situ*. A complete description of the various components is given in this chapter.

In Chapter 3 of this work, the hardware described in the previous chapter is used to study some of the depolarizing mechanisms present during SEOP. First, broadband atomic absorption spectroscopy measurements are performed in the polarizer optical cell during polarization in order to search for the characteristic absorption band of Rb dimers, which have been proposed as an explanation for sub-optimal ^{129}Xe polarization during continuous-flow SEOP. Secondly, a combination of *in situ* ^{129}Xe NMR measurements on the optical cell outlet are used to measure the effect of un-illuminated Rb vapor (dark Rb) on the final ^{129}Xe polarization.

Chapter 4 begins with a brief introduction to the origin and practical utility of the chemical shift in NMR spectroscopy. Then, it outlines some of the problems associated with the conventional reference standard for ^{129}Xe NMR spectroscopy. Specifically, for ^{129}Xe NMR spectroscopy the reference standard is the gas phase frequency, which, by residing in a different tissue/organ compartment, typically experiences a different local magnetic field than dissolved-phase frequencies. This inherently leads to large variations in the apparent chemical shift of dissolved-phase ^{129}Xe resonances. These variations are quantified by computing the effect of magnetic susceptibility gradients on the ^{129}Xe frequencies in the human head and

torso. We then propose and validate a novel method for referencing dissolved-phase ^{129}Xe frequencies that takes advantage of the local ^{1}H spins to remove the effect of macro- and microscopic susceptibility gradients, while retaining chemical shift information.

The referencing system described in Chapter 4 is of general applicability and is used in Chapter 5 to better understand the dependence of a specific ^{129}Xe resonance frequency observed in *in vivo* experiments, the lipid-dissolved ^{129}Xe (LDX) frequency, on temperature and on triglyceride saturation and hydrocarbon chain length. An absolute LDX frequency/temperature relation is also found that enables us to determine tissue absolute temperature *in vivo* by hyperpolarized ^{129}Xe NMR.

In Chapter 6 we use the temperature dependence of LDX to measure temperature *in vivo*. Temperature, one of the most important physical properties of matter, is extremely hard to measure non-invasively *in vivo*. Yet, non-invasive absolute thermometry would be invaluable for a variety of applications, ranging from cancer treatment of tumors to measuring increased metabolic activity in tissues. For tissues like brown fat, absolute temperature measurements would represent the most direct way to measure the activity of this tissue, and to determine whether there exist other non-shivering thermogenesis mechanisms that are independent of the uncoupling protein one. In this chapter, we demonstrate how the hyperpolarized ^{129}Xe absolute thermometry method can help to answer this question, which has been a matter of debate for the past 20 years.

Finally, a concise summary of the work accomplished and contributions to the field of dissolved-phase ^{129}Xe MR is given, and future applications of dissolved-phase ^{129}Xe MR are discussed.

CHAPTER 2: SEOP LIMITATIONS & CONSTRUCTION OF ULTRA LOW FIELD NMR & OPTICAL SPECTROMETERS

2.1 Limitations of SEOP

Although, at the fundamental level, the theory of continuous-flow SEOP is well understood, in practice it is very difficult to achieve the theoretical maximum ^{129}Xe polarization for a given set of continuous-flow polarizer parameters. A number of possible explanations have been provided to justify the discrepancy between theoretical and experimental polarization values.

Driehuys, *et al*. [19] demonstrated the use of ^{4}He to pressure-broaden the Rb absorption line without unacceptably high depolarization from the presence of a high density of ^{129}Xe. Despite producing a relatively large volume of hyperpolarized ^{129}Xe (500 ml), a polarization of only 5% was attained where theory predicted 60%. They also reported lower-than-predicted Rb polarization as a result of pump beam nonuniformity that left parts of the optical cell poorly illuminated, highlighting the difficulty of collimating the pump beam to illuminate the entire optical pumping region. Further damage is done to the Rb polarization if the direction of the pump laser light propagation is skewed relative to the magnetic field within the optical cell. Chann, *et al*. [31] studied these skew light effects and found that, since efficient optical pumping requires that the electric field of the pump laser light be perpendicular to the static magnetic field, any skew of the angle would result in the sharp increase of optical absorption and decreased optical pumping efficiency over the entire length of the cell. For example, they observed that for a 5 cm long optical cell heated to 180°C a 15 W pump laser would be attenuated by half with a skew of only 3.1°.

Schrank, *et al.* [26] employed a long (> 1 m) optical cell design, similar to the one previously introduced by Ruset, *et al.* [32], along with a low xenon partial pressure and 30 W of spectrally narrowed laser light to optimize the Rb polarization, which ultimately sets the upper limit of ^{129}Xe polarization. Even under conditions that optimized the Rb polarization to 85% – 95% along the length of the cell, experimental values of ^{129}Xe polarization were still half of those predicted experimentally[26]. Work by Norquay, *et al.* [33] observed the same two-fold discrepancy between theory and observations.

Because of the flow of relatively cool noble gas into heated Rb pools in the presaturation region of many continuous-flow ^{129}Xe polarizer designs, Freeman, *et al.* [34] hypothesized that the presaturated Rb vapor contained paramagnetic Rb nanoclusters that could spoil Rb polarization and relax polarized ^{129}Xe atoms. When incorporated into the standard SEOP model, these effects provided an explanation for the discrepancy between theoretically predicted and experimentally observed ^{129}Xe polarization; however, experimental observation of the offending Rb clusters, in the Rb vapor, *in situ*, had not yet been accomplished.

Finally, a number of studies have also focused on the gas flow path after the optical pumping cell as a possible location for ^{129}Xe depolarization. Norquay, *et al.* [33] examined the relaxation of the frozen hyperpolarized ^{129}Xe snow as a function of time and found that the storage conditions in the cold finger lead to a T_1 of about 87 minutes, shorter than previous measurements in the solid state[35, 36], but long enough to result in a polarization loss of only about 10% of the final polarization during a typical 40 minute collection time. Burant, *et al.* [37] studied ^{129}Xe depolarization via diffusion through strong magnetic field gradients that can exist in some continuous-flow polarizers between the relatively weak optical pumping magnetic field and the strong magnetic field used to maintain the polarization of frozen ^{129}Xe during cryogenic collection. While the diffusion of polarized ^{129}Xe gas through strong magnetic field gradients was shown to be a major relaxation mechanism in previous polarizer designs, removal of these strong gradients from the ^{129}Xe flow path did not bring the measured ^{129}Xe polarization into agreement with the predicted theoretical maximum.

As a result, with the exception of the Rb cluster theory, which has not found experimental confirmation, a full explanation of continuous-flow SEOP inefficiency still does not exist.

For this project our goal was to search for experimental evidence of Rb clusters in the Rb vapor and quantify the effect of dark Rb on the final ^{129}Xe polarization. For these studies, which required *in situ* absorption and NMR spectroscopic measurements, a custom ultra-low field NMR spectrometer and a custom optical spectrometer were designed and constructed.

2.2 Ultra-low Field NMR Spectrometer

The custom ultra-low field NMR spectrometer designed and constructed in this work, utilizing a LabVIEW interface (National Instruments Corporation, Austin, TX, USA) and off-the-shelf components, is a modified version of previous low-field designs[38–41]. For simplicity, external hardware and circuitry were kept to a minimum. We took advantage of many built-in features of a National Instruments PCI-6110 multifunction data acquisition (DAQ) board, such as simultaneous analog and digital input/output, external triggering, and programmable dynamic range. A block diagram of the spectrometer is given below in Figure 2.1.

2.2.1 Timing Circuit

Most timing functions used for NMR can be programmed via the DAQ card onboard clock. One notable exception in this implementation is the ability to time precisely the acquisition delay after the excitation pulse. Since the PCI-6110 digital inputs and outputs cannot be hardware timed or triggered via the onboard clock, it is necessary to build an external circuit that precisely times the acquisition delay and triggers the DAQ analog input. The best solution is a straightforward circuit using an SE555P timer (Texas Instruments, Dallas, TX, USA) running in monostable pulse mode as shown in Figure 2.2. A digital potentiometer DS1804 (Maxim Integrated, San Jose, CA, USA) and 0.01 μF electrolytic capacitor determine the monostable pulse length of the 555 timer. The digital outputs of

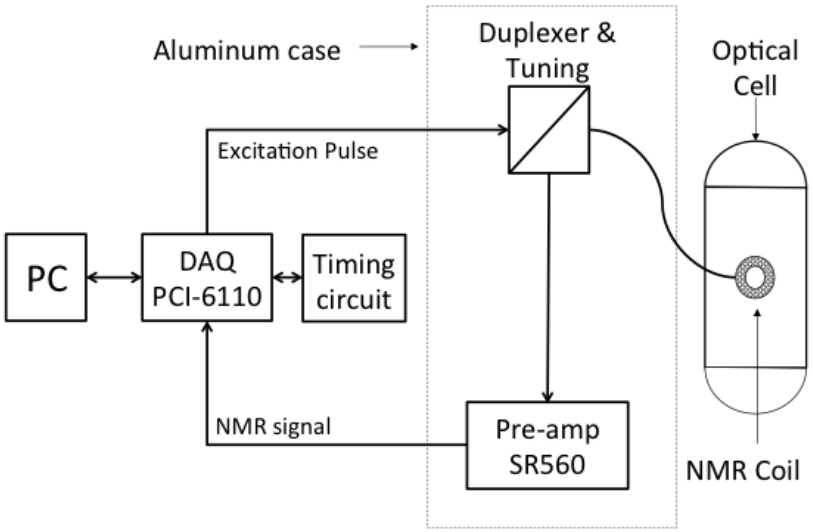

Figure 2.1: Block diagram of the ultra-low field NMR spectrometer. The excitation pulse and NMR signal are carried by shielded BNC cables.

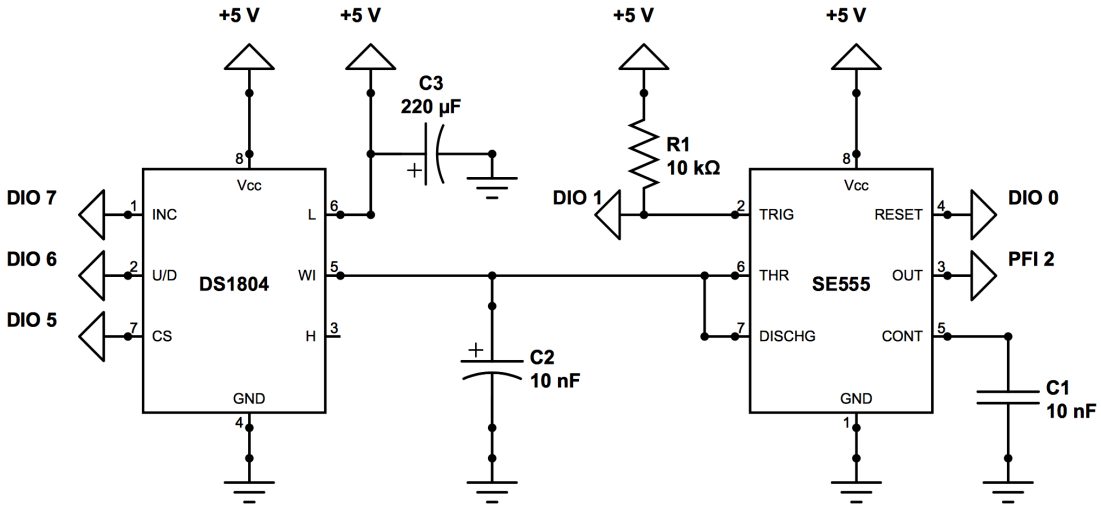

Figure 2.2: Diagram of the spectrometer timing circuit. The DS1804 digital potentiometer and SE555P timer integrated circuits (ICs) are controlled remotely by the DAQ card digital input/output ports (DIOs) and programmable function input/outputs (PFIs). Power is supplied by an external 5 V source and the ICs are grounded to the DAQ card digital ground. The monostable pulse length is given by 1.1RC2, where R is the resistance of the DS1804 potentiometer.

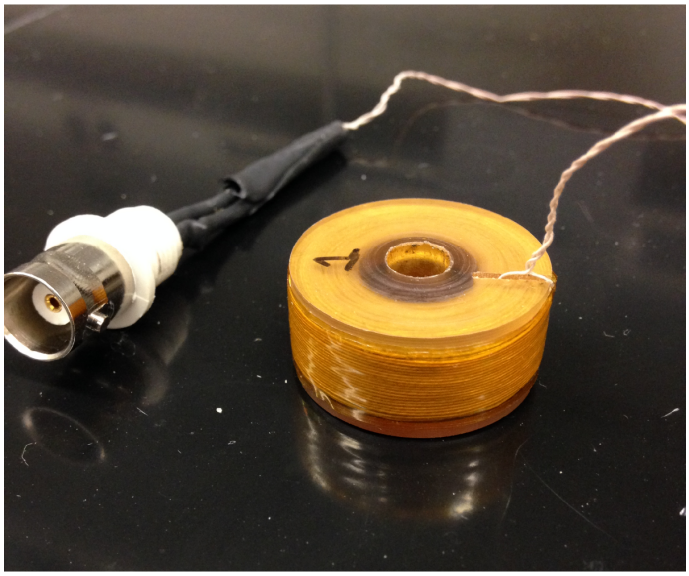

Figure 2.3: Photograph of the final NMR surface coil design. The coil form was machined out of Ultem plastic and wound with 550 turns of 32 AWG 15/44 Litz wire to an average diameter of 2 cm and height of 1 cm. Kapton tape secures the coil windings for higher-temperature applications, such as monitoring ^{129}Xe polarization during spin-exchange optical pumping.

the DAQ card allow direct control of both the 555 timer and the digital potentiometer via LabVIEW. Conveniently, digital outputs programmed on the same channel initialize within 1 ns of each other providing a t = 0 point for timing the rest of the spectrometer functions. In order to stabilize the timing components thermally, the timing circuit is mounted inside an aluminum box. An external power supply drives the integrated circuits with +5 V. We connect the circuit through the box with simple isolated screw mounts that allow for easy disconnect and transport.

2.2.2 NMR Surface Coil

While the literature contains some details regarding the design of low-field MRI volume coils[42–45], low-field surface coil designs still have not been studied systematically. Low-field spectroscopy coil designs present different challenges than traditional high-field spectroscopy probes. While the major source of noise at high field is body noise, at low field losses are negligible and coil resistance dominates as the primary source of noise [10].

More quantitatively, the Johnson noise of the coil-sample system is given by[46]:

$$V_{RMS,\ noise} = \sqrt{4kT \cdot R \cdot \Delta f} \tag{2.1}$$

where k is the Boltzmann constant, T is the absolute temperature of the system, Δf is the receiver bandwidth, and $R = R_c + R_s$ is the effective resistance of the coil-sample system consisting of R_c, the coil DC resistance, and R_s, the effective resistance due to the sample loading. At our operating frequency of ∼25 kHz, R_s is negligible, leaving R_c as the dominant noise contribution. To minimize this noise, and hence maximize the signal to noise ratio (SNR), the use of Litz wire is also crucial[38, 41]. Furthermore, the final SNR of the coil also depends on the uniformity and tightness of the coil turns. The final surface coil design, shown in Figure 2.3, consists of 550 turns of 32 AWG, 15/44 Litz wire wound to an average diameter of 2 cm and height of 1 cm. The first generation coil form was designed in Solidworks (Dassault Systemes Solidworks Corp., Waltham, MA, USA) and 3D printed using ABS plastic. This approach is useful for lower temperature applications, but could not withstand the temperatures used in the current experiments without severely warping the coil form. The final, high temperature coil form is machined out of 1.25 inch diameter Ultem plastic rod (McMaster-Carr, item 8686K77). Final measured coil inductance when connected via a BNC cable is 4.674 mH with Q = 13.9 at 10 kHz. Coil resistance, including the BNC cable connection, is 21.01 Ω resulting in $V_{RMS,\ noise} \approx 0.1\ mV$ at room temperature.

2.2.3 Duplexer and Tuning Circuit

In order to isolate the transmission phase from the receive phase, we use a simple duplexing circuit similar to the ones in Refs. [38] and [41]. As shown in Figure 2.4, a pair of crossed 1N914 diodes (D1 and D2) conduct during the transmit phase. This puts capacitor C in parallel with C_tune and the NMR coil. Since C is relatively small for the current working frequency of the spectrometer, it does not significantly detune the resonance circuit during transmission. Also, capacitor C prevents grounding of the circuit through the preamp, which

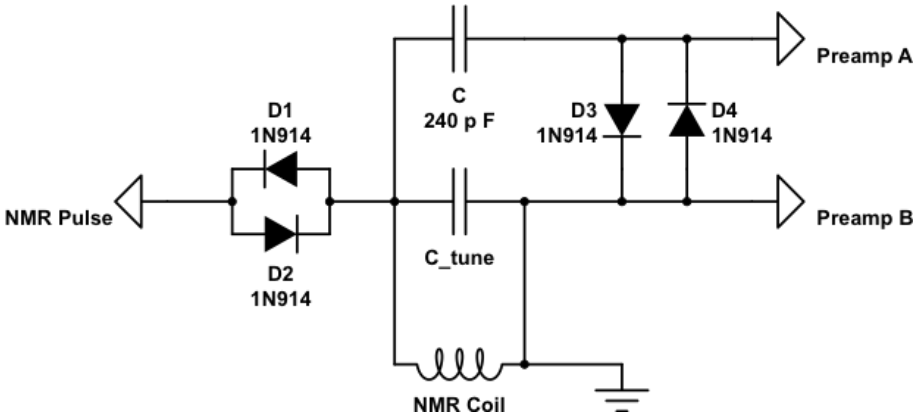

Figure 2.4: Schematic of the NMR coil tuning circuit and duplexer. The crossed diodes D1 and D2 conduct during the transmission phase, but appear open to the preamp during the receive phase. They further serve to isolate the transmitter from the receive stage, reducing noise in the NMR measurements. Crossed diodes D3 and D4 act as a diode clamp that prevents overloading of the preamp during transmission. Excitation pulse amplitudes range from 1-10 V, while the received NMR signal is on the order of 10^{-1} mV.

is blanked to ground during transmit. C_tune serves as the tuning capacitor for the NMR probe tank circuit and has a value of 0.01 μF for a working frequency of 23.1 kHz. Crossed diodes D3 and D4 prevent preamp overloading during transmit, which can be problematic even when the preamp is blanked. During the receiving stage, the crossed diodes D1 and D2 are open and capacitor C simply serves as a coupling capacitor to the preamp. For higher working frequencies, an inductor to ground, added before the crossed diodes, to counteract the capacitor C if it poses problems for tuning, as well as a variable capacitor in parallel with C_tune, could be added[38]. The circuit is housed in an aluminum box to reduce the effect of external noise. Signals pass in and out of the box via isolated BNC bulkheads (Amphenol RF 112443). The Q value of any components in the circuit must be considered carefully as they can substantially degrade the induced NMR signal. Both capacitors are ultra-high Q (>10,000 at 1 kHz) model 1111C (Passive Plus, Inc., Huntington, NY, USA).

2.2.4 Preamplifier and Spectrometer Shielding

To amplify the received NMR signal, we use an SR560 low-noise preamplifier (Stanford Research Systems, Sunnyvale, CA, USA). The preamp settings used for most experiments

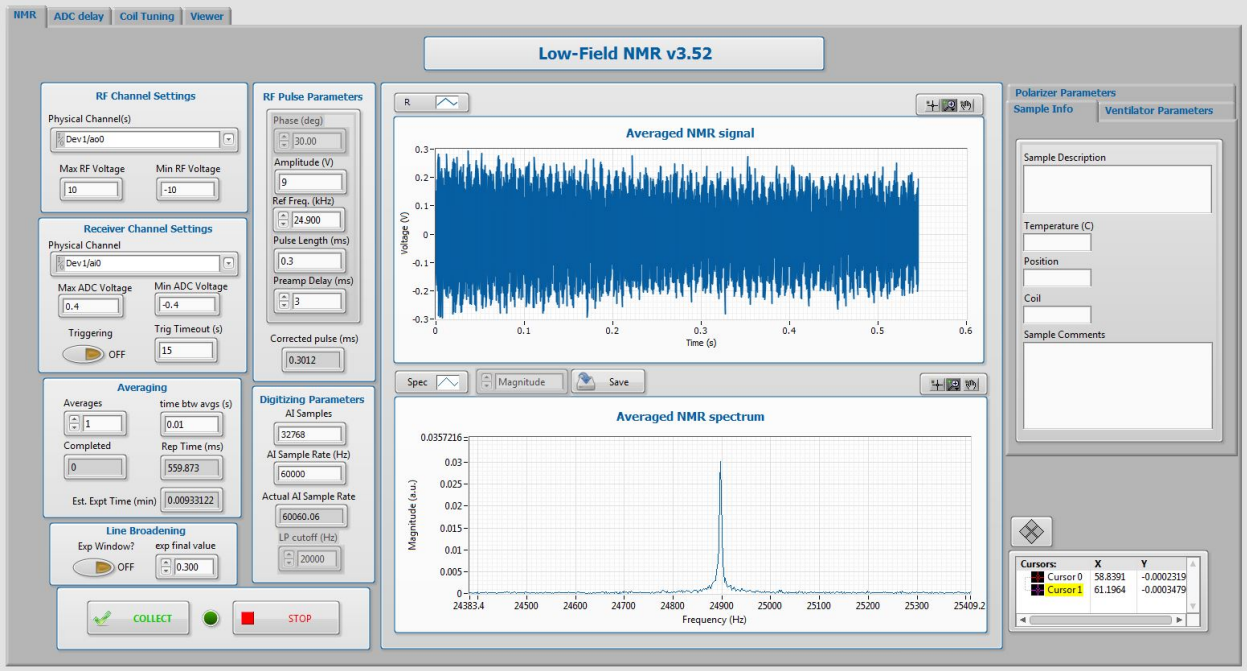

Figure 2.5: Screenshot of the ultra-low field NMR spectrometer LabVIEW control interface.

are low-noise mode with a differential measurement between inputs A and B (see Figure 2.4), a gain of 1000, and an analog bandpass filter (6 dB/octave rolloff) with range 10 - 30 kHz. During transmission, the preamp is blanked by a TTL pulse from a digital output on the PCI-6110. The preamp and enclosed duplexer are both housed within a heavy aluminum case to provide extra shielding from background RF interference and noise. Signals pass through the case via isolated BNC bulkheads.

2.2.5 LabVIEW Controller

The spectrometer is programmed and controlled using LabVIEW systems engineering software. Figure 2.5 shows a screenshot of the LabVIEW interface which allows the user to adjust all of the low-level digital and analog channel settings, pulse timing, acquisition and digitization parameters, and averaging. The current implementation uses a linear programming architecture for simplicity as shown in Figure 2.6. Data can be optionally pre-processed with line-broadening for improved SNR. All NMR parameters, as well as manually input information related to the sample, can be output as a text file along with

the raw time-domain NMR data for post-processing and analysis. Additionally, a utility for finding the resonance frequency of new NMR coils is included with the spectrometer code. A screenshot of the tuning utility is shown in Figure 2.7.

2.3 Optical Spectrometer

One important tool needed to monitor SEOP conditions inside optical cells on a regular basis is an optical spectrometer. As an alternative to typical commercial spectrometers, we describe here the design of an optical spectrometer suitable for both high and low resolution optical spectroscopy in a research laboratory. The following design allows for easy exchange of commercially-available, blazed reflective diffraction gratings that span a wide range of wavelengths and resolutions in the ultra-violet, visible and near-infrared range.

The current design is particularly suitable for SEOP with Rb and ^{129}Xe, where a wide range of wavelengths and resolutions is desirable for monitoring the pumping conditions within the optical cell. For example, with the more common use of tunable diode lasers, research groups have a greater need to monitor the laser center frequency and line width using a high-resolution measurement around 794.7 nm. At the same time, certain conditions can lead to energy pooling processes that emit violet light of wavelength 421 nm, as well as other wavelengths between 500 and 640 nm, depending on the strength of the energy pooling and temperature of the optical cell[20]. Both high and low resolution measurements are useful for characterizing these processes. Finally, high resolution atomic absorption measurements are useful for observing the absorption line width and shift of the Rb D1 and D2 lines, as well as providing a measurement of relative Rb vapor density within the optical cell.

For a Czerny-Turner optical spectrometer like the one presented here, the spectral resolution is given by

$$\delta\lambda = \frac{F \cdot \Delta\lambda \cdot W_s}{n \cdot W_p} \tag{2.2}$$

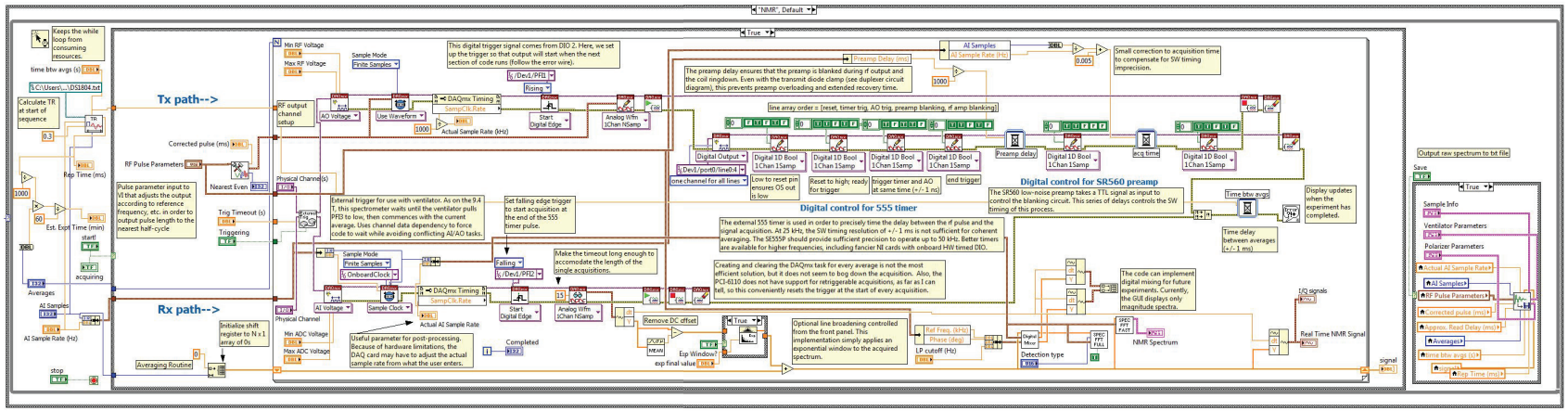

Figure 2.6: Screenshot of the ultra-low field NMR spectrometer LabVIEW block diagram.

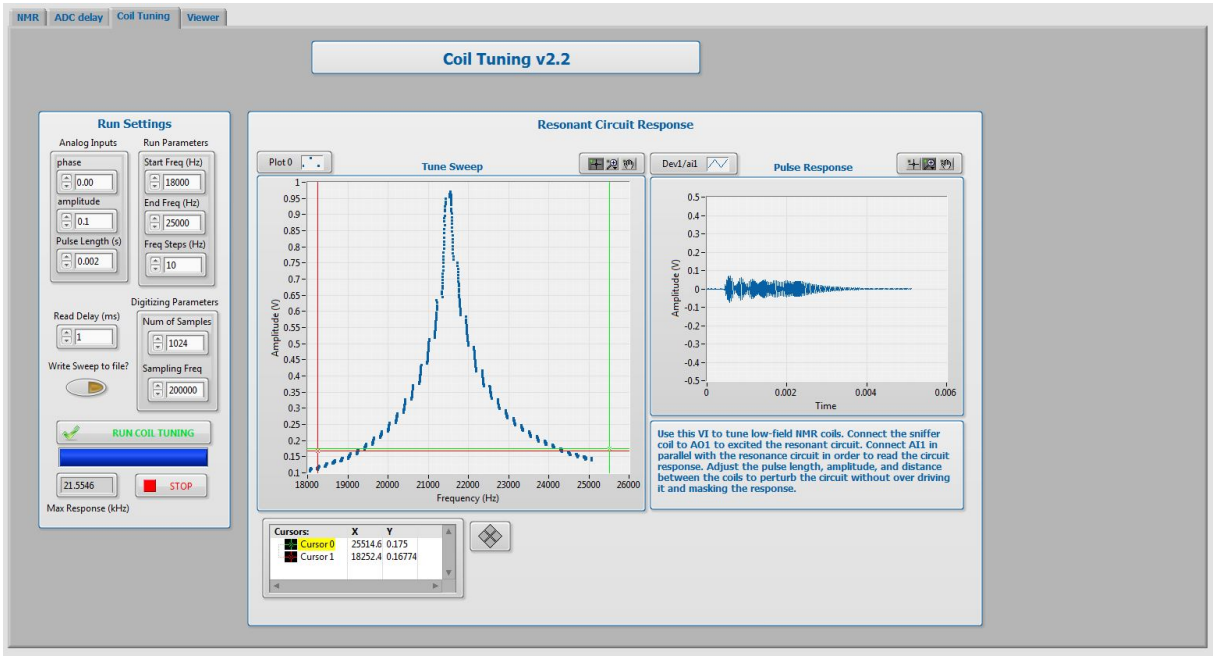

Figure 2.7: Screenshot of the ultra-low field NMR spectrometer LabVIEW coil tuning utility.

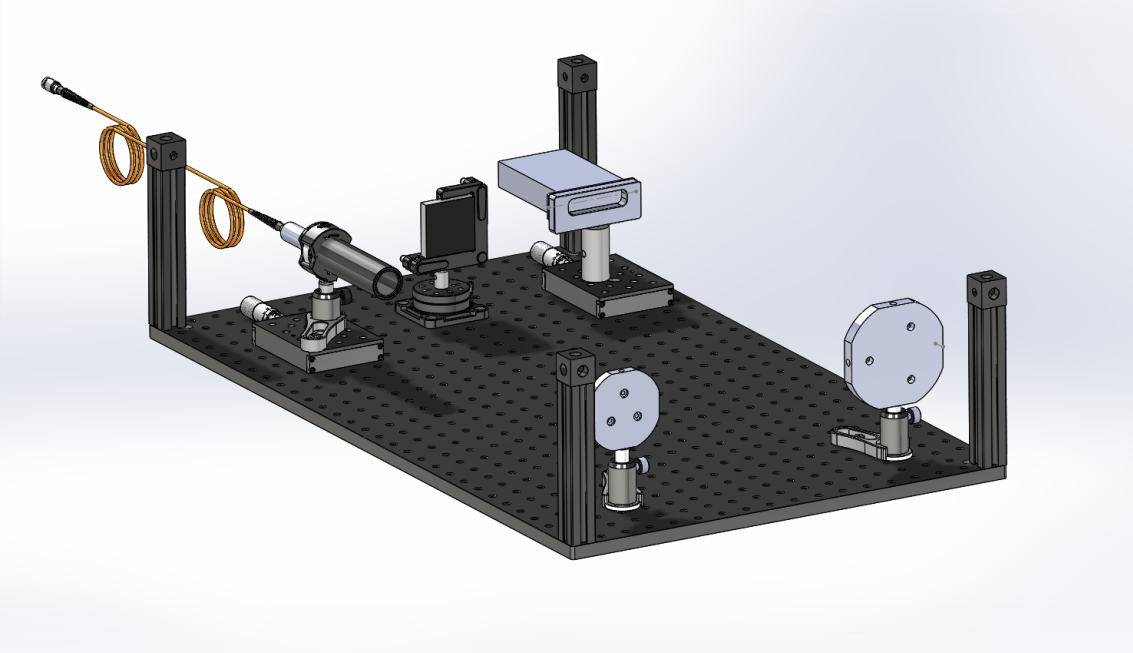

Figure 2.8: Solidworks model of the optical spectrometer built for optical absorption and pump laser profile studies. The 5 μm slit should be placed at the focal point of the 5.08 cm mirror, while the line CCD camera should be at the focal point of the 7.62 cm mirror.

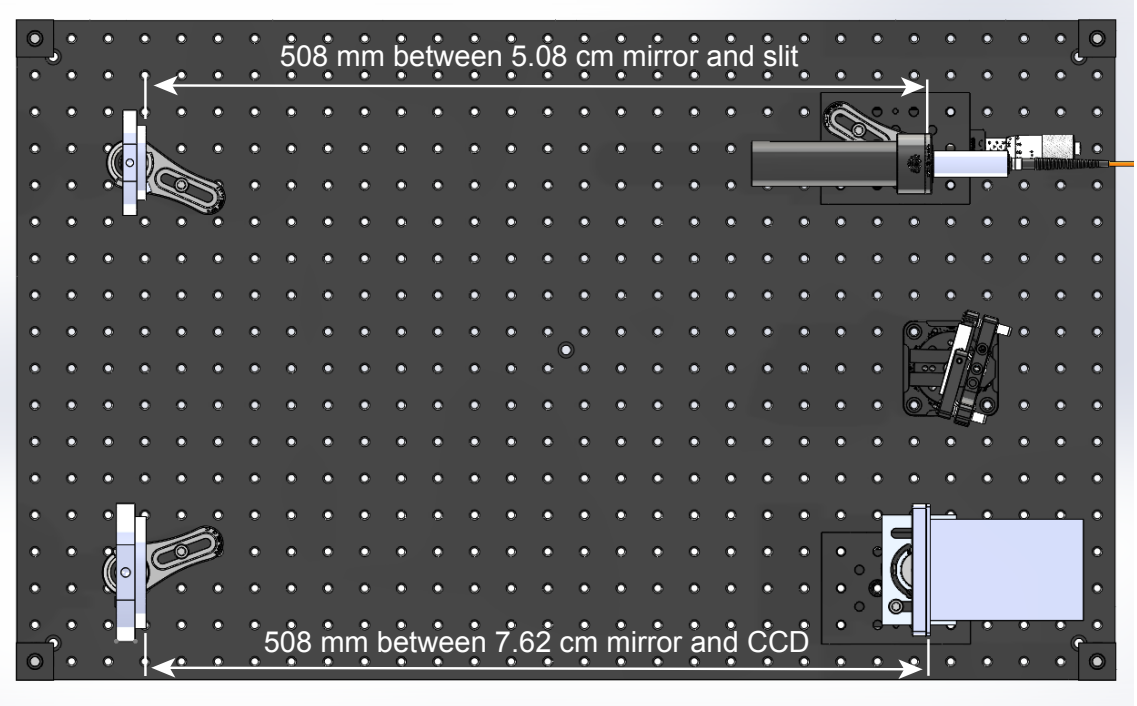

Figure 2.9: Top view of optical spectrometer assembly with enclosure removed. The mounted slit and line CCD camera are both located at the 508 mm focal length of the parabolic mirrors. Translation stages are used to the fine-tune the spectrometer after alignment. Knobs on the diffraction grating kinematic mount allow for fine adjustment of the grating position.

where F is a resolution factor determined by how comparable in size are W_s, the slit width, and W_p, the charge-coupled device (CCD) pixel width, $\Delta\lambda$ is the spectral range of the spectrometer, and n is the number of pixels in the CCD (3648 in our case). For our spectrometer, the slit width is 5 μm and the pixel width is 8 μm, giving a resolution factor of about 3. For the 300 lines/mm grating, our spectral range is 175.1 nm yielding a spectral resolution of about 0.09 nm. For the 1200 lines/mm grating, the spectral resolution is about 0.017 nm.

The spectrometer assembly, shown in Figure 2.8, is built entirely of commercially-available parts, with the exception of one custom-machined bracket used to mount the CCD line camera. Figure 2.9 shows a top view of the spectrometer assembly.

To assemble the spectrometer:

1. Roughly place the mirrors, the mounted slit, and the CCD camera as shown in Figure 2.9. To align the optics, we found a HeNe laser to be most convenient since it is clearly visible to the eye. The 5.08-cm parabolic mirror should collimate the light from the mounted slit onto the diffraction grating.

2. Position the diffraction grating such that the blaze arrow points towards the mounted slit and the first-order diffraction pattern falls on the 7.65-cm parabolic mirror.

3. Adjust the rotating mount in order to change the horizontal position of the diffracted light and then lock the mount in place with the set screw.

4. Use the kinematic mount adjustment knob to adjust the vertical position of the diffracted light onto the mirror.

5. Finally, the 7.62-cm mirror should image the diffraction pattern evenly onto the line CCD camera for display and collection.

6. To fine-tune the slit and CCD position, simply replace the HeNe laser with the low-pressure argon lamp and adjust the translation stages and kinematic mount knobs until the argon emission lines are symmetric and as narrow as possible.

CHAPTER 3: DEPOLARIZATION OF ^{129}XE DURING SEOP BY DARK RB & RB NANOCLUSTERS

This section presents results published in the *Journal of Magnetic Resonance*.[1]

3.1 Introduction

In this work we perform combined NMR measurements and atomic absorption spectroscopy (AAS) measurements to understand some of the possible causes of xenon depolarization during continuous-flow SEOP. Specifically, we first use AAS measurements to assess the presence of the postulated nanoscale Rb clusters inside the optical cell[34]. Since during the formation process of Rb clusters Rb_2 are expected to be formed first, AAS could in principle be used to observe the presence of the hypothesized clusters. Then, we evaluate the presence and the impact of optically dark Rb vapor in the outlet of the optical cell on final ^{129}Xe polarization. While seemingly obvious when one compares the better performance of polarizer designs that incorporate cooling regions in the front of the optical cell to condense Rb vapor [25, 26, 47, 48] with those that do not [19, 34, 49, 50], the effects of dark Rb regions on xenon polarization have never been investigated.

3.2 ^{129}Xe Polarization Model

The final expected ^{129}Xe polarization after cryogenic collection is given by[34]

$$P_{Xe}\left(t_{res}, t_a, T\right) = \frac{\gamma_{SE}(T)}{\gamma_{SE}(T)+\Gamma}\langle P_{Rb}(T)\rangle\left(1-e^{-(\gamma_{SE}(T)+\Gamma)t_{res}}\right)\left(\frac{T_1}{t_a}\right)\left(1-e^{-\frac{t_a}{T_1}}\right), \qquad (3.1)$$

[1] Antonacci MA, Burant A, Wagner W, and Branca RT. Depolarization of nuclear spin polarized ^{129}Xe gas by dark rubidium during spin-exchange optical pumping. *Journal of Magnetic Resonance* 2018; 279:60-67. DOI: 10.1016/j.jmr.2017.04.011.

where γ_{SE} is the Rb-Xe spin-exchange rate, Γ is the ^{129}Xe nuclear spin destruction rate, $\langle P_{Rb}(T)\rangle$ is the mean Rb spin polarization throughout the optical cell, t_{res} is the mean xenon residency time in the optical cell, t_a is the total accumulation time, T is the absolute temperature, and T_1 is the longitudinal relaxation time of solid ^{129}Xe. The factor $\left(\frac{T_1}{t_a}\right)\left(1-e^{-\frac{t_a}{T_1}}\right)$ accounts for relaxation of solid xenon during progressive cryogenic collection, as described in Ref. [33]. Equation (3.1) clearly shows that what ultimately sets the upper bound for the xenon polarization level is the Rb electron spin polarization. This can be expressed as a function of position along the cylindrical axis of the cell as[34]

$$P_{Rb}(z,T) = \frac{\gamma_{OP}(z,T)}{\gamma_{OP}(z,T)+\Gamma_{SD}(T)}, \tag{3.2}$$

where $\Gamma_{SD}(T)$ is the temperature-dependent Rb spin-destruction rate and $\gamma_{OP}(z,T)$ is the temperature- and position-dependent Rb optical pumping rate. The Rb spin-destruction rate is determined by binary collisions between Rb atoms and gases within the cell (Xe, N_2, and He), as well as from the formation and breakup of Rb-Xe van der Waals molecules. If we model the pump laser light as a Gaussian function, with center wavelength λ_l and width $\Delta\lambda_l$, and the broadened Rb D1 absorption cross section as a Lorentzian function, the optical pumping rate can then be written in terms of photon flux $F = \frac{I\cdot n_p}{A}$ as[50]:

$$\gamma_{OP}(z,T) = \frac{\beta}{[Rb]}F, \tag{3.3}$$

where I and A are pump laser intensity and cross-sectional area, respectively, n_p is number of photons per Joule of the pump laser, and $[Rb]$ is the Rb number density. The constant β is given by[50]:

$$\beta = \frac{2\sqrt{\pi \ln 2} r_e f_{D1} \lambda_l^3 w'(r,s)}{hc\Delta\lambda_l n_p}\,[Rb]\,, \tag{3.4}$$

where r_e is the classical electron radius, f_{D1} is the Rb D1 oscillator strength, h is Planck's constant, c is the speed of light, and $w'(r,s)$ is the real part of the complex overlap function, which depends on r, the ratio of the atomic D1 linewidth to the pump laser linewidth, and s,

the relative detuning between the pump laser and D1 atomic absorption cross section[51]. We can then describe the optical pumping rate along the length of the optical cell as[50]:

$$\frac{d\gamma_{OP}(z,T)}{dz} = -\beta\left(1 - s_z\frac{\gamma_{OP}(z,T)}{\Gamma_{SD}+\gamma_{OP}(z,T)}\right)\gamma_{OP}(z,T), \tag{3.5}$$

where s_z is the fraction of circularly polarized laser photons. Equation (3.5) can then be solved by separation of variables and used to calculate the optical pumping rate at discrete positions along the axis of the optical pumping cell[50]. The optical pumping rate at each discrete step is used to find the expected Rb polarization at that position via Equation (3.2). By substituting the mean of the Rb polarization values for a given temperature into Equation (3.1), we then calculate the expected final xenon polarization. The above equations were all coded and run with Wolfram Mathematica (Wolfram Research, Inc., Champaign, IL, USA) in order to model our particular experimental setup during gas production for human experiments. Specifically, the cell surface temperature was varied from 363 K to 423 K at a pressure of 1.6 atm, flow rate of 1.0 standard liters per minute (SLM), collection time of 20 min, incident laser power of 31.4 W, optical cell inner radius of 2.4 cm and cell length of 15 cm.

3.3 Atomic Absorption Spectroscopy (AAS) Measurements

3.3.1 Low-resolution Broadband Rb Absorption Spectroscopy on a Sealed Optical Cell

In an attempt to observe Rb clusters during SEOP, AAS measurements were the first to be made. Before performing AAS directly on the optical cell, measurements were made on a sealed Rb cell where temperature could be tightly controlled and Rb and Rb_2 number densities could be easily calculated[52]. The sealed Pyrex cell, 7.5 cm long and with a 2.5 cm outer diameter, was evacuated to about 10^{-6} torr and charged with ∼20 mg of molten Rb (Opthos Instruments, Inc., part D7). Initial observations were performed in low resolution mode to observe the $1(X)^1\Sigma_g^+ \rightarrow 1(B)^1\Pi_u$ Rb_2 absorption band caused by its large absorption

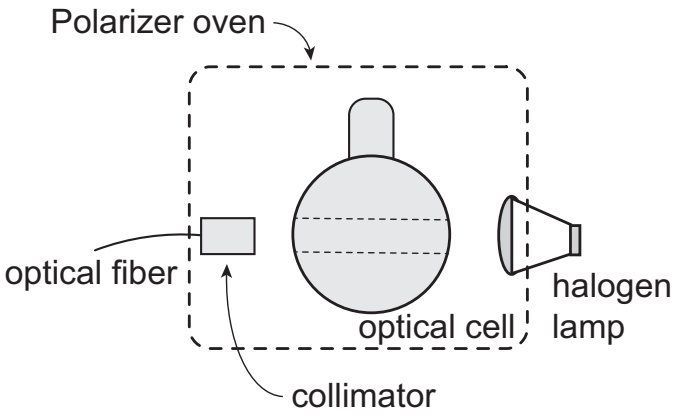

Figure 3.1: Diagram of low-resolution atomic absorption spectroscopy setup on the optical cell body.

cross-section[53, 54] and the availability of a diffraction grating with high efficiency in this wavelength range. A resistance temperature detector (RTD) was taped to the center of the cell with Kapton tape and the entire cell wrapped in heating tape and placed within an insulated aluminum box mounted on an optical quality aluminum breadboard (model MB4545/M, Thorlabs, Newton, NJ, USA). The temperature of the cell was regulated by a microcontroller (iTRON 702040, Jumo Process Control, Inc., East Syracuse, NY, USA). Absorption measurements were made by shining a broadband halogen light source (Thorlabs QTH10/M) through the absorption cell and collecting the transmitted light with a fiber collimator (Thorlabs F220SMA-780) for cell temperatures from 673 to 853 K.

3.3.2 Low-resolution Broadband Rb Absorption Spectroscopy During Continuous-flow SEOP

Similar measurements were made on the optical cell during continuous-flow SEOP. For these measurements, the original oven enclosure on the commercial polarizer was duplicated and modified to allow spectroscopy measurements to be performed in a direction perpendicular to the direction of the optical pumping laser. The halogen light source was mounted to shine within the polarizer oven and allowed to equilibrate for at least 12 hours prior to polarizer

warm-up. The fiber collimator was mounted opposite the light source and both were aligned for maximum transmission into the custom spectrometer as shown in Figure 3.1.

We collected AAS spectra during SEOP with flow rates of 0.1 SLM (typical rate for standby operation) and 1.5 SLM (typical rate for collection of clinical-scale volumes). We also collected AAS spectra immediately after flow began since dense Rb vapor was always observed at the beginning of the gas flow with a digital camera. Standard parameters for hyperpolarized ^{129}Xe production for these experiments were an optical cell pressure of 4.1 atm, cell temperature of 358 K, and presaturation bulb temperature of 438 K. Integration time for each spectrum was 10 ms with 4599 averages. Baseline spectra were also collected during polarizer cool-down once the Rb D1 and D2 absorption lines receded below noise level. This ensured maximum transmission of the broadband light through the optical cell. Baseline spectra were then used in post-processing as described below.

3.3.3 High-resolution Broadband Rb Absorption Spectroscopy During Continuous-flow SEOP

In order to study the presence of dark Rb in the optical cell outlet and its effect on xenon polarization, the AAS setup described above was mounted within the polarizer oven such that the optical cell outlet sat between the halogen lamp and the collimation lens as shown in Figure 3.2. The same stabilization procedure was used to allow the lamp to reach thermal equilibrium. Outlet absorption spectra were collected during SEOP at a flow rate of 1.0 SLM, optical cell pressure of 1.8 atm, and presaturation bulb temperature of 438 K, for a variety of oven temperatures between 363 and 423 K. Collection time was 20 min for each batch of hyperpolarized ^{129}Xe and absorption spectra were obtained 8-10 min into the collection time, with 10 ms integration time and 4599 averages.

The NMR surface coil was placed in the center of the optical pumping cell in order to monitor the in-cell ^{129}Xe polarization throughout the SEOP process. NMR spectra were collected using a block pulse of frequency 23.1 kHz, pulse length 0.325 ms, repetition time 524 ms, 50 averages, sampling frequency 200 kHz, and 4096 points. NMR measurements were

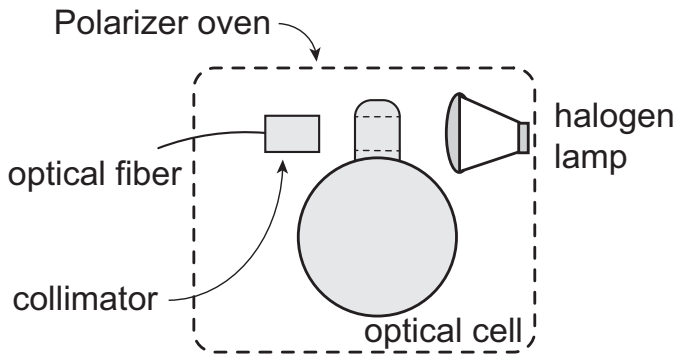

Figure 3.2: Diagram of high-resolution atomic absorption spectroscopy setup on the optical cell outlet.

made immediately following the outlet absorption measurement. The pump laser transmission was monitored by an on-board photodiode located behind the optical cell. This value was recorded concurrently with the NMR measurement. At the end of the collection time, the frozen xenon was sublimated into a 150 ml Tedlar bag (Jensen Inert Products, Coral Springs, FL, USA) and the polarization was measured with a calibrated polarization measurement station (Model 2881, Polarean, Inc., Durham, NC, USA).

3.3.4 Gas Temperature Calibration

One particular challenge of continuous-flow SEOP modeling is not knowing the exact temperature of the gas mixture within the pumping cell. To determine experimentally the temperature of the gas mixture flowing through an optical cell during SEOP is a notoriously difficult task. Turbulent fluid flow patterns [20], temperature gradients, and laser heating make the RTD temperature measurement from the cell surface suspect, at best. Newton, *et al*. [55] succeeded in using Raman spectroscopy to measure temperature at specific points in an optical cell during batch-mode SEOP, but no such measurements for continuous-flow SEOP have been reported in the literature. In an effort to obtain more accurate temperature measurements for the gas mixture in our optical cell, we developed a method to estimate the actual gas temperatures from the external RTD measurements.

First, we used the RTD temperature measurements on our cell, without flow or laser illumination, to calibrate transverse AAS measurements through the center of the optical cell. We expect the buffer-gas broadened D2 absorption line of Rb to be well-approximated by a Lorentzian lineshape because of the decaying exponential probability that an atom will be found in the ground state and hence be able to absorb an on-resonance photon[56]. Following Zheng, *et al.* [57], we first calculate $f(\nu) = \ln\left(\frac{I}{I_0}\right)$, the natural log of the ratio of our absorption spectrum I to our baseline spectrum I_0. Then we fit this result according to[57]:

$$f(\nu) = \frac{a + b(\nu - \nu_0)}{(\nu - \nu_0)^2 + (\Delta\nu/2)^2} + d, \tag{3.6}$$

where a is the peak amplitude, b is a dispersive correction resulting from buffer gas interactions, ν_0 is the center frequency of the D2 line, $\Delta\nu$ is the D2 linewidth, and d is a constant offset. From the peak amplitude, linewidth, and absorption path length l we calculate the average Rb density over the optical path[57]:

$$[Rb] = \frac{2a}{r_e c f_{D2} \cdot l \cdot \Delta\nu}, \tag{3.7}$$

where f_{D2} is the Rb D2 oscillator strength. With a Rb vapor pressure curve[58], this number density can then be used to extract an average temperature for the vapor along the absorption path inside the optical cell. We found that this method systematically results in measured temperatures 7 - 26 K lower than what was measured by the RTD, even though there was no gas flow through the cell. Thereafter, we fitted a correction function that appropriately scaled the AAS temperature measurement to match the RTD measurement, and hence calibrated our AAS measurements within the temperature range of interest (Figure 3.3). This allowed us to make AAS temperature measurements during SEOP with the same setup, obtain reliable temperature measurements of the gas at the center of the cell, and correlate them with the RTD temperature measurements.

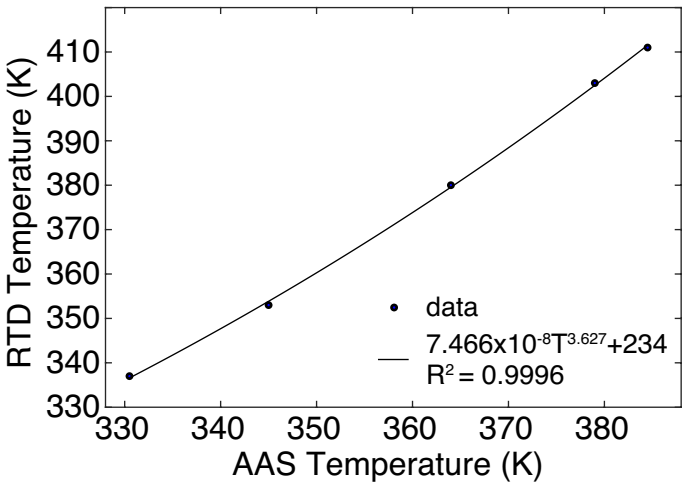

Figure 3.3: Plot of the correction function used to calibrate AAS temperature measurements within the optical cell. Data were acquired with no gas flow or pump laser illumination. The uncertainty in temperature measurements is indicated by the size of the data point.

3.3.5 Analysis of Spectra

All absorption spectra were processed by first dividing by the scaled baseline spectrum from the halogen lamp. The D2 peaks were then fitted with a normalized Lorentzian line shape function with area uncertainty given by the 95% confidence interval of the line area parameter. NMR spectra were likewise fit with a normalized Lorentzian line shape and the line area used as a measure of the signal intensity.

3.4 Results

The theoretical final ^{129}Xe polarization vs. cell temperature as predicted by the standard model above is plotted in Figure 3.4, along with experimental measurements made on our commercial polarizer. The maximum expected xenon polarization should be on the order of 44% for these parameters, whereas the maximum final xenon polarization obtained experimentally was only 25%. While slight mismatches between the calculated and observed temperature for maximum ^{129}Xe polarization can be easily explained by uneven laser light heating of the gas inside the optical cell, as previously reported in the literature[55, 59–61],

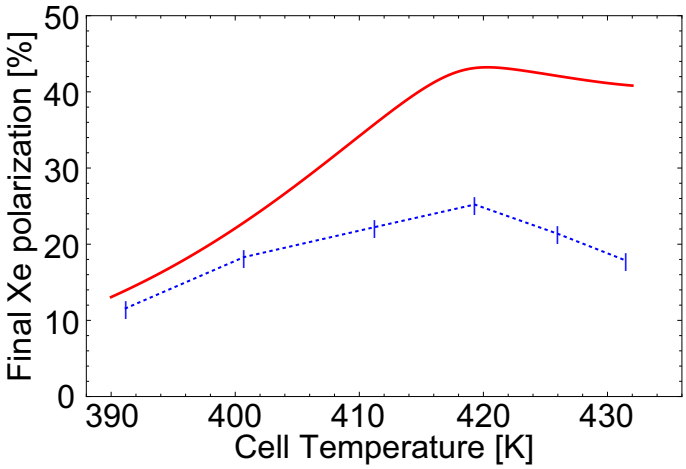

Figure 3.4: Experimental and theoretical final ^{129}Xe polarization as a function of cell temperature. (blue) Experimental best final ^{129}Xe polarization vs. cell temperature at a gas flow rate of 1.0 SLM and collection time of 20 min. Dashed connecting lines are drawn only to guide the eye. (red) Theoretical ^{129}Xe polarization vs cell temperature for the same operating parameters, calculated using Equation (3.1).

the decrease in polarization observed at higher temperatures is clearly faster than what is predicted by the standard model[34].

3.4.1 Rb Dimers

Absorption spectra acquired from the sealed Rb cell are shown in Figure 3.5. The $1(X)^1\Sigma_g^+ \rightarrow 1(B)^1\Pi_u$ molecular transitions between 640 and 740 nm begin to appear clearly around 773 K, becoming stronger at higher temperatures, as expected. The Rb D2 absorption line is also clearly visible in the observed bandwidth. Based on known vapor curves[52], at 773 K the density of atomic Rb is 8.6×10^{19} cm^{-3} and of Rb_2 is 2.3×10^{16} cm^{-3}.

Absorption spectra collected during SEOP, both during continuous-flow SEOP and at the start of flow, are shown in Figure 3.6. The Rb D2 absorption line is clearly visible. Within the observed bandwidth, we would expect to see a broad absorption band from the X-B molecular transitions if a sufficient density of dimers were present in the optical cell[54]. In neither the case of continuous-flow SEOP at 0.1 and 1.5 SLM, nor at the time of the cell opening, did we observe this absorption band.

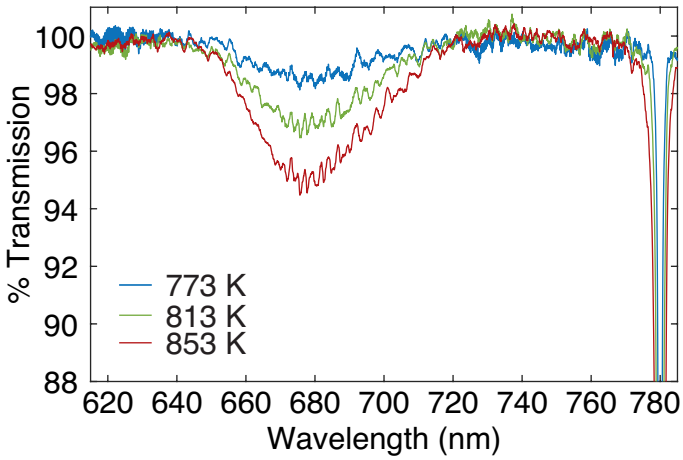

Figure 3.5: Rb_2 absorption bands in closed Rb cell. The sharp absorption line at 780 nm is the atomic Rb D2 line. The weakest Rb2 band was observed at a cell temperature of 773 K, and the strongest at 853 K.

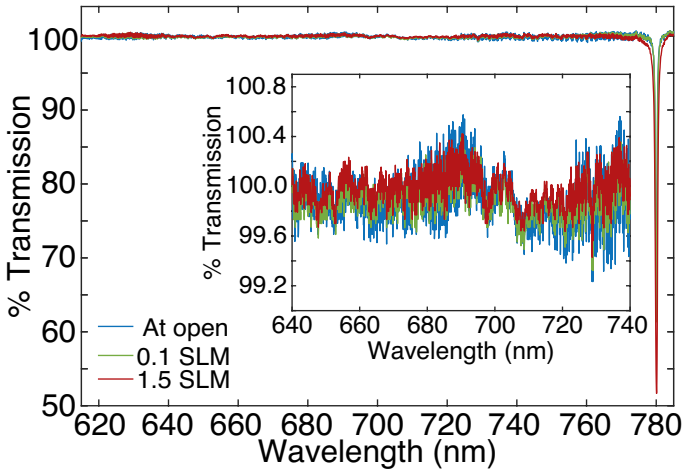

Figure 3.6: Rb absorption spectra obtained during SEOP at 0.1 and 1.5 SLM, as well as at the start of flow through the optical cell. Notice the clear D2 atomic absorption line at 780 nm. The inset shows a zoomed-in view of wavelengths where the Rb_2 X-B absorption band would be expected. No absorption band is discernible above background.

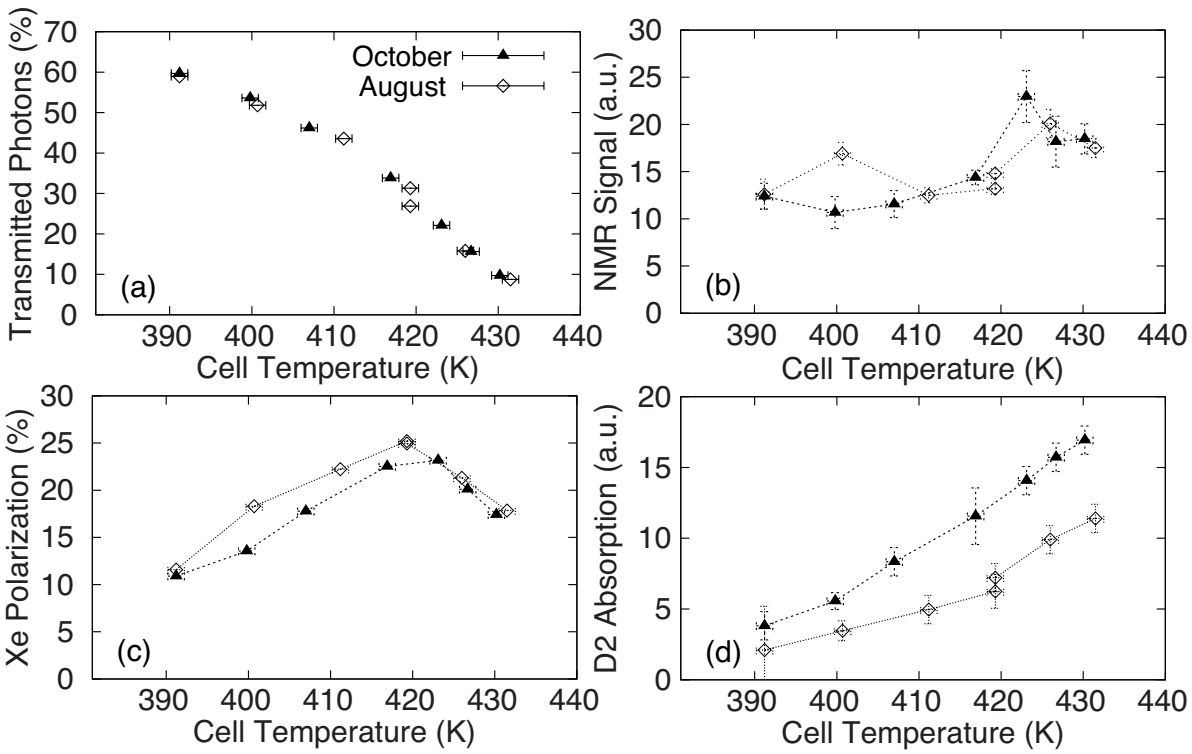

Figure 3.7: Results from the cell outlet depolarization measurements taken at a flow rate of 1.0 SLM. The temperature of the presaturation bulb was kept constant at 438 K, while cell pressure was 1.8 atm. The measurements were made twice on the same cell, over a month apart, for validation. (a) Transmitted photons as measured by a photodiode located on the back of the cell vs. optical cell temperature; (b) NMR signal from the optical cell vs. cell temperature; (c) Final xenon polarization vs. cell temperature; (d) Rb D2 absorption intensity at the cell outlet vs. cell temperature. Connecting lines are drawn to guide the eye.

Based on the Rb absorption spectra collected from the closed Rb cell, we estimated a sensitivity of 8.3×10^{15} cm^{-3} for Rb_2 using our optical spectrometer and a similar upper-limit value for Rb_2 present during our continuous-flow SEOP experiments. This limit was calculated by scaling the minimum Rb_2 density visible in the closed cell by the ratio of the D2 absorption line amplitudes in the closed cell and during continuous-flow SEOP.

3.4.2 Depolarization in the Optical Cell Outlet by Dark Rb

Both NMR spectroscopy and AAS measurements performed on the optical cell during SEOP as a function of cell temperature, as well as the pump laser transmission along the optical cell, are reported in Figure 3.7. Despite the two measurements being performed more

than a month apart, during which the polarizer was used to produce hyperpolarized ^{129}Xe for human use, results were very consistent. As expected, the increased Rb density at high temperature leads to an increase in absorption and to a reduction of the transmitted light. Over the range of temperatures measured, the NMR signal from polarized ^{129}Xe remained basically constant (see Figure 3.7b). However, as can be seen in Figure 3.7c, the final xenon polarization reached a maximum at 419 K and at 423 K for the earlier and later trials, respectively. Clearly, some depolarization mechanism overtook the positive spin-exchange at higher temperatures, damaging the final polarization. Figure 3.7d shows the absorption intensity of the Rb D2 transition across the optical cell outlet vs. cell temperature, indicating an increase in the Rb vapor density in the cell outlet at higher temperatures.

3.5 Discussion and Conclusions

As far as we know, this is the first experimental attempt to observe Rb_2 during SEOP using broadband absorption. Some attempts have been made to observe Rb clusters through Mie scattering of broadband light, but none have succeeded[62].

Although we were not able to directly observe Rb_2 during continuous-flow SEOP, we were able to set an upper limit for the observable density of Rb_2 present in the optical pumping cell during SEOP to less than 8.3×10^{15} cm^{-3}, which is what could be directly detected by our spectrometer. Since for our polarization setup Freeman, *et al.*'s model predicts a cluster density on the order of 1×10^{9} cm^{-3}, an improvement in sensitivity of 6 orders of magnitude would be necessary in order to directly detect Rb dimers during SEOP with our current spectrometer. Although the sensitivity could be improved by extending the absorption path via multiple reflections through the optical cell and/or by increasing the integration time and number of averages, it is highly unlikely that we could achieve an improvement in sensitivity of 6 orders of magnitude. Taken together, our results indicate that absorption spectroscopy, unlike what was originally proposed by Freeman, *et al.*, is not sensitive enough to detect

the presence of Rb dimers during continuous-flow SEOP, and other techniques should be investigated in order to experimentally validate the cluster model.

Interestingly, when gas flow was first turned on, we did observe through a digital video camera (model HMC-40, Panasonic, Chesapeake, VA, USA) a dense Rb vapor that was quickly dispersed throughout the optical cell. However, when AAS measurements were performed to detect the possible presence of Rb dimers in this dense vapor, no significant differences were seen with respect to spectra acquired during steady-state flow (see Figure 3.6). Therefore, at this point, it is unclear whether this vapor is simply atomic Rb that has condensed at the optical cell inlet and is disturbed at the start of flow, or whether it is the result of some more complex process.

Combined NMR measurements of in-cell polarization and final polarization suggest that, at high temperature, part of the xenon polarization is lost outside the optical cell. Since AAS measurements show an increase in Rb density in the outlet of the cell when temperature is increased, it is reasonable to think that hyperpolarized ^{129}Xe interaction with dark Rb vapor present in the outlet of the cell is responsible for at least part of the observed xenon depolarization at higher temperatures. This temperature-dependent spin-exchange depolarization effect from dark Rb in the optical cell outlet can be included in the SEOP theory as a correction factor that takes the same form as the in-cell spin-exchange interaction[34]:

$$\Delta_{darkRb}\left(t_{outlet}, T\right) = e^{-\gamma_{SE}(T) t_{outlet}}, \tag{3.8}$$

where T is the absolute cell temperature and t_{outlet} is the residency time of polarized ^{129}Xe in the optical cell outlet. The final xenon polarization will then be given by

$$P_{Xe}\left(t_{res}, t_a, t_{outlet}, T\right) = P_{Xe}\left(t_{res}, t_a, T\right) \Delta_{darkRb}\left(t_{outlet}, T\right). \tag{3.9}$$

For our polarizing parameters, Figure 3.8 shows the predicted ^{129}Xe polarization vs. cell temperature curve as modeled in Equation (3.9). In the absence of turbulence in the cell

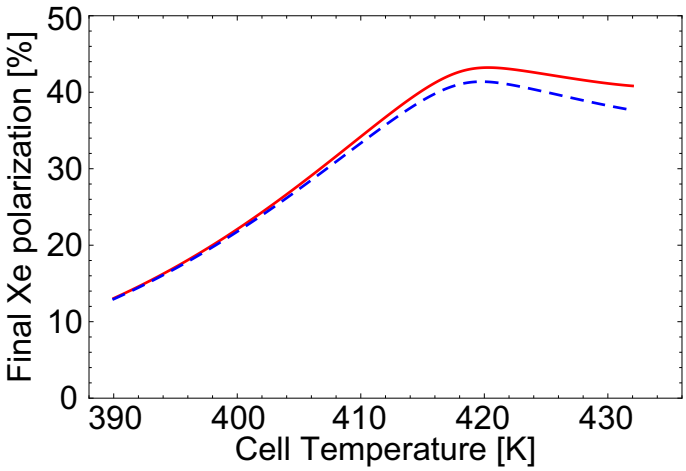

Figure 3.8: Final ^{129}Xe polarization vs. cell temperature with the same polarizing parameters as the experimental data shown in Figure 3.4, (red line) without outlet depolarization and (blue dashed line) calculated using Equation (3.9).

outlet, the estimated residency time of hyperpolarized ^{129}Xe in our cell outlet at a flow rate of 1.0 SLM is about 0.8 s. Under this condition, and at the maximum cell temperature studied here (432 K), a reduction of the final polarization of ∼8% is expected by dark Rb in the outlet of the cell. While the depolarizing effect of dark Rb is not more than a few percent at our typical running parameters, this could be a significant effect for polarizers running in a higher temperature regime and/or at lower flow rates[33, 34, 49, 59]. In the presence of turbulence in the cell outlet, such values could be considerably higher. Interestingly, despite when we assume absence of turbulence the reduction of the final xenon polarization is only ∼8%, the rate at which the final xenon polarization is expected to decrease with temperature because of dark Rb nicely followed the experimental values.

In conclusion, we have attempted to observe Rb_2 during SEOP using broadband AAS. Comparison with measurements performed on a sealed Rb absorption cell indicated that broadband AAS is not sensitive enough to observe the density of paramagnetic Rb clusters postulated by Freeman, *et al.*, even if that population were composed entirely of dimers. We also studied the depolarizing effect of dark Rb vapor in the optical cell outlet on the final ^{129}Xe polarization. While wall relaxation is typically assumed to be the primary source of relaxation for xenon polarization[19, 25, 47, 63, 64], our results show that dark Rb vapor in

the cell outlet can lead to reductions in final ^{129}Xe polarization of tens of percent at higher temperatures and lower flow rates, and should be considered carefully in polarizer design. Although Refs. [25] and [47] mention the need for cooling regions to prevent the presence of unpumped Rb vapor, no one, to our knowledge, has measured the effects of this vapor on the final xenon polarization. Furthermore, this study also shows that an optimized in-cell xenon polarization does not necessarily entail an optimized final ^{129}Xe polarization.

CHAPTER 4: ROBUST REFERENCING METHOD FOR DISSOLVED PHASE ^{129}XE NMR SPECTROSCOPY

Results in this section have been published in the journal *Magnetic Resonance in Medicine*.[1]

4.1 Background and Motivation

Arguably the most important parameter in NMR spectroscopy is the chemical shift, or change in precession frequency, induced by variation of the local magnetic field felt by the nucleus, arising from the electronic distribution of the atom. The interaction of precessing nuclear spins with the chemical (electronic) environment, specifically, can serve as a useful probe of a system's molecular structure, composition, and even macroscopic physical characteristics such as temperature and pressure. In this section, we outline the origin and practical utility of the chemical shift in NMR spectroscopy. Then, we proceed to discuss some problems with the conventional reference standard used for ^{129}Xe NMR spectroscopy and, finally, propose an alternative, more robust reference for dissolved-phase ^{129}Xe NMR spectroscopy.

4.1.1 ^{1}H Chemical Shift

The major players in the magnetic environment of nuclei are the surrounding valence and chemical bond electrons. The orbital structure of the surrounding electrons plays a major role in determining the chemical characteristics of a molecule. Furthermore, the magnetic

[1] Antonacci MA, Zhang L, Burant A, McCallister D, Branca RT. Simple and robust referencing system enables identification of dissolved-phase spectral frequencies. *Magnetic Resonance in Medicine* 2018; 80:431-441. DOI: 10.1002/mrm.27042.

field felt by the nucleus is given by the outside static field plus the field produced by these surrounding electrons[8]. Any change in the distribution of the electrons around a given nucleus manifests itself with a change in the NMR frequency. This effect is known as the chemical shift[65]. Since the electron cloud of a given atom is easily modified by the presence and distribution of nearby atoms, it is easy to see how the the chemical shift is a useful probe of an atom's chemical environment[66].

The experimental measurement of the absolute value of the chemical shift is often complicated by a number of outside factors, including the field strength and shimming conditions. To reduce these complications, a robust frequency reference is typically added to a sample. For ^{1}H spectroscopy, the standard reference is tetramethylsilane (TMS). By referencing the ^{1}H chemical shift to that of TMS, one can easily remove frequency shifts caused by field strength, shimming conditions, and magnetic susceptibility, while retaining chemical shift information. Also, the compound is inert and readily dissolves in most water-based solutions, making it an ideal reference standard for nearby ^{1}H [8]. The general field-independent expression for a chemical shift δ (deshielding) is given by

$$\delta = \frac{\omega - \omega_{ref}}{\omega_{ref}}, \tag{4.1}$$

where ω_{ref} is the Larmor frequency of the reference compound. Chemical shifts are typically reported in parts per million (ppm), a unit which makes the chemical shift field independent.

Since the ^{1}H chemical shift has been very well characterized, both theoretically and experimentally, it serves as a useful tool to probe the chemistry of a system, both *in vitro* and *in vivo*. *In vitro*, the chemical shift serves often as an important parameter in determining molecular structure by high resolution NMR[66–68]. In general, the chemical shift is represented as a tensor; however, in solution-state NMR experiments with isotropic liquids, the chemical shift effect is given simply by a scalar average value[66].

Of particular interest in this work is the use of chemical shift information to probe tissue structure and temperature. For example, the chemical shift of ^{1}H signals in a triglyceride

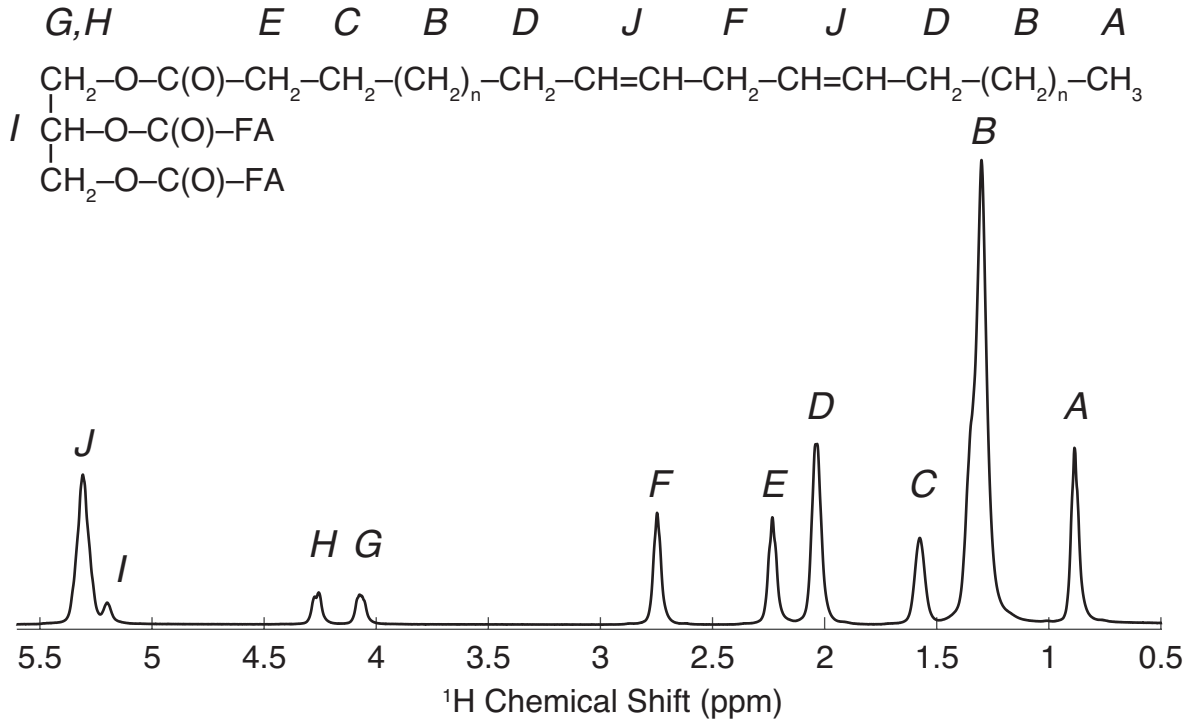

Figure 4.1: ^{1}H NMR spectrum of neat trilinolein taken on a 500 MHz spectrometer and referenced to TMS. Peak contributions from different locations on the triglyceride molecule are labeled A-J. Water would appear at approximately 4.9 ppm.

molecule indicates the ^{1}H position within the triglyceride molecule. Figure 4.1 shows an example ^{1}H NMR spectrum of neat triolein where chemically different protons are clearly resolved.

4.1.2 ^{129}Xe Chemical Shift

Xenon-129 at room temperature is an inert gas with a nuclear spin of 1/2, a very large chemical shift range (>200 ppm)[69, 70] in gas mixtures[71–74] and solutions[75–80], and relatively high solubility in organic solvents[81, 82], biocompatible carrier solutions[83–85] and tissues[69, 86–90]. Table 4.1 gives the Ostwald solubility coefficient for xenon in various solvents and tissues.

Table 4.1: Ostwald solubilities of xenon in various tissues and solvents at 37°C.

Solvent	Ostwald Solubility Coefficient [86]
adipose tissue	1.72
red blood cells	0.27
white matter	0.22
gray matter	0.14
skeletal muscle	0.11
renal cortex	0.14
renal medulla	0.14
olive oil	1.83
distilled water	0.08

Because of the sensitivity of the ^{129}Xe chemical shift to the molecular environment, ^{129}Xe NMR has served as a useful tool to probe sample structure in material science. For example, Ripmeester and Ratcliffe[91] used ^{129}Xe NMR chemical shifts to measure the pore sizes of a range of zeolites. Huang, *et al.* [92] used hyperpolarized ^{129}Xe NMR to study functionalized mesoporous silica. The exquisite sensitivity of the ^{129}Xe chemical shift to the chemical environment enabled them to extract information about the material surfaces, pore structures, and functional groups attached to the material surface. As a final example, Farina, *et al.* [93] studied micro- and mesoporous carbon (biochar) produced from almond shells in order

to determine pore size and chemical exchange within the sample. The use of ^{129}Xe NMR chemical shift measurements to characterize novel materials continues to expand[94–96].

Xenon has also been widely used for *in vivo* MRI experiments to monitor lung ventilation function. Because of its relatively high solubility in tissues, once inhaled[84, 97, 98], it readily dissolves in lung parenchyma[99, 100] and into the blood[101–106], by which it is transported to other regions of the body[88, 107–113]. In distal organs, xenon dissolves in a manner that depends on tissue perfusion and on the relative tissue/blood solubility. In highly perfused and lipid-rich tissues like brown fat, the concentration of xenon upon inhalation can reach values comparable to those reached in the lungs[114]. At the typical concentrations achieved *in vivo* during gas inhalation (mM or sub-mM), xenon clearly needs to be hyperpolarized to enable its detection in a reasonable time.

4.1.3 Motivation

Applications of dissolved-phase, hyperpolarized xenon (DPXe) imaging and spectroscopy have increased considerably over the past 5 years, and include monitoring of gas exchange[115, 116] and alveolar septa thickness in the lungs[99, 100, 103, 117–120], monitoring of brain perfusion and blood oxygenation[108, 110, 113, 121, 122], detection of brown adipose tissue[111], temperature imaging[123], and renal MRI and MR spectroscopy (MRS)[112]. To be able to use DPXe as a probe for tissue anatomy and/or function, one has to be able to identify reliably spectral lines based on their chemical shift. Historically, the chemical shift of DPXe has been measured with respect to the xenon gas-phase resonance[100, 108, 124–127]. However, referencing the DPXe peaks to the gas phase presents several pitfalls: First, depending on the specific organ/tissue investigated, the gas phase may not always be visible in the acquired spectra; Second, even when visible, the gas-phase chemical shift is sensitive to several factors that, as recently pointed out[128], typically vary during an MR experiment, including level of lung inflation and partial pressure of the different gases in the lungs[72, 73, 129, 130]; Lastly, because the gas-phase and the dissolved-phase signals originate from tissue compartments

or organs with different magnetic properties, local magnetic fields experienced by these two phases are expected to be very different such that, even if the relative gas concentration in the lungs were known and could be kept constant during an experiment, macroscopic magnetic susceptibility gradients would make the dissolved-phase frequency highly variable[131].

To alleviate the problem, one might consider minimizing macroscopic field variations by adding higher-order magnetic field gradients, a process usually referred to as "shimming". Magnetic field shimming is applied in almost every MR experiment as a standard procedure for increasing field homogeneity within the sample, thus optimizing the SNR of the acquired signal, to the point where all modern spectrometers are capable of running an automated, sequence-specific shimming routine for most experiments. When dealing with DPXe experiments, however, shimming conditions can be optimized either for the dissolved phase (by shimming the tissue region of interest with the local ^{1}H signal) or the gas phase (by shimming on the gas phase peak, which is the predominant peak observed *in vivo* upon gas inhalation), but not both[126]. As a result, it is not surprising that variable DPXe chemical shift values have been reported in the literature (Table 4.2), making the identification of the source of some of these peaks very challenging.

In this chapter, we first analyze the effect of macroscopic susceptibility gradients on the gas-phase referenced DPXe chemical shift using numerical simulation methods similar to those in previous studies[132–135]. We then propose an alternative ^{1}H-based reference for the DPXe spectrum that, unlike the gas phase, leads to DPXe chemical shift values that are immune to variations in field strength, lung oxygenation, and shimming conditions. The consistency of the DPXe chemical shift values obtained by using this ^{1}H-based reference is then tested *in vivo* in rats at 9.4 T and finally used, in combination with high resolution *in vitro* spectroscopic measurements, to identify the origin of some of the DPXe peaks observed *in vivo*.

Table 4.2: Summary of DPXe chemical shift values and their assignments found in the literature.

Study	Investigation	Peak position (ppm) (assignment)				
Swanson, *et al.* [125]	Rat (body)	192 (epicardial fat)	—	—	199 (tissue)	210 (blood)
Duhamel, *et al.* [85]	Rat (head)	—	—	194 (intravascular)	199 (brain)	194.0±1.0 (intravascular)
Duhamel, *et al.* [136]	Rat (head)	—	—	194.5 (lipid emulsion)	19 (brain tissue)	194.0±1.0 (intravascular)
Wakai, *et al.* [137]	Rat (body)	189 (epicardial fat)	—	—	199 (tissue)	212 (blood)
Nakamura, *et al.* [127]	Rat (head)	188.8-189.5 (non-brain)	192	194.5-195.2 (brain)	198	210 (blood)
Kilian, *et al.* [107]	Human (head)	—	192-194 (white matter)	195.5-197.5 (gray matter)	–	–
Kershaw, *et al.* [126]	Rat (head)	187-192 (jaw muscle and/ or fat tissue)	191-194 (white matter)	193-197 (gray matter)	197-201 (jaw muscle and/ or fat tissue)	216 (blood)
Zhou, *et al.* [138]	Rat (head)	189 (non-brain)	191.6	194.7 (brain)	197.8	209.5 (blood)
Mazzanti, *et al.* [108]	Rat (head)	189 (non-brain tissue)	191.6	194.7 (gray matter)	197.8	209.5 (blood)
Rao, *et al.* [122]	Human (head)	187-189 (soft muscular tissue)	192-192.7 (white matter)	195.4-196 (gray matter)	199-200 (interstitial fluid/plasma, fat tissue, CSF)	217 (blood)

4.2 Methods

4.2.1 Human Susceptibility Model

A human susceptibility model was constructed from a 3D computed tomography (CT) data set of the human body acquired in a healthy human volunteer under approval of the Institutional Review Board at the University of North Carolina at Chapel Hill and conducted in accordance with the Helsinki Declaration. CT images were acquired with a resolution of $0.91 \times 0.91 \times 1.5$ mm^3 by using 5 bed positions to cover a region from the crown of the head to the lower abdomen. The 3D image dataset was thresholded with a cutoff value of -400 HU to separate the soft tissue from airspaces using VivoQuant software (Invicro, Boston, MA). Each region was then assembled into a standard tessellation language mesh using 3D Slicer open-source software (http://www.slicer.org)[139]. In preparation for finite-element analysis simulations, the mesh models were reconstructed into watertight surfaces using screened Poisson surface reconstruction[140] and quadratic edge collapse decimation, as implemented in MeshLab (http://www.meshlab.net)[141]. From the 3D human model, a 3D susceptibility map was generated by assigning a susceptibility value of -9.05 ppm to soft tissue and 0.36 ppm to air[142].

A 3D model of our high-pressure NMR tube assembly containing a sample of water was also created using Solidworks CAD software (Dassault Systémes SolidWorks Corp., Vélizy-Villacoubly, France).

4.2.2 Magnetic Susceptibility Field Calculations

The calculation of magnetic fields in general magnetostatic arrangements can be a complex task because of the presence of electric currents, non-linear constitutive relations, and the heavy dependence of magnetic fields on the geometry surrounding the region of interest. Fortunately, a number of simplifications can be made for the case of biological materials in a strong, static magnetic field. First, tissues and air fall within the realm of diamagnetic

and weakly paramagnetic materials, respectively. This means that the magnetic field $\vec{H}$ and magnetic flux density $\vec{B}$ are linearly related by the magnetic permeability μ and susceptibility χ_M:

$$\vec{B} = \mu\vec{H} = \mu_o(1 + \chi_M)\vec{H}, \tag{4.2}$$

where μ_o is the magnetic permeability of free space. Secondly, there are no constant electric currents in the tissue or air during the MR acquisition period (we ignore eddy currents that may arise in the scanner during magnetic field gradient switching in order to isolate susceptibility effects). The relevant macroscopic magnetostatic equations are then:

$$\vec{\nabla} \cdot \vec{B} = 0 \tag{4.3}$$

and

$$\vec{\nabla} \times \vec{H} = 0. \tag{4.4}$$

Analogous to the electrostatic case[143], we can then rewrite $\vec{H}$ as the gradient of a magnetic scalar potential Φ_M:

$$\vec{H} = -\vec{\nabla}\Phi_M. \tag{4.5}$$

Since the constituent relations in tissue and air are linear, we can substitute Equation (4.5) into Equation (4.4) to obtain

$$\vec{\nabla} \times \mu(-\vec{\nabla}\Phi_M) = \nabla^2\Phi_M = 0, \tag{4.6}$$

the familiar Laplace equation. The calculation is now reduced to a boundary-value problem with the boundary conditions between, say, regions 1 and 2, given by

$$\vec{H}_2 \cdot \hat{n} = \frac{\mu_1}{\mu_2}\vec{H}_1 \cdot \hat{n} \tag{4.7}$$

and

$$\vec{H}_2 \times \hat{n} = \vec{H}_1 \times \hat{n}. \tag{4.8}$$

These conditions require that the normal (Equation (4.7)) and tangential (Equation (4.8)) components of the magnetic field be continuous at the boundary[143, 144].

For simple geometries, where the boundary conforms to planar, spherical, or cylindrical surfaces, this boundary-value problem is exactly solvable by analytic methods following a separation of variables[145]; however, for complicated geometries, such as the human body, numerical methods must be employed. Therefore, the magnetic flux density within the human body model was computed by means of finite-element analysis calculations (COMSOL Multiphysics, Stockholm, Sweden). The computation was performed by axially aligning the 3D human model with an external static magnetic flux density of $B_0 = 3$ T in the $\hat{z}$ direction within a sphere of air 1.6 m in diameter. To avoid distortion in the field, the model was bounded by an infinite-element domain. The resulting boundary value problem was solved for the scalar magnetic potential Φ_M. In each domain i, the gradient of the scalar magnetic potential is then taken to calculate the magnetic field $\vec{H}_i$ and resulting magnetic flux density $\vec{B}_i = \mu_i \vec{H}_i$. Finally, the reduced magnetic flux density parallel to the applied static flux density was calculated for each domain by $\vec{B}_i \cdot \hat{z} - B_0$.

The same procedure was followed for the high-pressure NMR tube, only the static external field was set to 11.7 T (to mimic a 500 MHz spectrometer). A susceptibility value of -9.05 ppm, 0.36 ppm, and -8.58 ppm was used for water, air, and the ZrO_2 NMR tube, respectively.

4.2.3 *In Vitro* High-Resolution ^{129}Xe NMR Spectroscopy

High-resolution NMR measurements of thermally polarized ^{129}Xe dissolved in cerebrospinal fluid (CSF; Lee Biosolutions Inc., Maryland Heights, MO), excised rat white adipose tissue (WAT) and excised rat and mouse muscle were performed on a 500 MHz Varian Inova spectrometer (Varian NMR Systems, Palo Alto, CA). Samples were prepared by partially filling a high-pressure NMR tube (Daedalus Innovations, LLC, Aston, PA) with

either CSF, freshly excised WAT, or freshly excised muscle. The sample was then connected to a vacuum pump and frozen in liquid nitrogen. Air was removed with the aid of a rotary pump and the sample was thawed. The freeze-thaw cycle was repeated 3 times to remove any possible oxygen from the sample. After degassing, enriched ^{129}Xe gas (>86% isotopic enrichment) was introduced at a given pressure in the sample, which was then allowed to equilibrate for 24 hours under xenon atmosphere to a pressure of 1.04 atm (CSF), 1.03 atm (WAT), or 2.86 atm (muscle). Equilibrium pressures were kept low to avoid Xe-Xe dipolar interactions that could shift the DPXe frequencies. A slightly higher pressure was used for the muscle samples, given the lower solubility of xenon in muscle compared with WAT and the inability to shim the sample to a line width similar to that of CSF.

Samples were then placed in the NMR spectrometer and allowed to equilibrate for at least 1 hour at a temperature of 31.3°C (CSF), 31.0°C (WAT), or 30.8°C (muscle), regulated and maintained by a temperature controller. This temperature value was calibrated with an accuracy of 0.1°C at the beginning of each spectroscopy experiment by using the chemical shift separation between the methyl and hydroxyl protons in a 100% methanol temperature standard. Sample temperature was maintained at 31°C to enable direct comparison with the *in vivo* hyperpolarized ^{129}Xe MRS and chemical shift imaging (CSI) experiments described below.

All samples were manually shimmed using up to the 7th order z shim and 4th order x and y shims. The ^{129}Xe spectrum was acquired with a center frequency (CF) of 138.2675304 MHz (138.2694672 MHz for muscle), repetition time (TR) of 34.5 s (30.5 s for WAT, 30.1 s for muscle), spectral width (SW) of 60015 Hz, 524288 points (8192 for muscle), 500 averages (7200 for CSF and 5300 for muscle) and a 90° flip angle. Proton spectra were acquired before and after the acquisition of each ^{129}Xe spectrum (to ensure consistency) with a CF of 499.7835792 MHz, TR of 9 s, SW of 5998 Hz, 47984 points, 16 averages, and 23° flip angle. The chemical shift of the DPXe signal was then measured with respect to the water chemical shift as described below.

4.2.4 Method for Dissolved-Phase ^{129}Xe Referencing

Referencing of the DPXe frequencies to the ^{1}H water frequency was performed similarly to the method used by Zhang, *et al*. for *in vivo* absolute ^{129}Xe MR thermometry[146]. First, a ^{1}H spectrum was acquired to obtain a measurement of the water resonance frequency. This frequency was then scaled by 3.61529502, *i.e.* the ratio between the ^{129}Xe gyromagnetic ratio (γ_{Xe} =11.7767392 MHz/T) and ^{1}H gyromagnetic ratio (γ_H = 42.5763866 MHz/T)[7], to obtain a water-based 0 ppm ^{129}Xe center frequency, from which the experimental DPXe chemical shift was calculated. Figure 4.2 shows a cartoon of the referencing procedure. An example computation of how the chemical shift of the main peak observed in the rat head is also provided in Table 4.3. This water-based referencing method led to chemical shift values typically 4 ppm higher than those obtained by using the xenon gas phase as reference, at least *in vivo* from the rat head.

4.2.5 Dissolved-Phase ^{129}Xe MRS and CSI in Rats

All *in vivo* animal studies were conducted under animal protocols approved by the Institutional Animal Care and Use Committee at the University of North Carolina at Chapel Hill. For *in vivo* studies, a total of 4 male Fisher rats, age 8-10 weeks old, were used. Before the experiments, rats were anesthetized with a 60 mg/kg intraperitoneal injection of pentobarbital and intubated with a 20-gauge catheter. Rats were mechanically ventilated with approximately 25-vol% O_2 and 75-vol% N_2 using a home-built ventilator[147] at a rate of 60 breaths/min with a tidal volume of approximately 2 mL. Before the acquisition of xenon spectra, N_2 gas was replaced by an equivalent hyperpolarized (HP) ^{129}Xe gas volume. Following the experiment, animals were euthanized with an overdose of pentobarbital.

Xenon gas was polarized up to 14% with a commercial polarizer (Model 9800, Polarean, Inc., Durham, NC) using a gas mixture of 1% enriched xenon (>86% isotopic enrichment), 10% N_2, and 89% He (Global Specialty Gases, Bethlehem, PA). The polarizer oven temperature was maintained at 403 K with a presaturation region held at 438 K. Gas flow was regulated by

a mass flow controller to a rate of 1.5 standard liters per minute and cryogenically collected for 20 min. Frozen xenon was then sublimated into a 350 mL Tedlar bag (Jensen Inert Products, Coral Springs, FL) and connected to the ventilator.

In vivo MRS and MRI experiments were performed on a 9.4 T Bruker BioSpec 94/30 spectrometer (Bruker BioSpin, Billerica, MA) controlled by a console running Paravision software. Rats were placed with the anatomical region of interest in the sensitive region of a 1 cm diameter ^{129}Xe surface coil. The rat and the ^{129}Xe surface coil were then placed inside a 72 mm diameter ^{1}H volume coil, used to collect reference anatomical images and ^{1}H spectra. All ^{129}Xe acquisitions were triggered to the breathing cycle to optimize the DPXe signal to noise ratio. Rat rectal temperature was monitored by means of a fiber optic rectal temperature probe and maintained at 31°C by a forced heated-air system.

Anatomical axial ^{1}H images were collected by using a gradient echo multi-slice sequence with a field of view of 4 × 4 cm^2. Before the collection of ^{1}H and ^{129}Xe spectra, manual first and second order local shimming was performed to achieve narrow water linewidths (between 0.1 and 0.5 ppm, depending on the size and localization of the shimming voxel). ^{1}H spectra, without water suppression, were acquired using a point-resolved spectroscopy (PRESS) sequence from the same voxel before and after the acquisition of a xenon spectrum, performed by maintaining the same shimming conditions used for the acquisition of the ^{1}H spectra. ^{1}H and ^{129}Xe CSI was also performed in the rat head. ^{129}Xe CSI data were collected using the xenon surface coil with a field of view (FOV) of 4 × 4 cm^2, without slice selection, 8192 complex points, TR of 6 s, SW of 500 ppm, CF of 110.7532358 MHz, and CSI matrix size of 8 × 8. ^{1}H CSI data were collected using the ^{1}H volume coil with a FOV of 4 × 4 cm^2, 1 slice, 1 cm slice thickness, 2048 complex points, TR of 2 s, SW of 10 ppm, CF of 400.326207 MHz and CSI matrix size of 8 × 8. The CSI results of both nuclei were reconstructed to a matrix size of 16 × 16 using Paravision software.

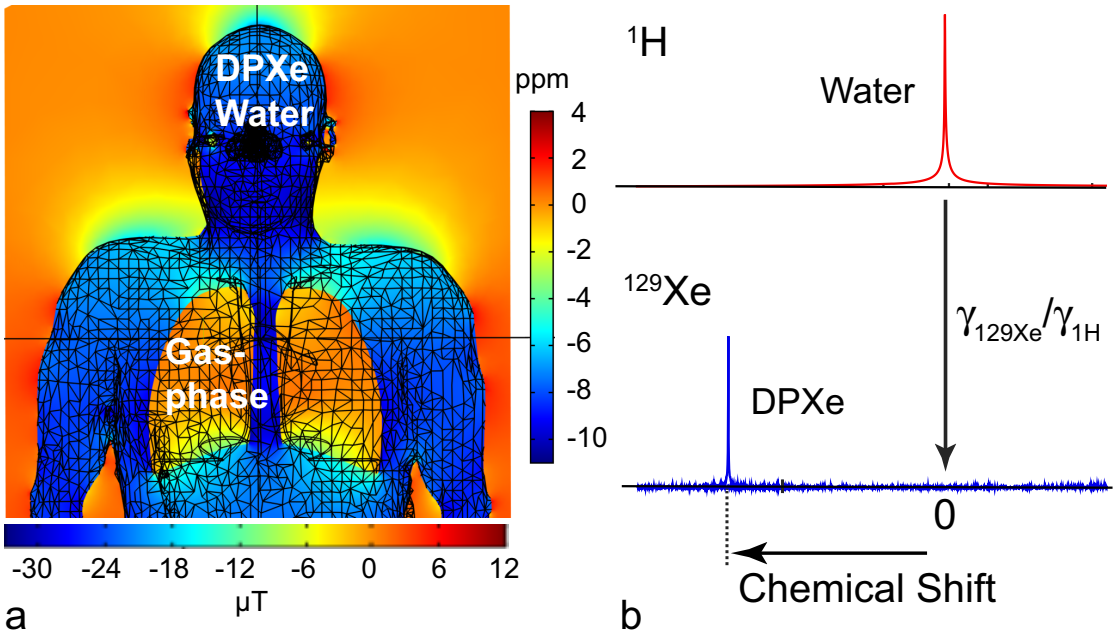

Figure 4.2: **a:** Susceptibility-induced frequency shift in the human body. **b:** Cartoon showing the proposed reference system for DPXe resonances. The 0 ppm reference in the xenon spectrum is obtained by scaling the water resonance frequency by the gyromagnetic ratios of the two nuclei. The DPXe chemical shift can then be measured with respect to this water-based reference. This referencing system eliminates the effect of macroscopic susceptibility gradients. An example of how chemical shift values are calculated is provided in Table 4.3.

4.3 Results

4.3.1 Susceptibility-Induced Frequency Shifts

A map of the reduced magnetic flux density and the induced frequency shift produced by magnetic susceptibility gradients between tissue and air in the human body is shown in Figure 4.2. This map outlines the challenge associated with trying to use the gas phase as a reference for the DPXe frequency. For example, at 3 T, the DPXe signal originating from brain tissue experiences a local field up to 24 μT lower than that experienced by the gas phase in the lungs or nasal cavities. This field difference produces an apparent difference in chemical shift between the gas phase in the lung and the DPXe in the brain of up to 6.5 ppm, a shift comparable to the frequency shift observed across different dissolved-phase xenon signals.

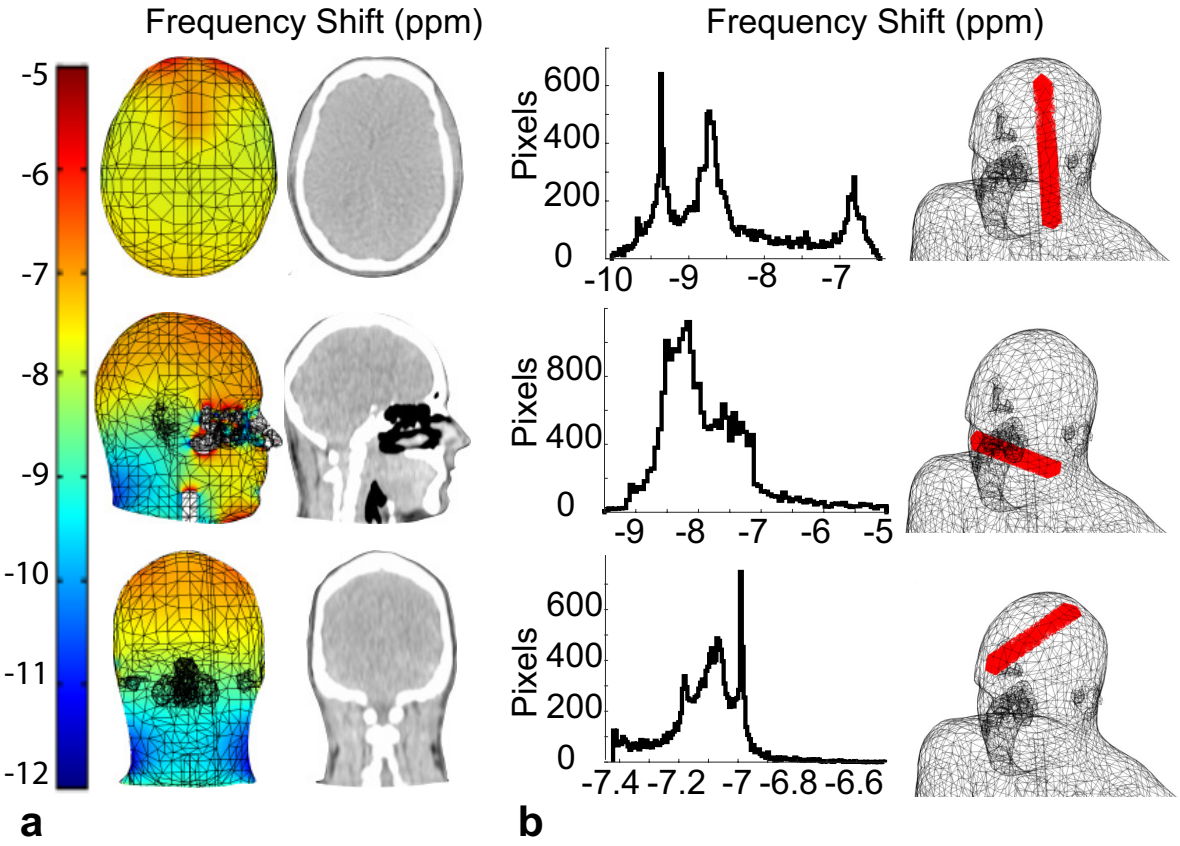

Figure 4.3: **a:** Representative maps (left column) of the frequency shift induced by magnetic susceptibility gradients at 3 T in the human head along with (right column) corresponding original CT slices used in the model. In CT slices, white represents bones, gray represents soft tissue, and black represents air. **b:** Histograms of frequency shift (left) present within the highlighted voxels shown in the 3D human head rendering (right). Note that anatomical features of the model located in front of the planes and voxels of interest are visible in the model rendering.

Table 4.3: Summary of the experimental frequencies measured in all 4 rat brains.[a]

Subject	Water (MHz)	^{129}Xe gas (MHz)	DPXe (MHz)	Water-based DPXe reference (MHz)	Gas-ref DPXe CS (ppm)	Water-ref DPXe CS (ppm)
Rat 1	400.3263440	110.7315642 –110.7317303	110.7532861	110.7313037	194.6 -196.1	198.5
Rat 2	400.3261221	110.7315811	110.7532519	110.7312459	195.7	198.7
Rat 3	400.3264150	110.7316491	110.7533335	110.7313269	195.8	198.7
Rat 4	400.3262054	110.7315610 –110.7316060	110.7532815	110.7312689	195.9 -196.3	198.8

[a]The water ^{1}H resonance frequency, the xenon gas-phase frequency (because this peak was quite broad, a range of chemical shift (CS) values is provided), the primary DPXe peak (previously attributed to gray matter) frequency and the water-based DPXe reference. The water-based DPXe reference was calculated by dividing the water resonance frequency by 3.6152950216. The last two columns report the DPXe chemical shift calculated with respect to the water-based DPXe reference and the gas-phase reference.

Figure 4.3a shows axial, sagittal, and coronal views of the frequency shift produced by magnetic susceptibility gradients in the human head, as well as the corresponding CT slices showing the details of the skull, nasal cavity, brain, and throat. These maps show that, across the human head, if shimming is not applied, macroscopic susceptibility gradients can produce apparent frequency shifts of up to 3 ppm, depending on the region analyzed. Figure 4.3b shows the frequency distribution for individual voxels previously selected to investigate the origin of DPXe resonances in the human head[122]. The field and frequency distributions are particularly inhomogeneous for individual spectra acquired near the nasal cavity or for those encompassing the brain from top to bottom. Across the brain, macroscopic susceptibility gradients can produce an apparent frequency shift between 1.5 and 2 ppm, of the same order of magnitude as variations observed experimentally for the DPXe peaks in the human head by Rao, *et al.* [122]. For comparison, Figure 4.4 shows a reduced magnetic flux density map in the high-pressure NMR tube when it is partially filled with a sample of water.

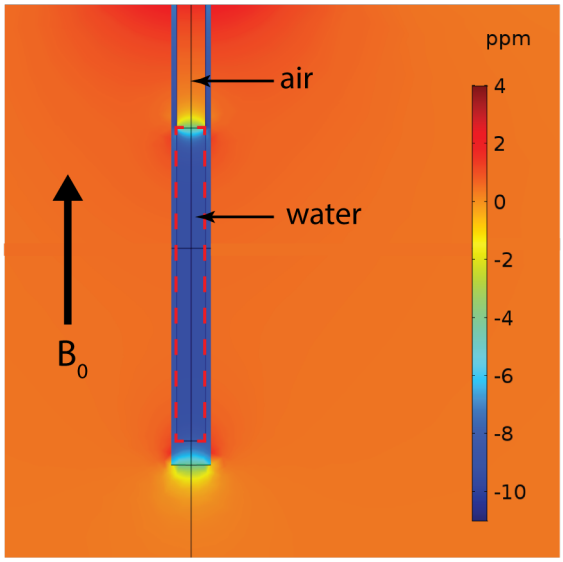

Figure 4.4: Reduced magnetic field map of a sample of water in a 5 mm NMR tube placed in a high (11.7 T) magnetic field. Notice that near the boundary of the water sample (denoted by red dashed outline) the static field B_0 can be distorted by over 10 ppm. NMR measurements in these regions will result in shorter $T_2^\star$ coherence times and hence much broader NMR spectral lines than in the center of the sample where the field is very uniform.

4.3.2 *In Vivo* MRS in Rats

Figure 4.5 shows representative xenon spectra acquired from the head of one of the rats at 34°C and 37°C. In addition to the gas phase peak and the red blood cell (RBC) peak, these spectra show 3 additional peaks, with only one of them shifting by an average of -0.2 ppm/°C. The location of these peaks with respect to the gas phase and the water-based xenon reference is shown in Table 4.4, along with a summary of previous peak assignments. Table 4.5 reports the chemical shift value of the major peak attributed to xenon in the brain for all rats analyzed. Experimental resonance frequencies from which the chemical shift values were calculated are reported in Table 4.3. As is clear from Table 4.5, our reference system provides consistent chemical shift values, whereas the gas-phase reference provides chemical shift values that varied by more than 1.5 ppm across the 4 animals. In this case, smaller variations, on the order of 0.3 ppm, were observed also across spectra acquired in the same animal under different shimming conditions.

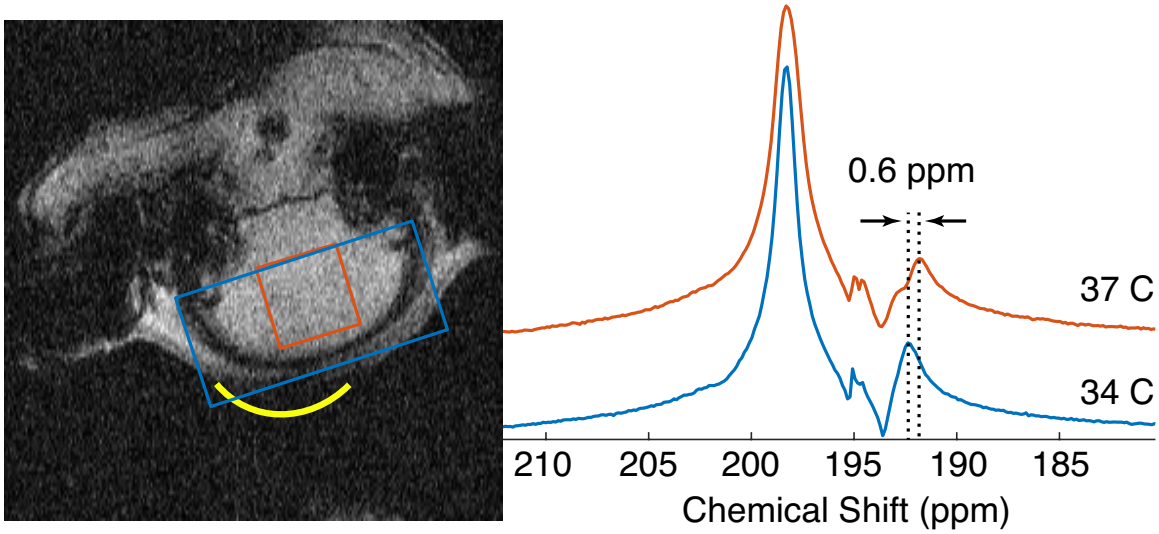

Figure 4.5: Representative *in vivo* xenon spectra obtained from the head of one of the rats at 34°C and 37°C. Chemical shift values are reported with respect to the water-based xenon reference calculated from the water resonance frequency measured in the region of interest. Only the peak at 193 ppm shows a clear upfield shift with increased temperature. Also shown are the anatomical regions from which the reference ^{1}H spectra were acquired after a manual shimming procedure (blue ($5 \times 5 \times 5$ mm^3) and orange ($7 \times 15 \times 14$ mm^3) boxes corresponding to the 34°C and 37°C spectra, respectively), and the location of the xenon surface coil (yellow line). A larger reference region was used in the 34°C spectrum to better resolve the lipid peak.

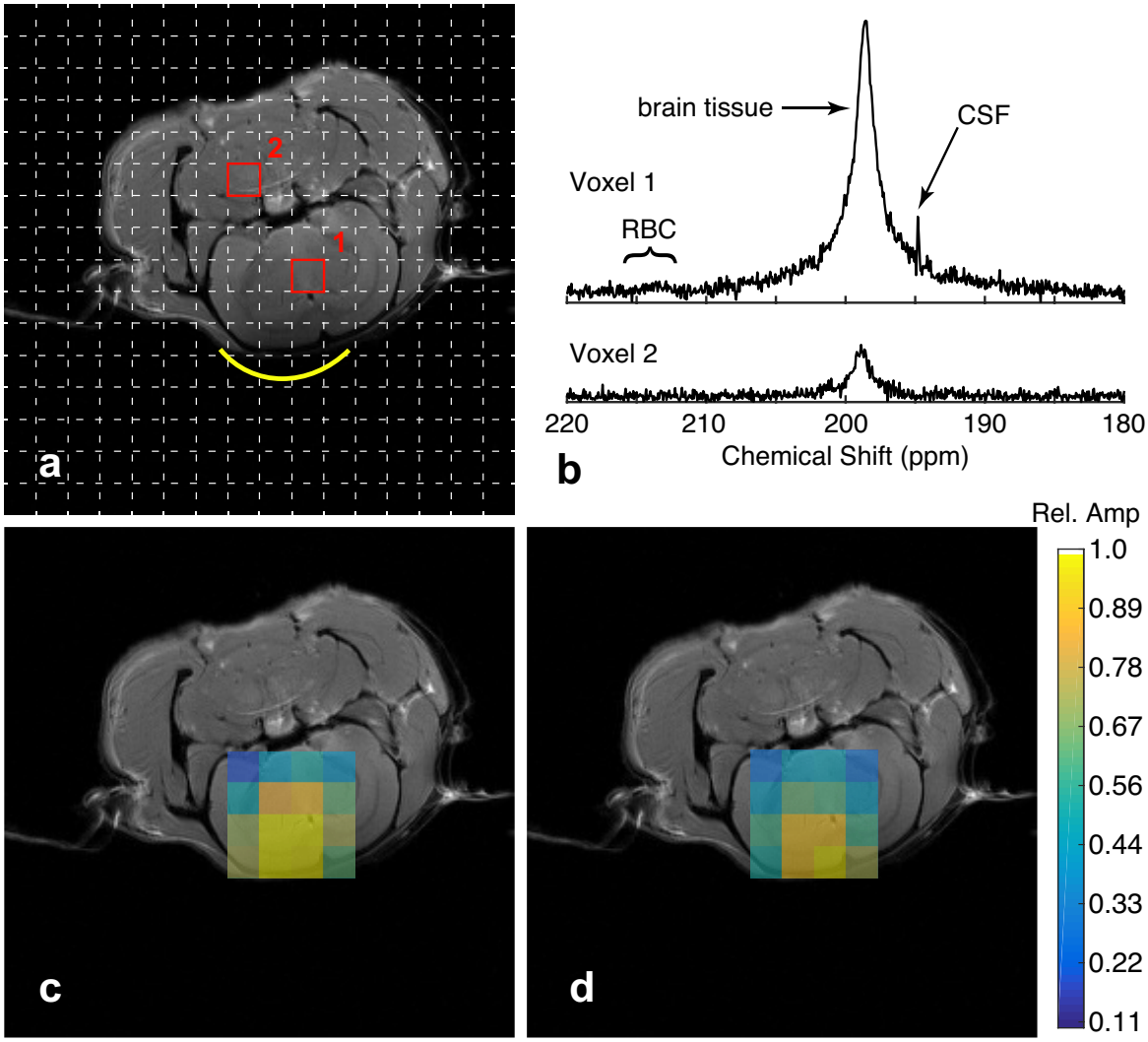

Figure 4.6: Xenon CSI maps in the rat brain. **a:** CSI matrix depicting two representative voxels, one inside (1) and one outside (2) the brain, along with (b) the ^{129}Xe spectra referenced to the water protons in each voxel. **c,d:** CSI maps of the primary brain (c) and CSF (d) peaks. The color scale depicts the peak amplitude relative to the maximum peak in each map.

Table 4.4: Summary of the chemical shift of the major *in vivo* DPXe peaks observed in this study and their assignments.[a]

Chemical Shift (ppm) *Gas-referenced*	Chemical Shift (ppm) *Water-referenced*	Previous peak assignments	Peak assignments from this study
189.9@31°C and 188.7@37°C	192.9@31°C and 191.8@37°C	Jaw muscle, fat	Fat
192.3	194.9	Brain tissue, white matter	CSF
195.7-196.2	198.7	Brain tissue, gray matter	Brain tissue, gray matter, maybe other tissues
195.6[b]	198.8	—	Muscular tissue, plasma
199.3[b]	202.5	Fat tissue	Muscular tissue
210-212	213-214	Red blood cells	Red blood cells

[a]Chemical shift values are reported with respect to the gas phase and to our water-based reference, obtained by scaling the water resonance frequency. Chemical shift uncertainties are ±0.1 ppm unless indicated otherwise. Included is a summary of previous peak assignments.
[b]Since no gas-phase ^{129}Xe signal was present in the *in vivo* muscle spectrum, these gas-referenced values were estimated by taking the chemical shift difference between the water-referenced DPXe chemical shift values for these peaks and the primary brain tissue peak, and adding the gas-referenced DPXe chemical shift value for gray matter as reported in Rao, *et al*. [122].

Figure 4.6 shows representative spectra obtained from a voxel located inside the brain and a voxel located outside the brain (Figure 4.6a). In the voxel located inside the brain, only two major peaks are observed at 198.7 ppm and at 194.9 ppm (Figure 4.6b), previously attributed to DPXe in gray and white matter, respectively[122]. A very weak signal is observed in the voxel outside the brain, most likely due to leakage from strong signals originating from brain tissue[148]. Figure 4.6c,d show CSI maps of the relative amplitude of the brain/gray matter and CSF DPXe peaks, respectively. In both cases, the signal originates from the expected regions of the brain.

Figure 4.7 shows representative xenon spectra acquired from different locations on the rat, along with xenon spectra acquired *in vitro* in CSF and in excised WAT and muscle. The anatomical regions and ^{129}Xe surface coil positions for each *in vivo* spectrum are given

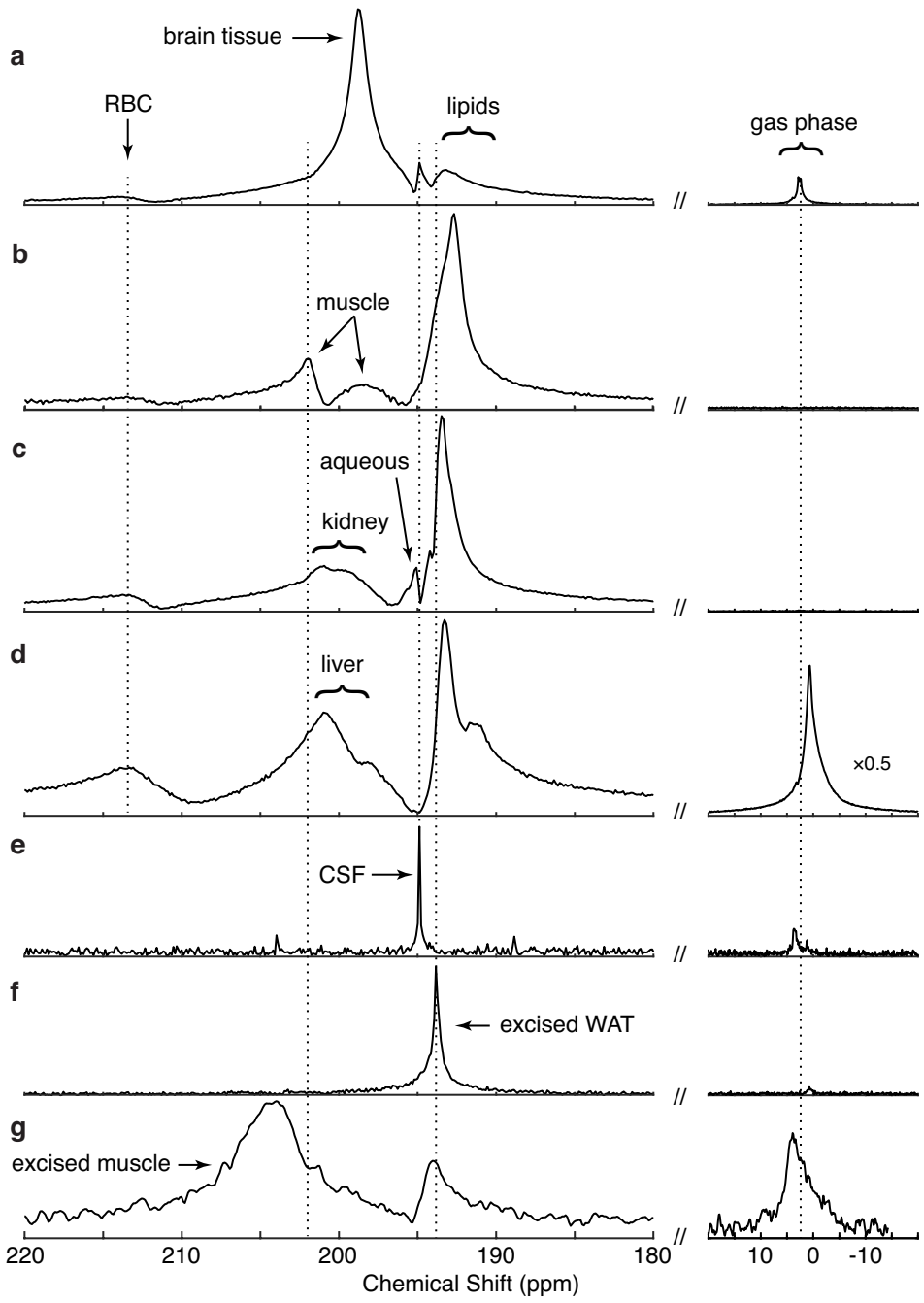

Figure 4.7: *In vivo* and *in vitro* DPXe spectra. **a-d:** Show representative DPXe spectra acquired *in vivo* from the rat head, leg muscle, kidney, and liver, respectively. All chemical shifts were calculated using the water-based ^{129}Xe reference calculated from the ^{1}H PRESS signal acquired from the voxels shown in Figures 4.8 and 4.9. **e-g:** DPXe spectra acquired *in vitro* in samples of CSF, excised rat white adipose tissue, and excised rat muscle, respectively. *In vitro* spectra corroborate the peak identification of CSF at 194.9 ppm and lipids at 193 ppm *in vivo* and 193.8 ppm *in vitro* at 31°C. Liver and kidney spectra show broad peaks centered around 200-202 ppm that may have contributions from muscle outside of the homogeneous field region as well as unidentified compartments within each organ.

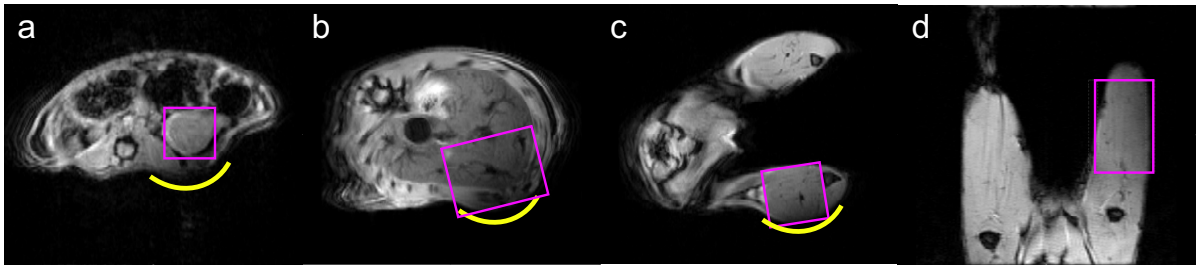

Figure 4.8: Regions of interest analyzed for the acquisition of rat (a) kidney, (b) liver, and (c,d) leg DPXe spectra. ^{1}H spectra were acquired from the voxels outlined in magenta, after a manual localized shimming procedure, using a ^{1}H PRESS sequence, right before the acquisition of ^{129}Xe spectra. ^{129}Xe spectra were acquired with a 90°-acquisition sequence with the use of a surface coil, whose position is indicated by the yellow line. The anatomical image for the liver (b) was acquired *post mortem* since movement of the diaphragm significantly distorted the liver image.

in Figures 4.8 and 4.9. In the rat leg, four peaks are clearly visible: two prominent peaks, located at 193 ppm and 202.5 ppm, and two small, broad peaks, located at 198.8 ppm and at 214 ppm, the latter known to originate from DPXe in RBC. Comparison of the *in vivo* spectra with the *in vitro* spectra acquired from excised muscle and adipose tissues (Figure 4.10) clearly indicates that the peak at 193 ppm (originally reported at 188-189 ppm from the gas phase[122]) originated from xenon dissolved in fat, not muscle. Also, the shift of this peak observed in the rat head spectra acquired at the two different temperatures is consistent with the previously measured temperature-induced shift of the chemical shift of xenon dissolved in lipids[146].

Table 4.5: Chemical shift values of the major peak observed from the heads of all rats.[a]

Subject	Chemical Shift (ppm) *Gas-referenced*	Chemical Shift (ppm) *Water-referenced*
Rat 1	194.6-196.1	198.5±0.1
Rat 2	195.7	198.7±0.1
Rat 3	195.8	198.7±0.1
Rat 4	195.9-196.3	198.8±0.1

[a]Chemical shift values are reported with respect to the xenon gas phase and our water-based reference, calculated from the resonance frequency of water protons. The gas phase in Rats 1 and 4 was split into multiple peaks giving a range of possible chemical shift values.

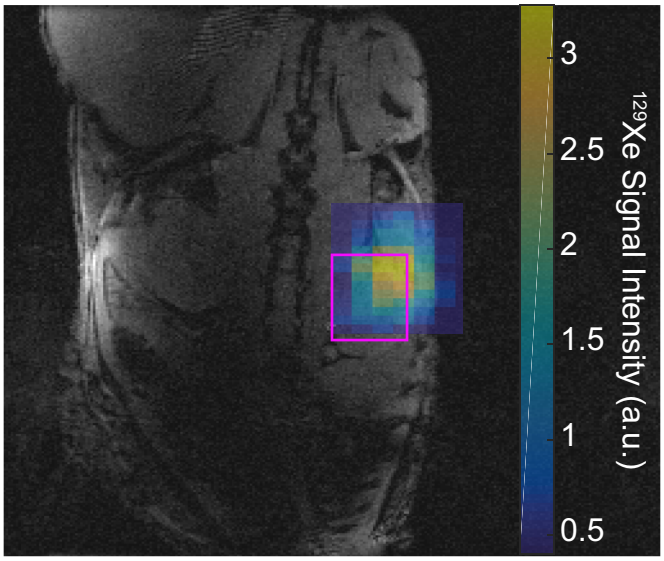

Figure 4.9: ^{1}H anatomical coronal image of the rat kidney with DPXe gradient-echo image overlay. The magenta box outlines the shimmed region. Notice that most of the DPXe signal originates from a region within the kidney.

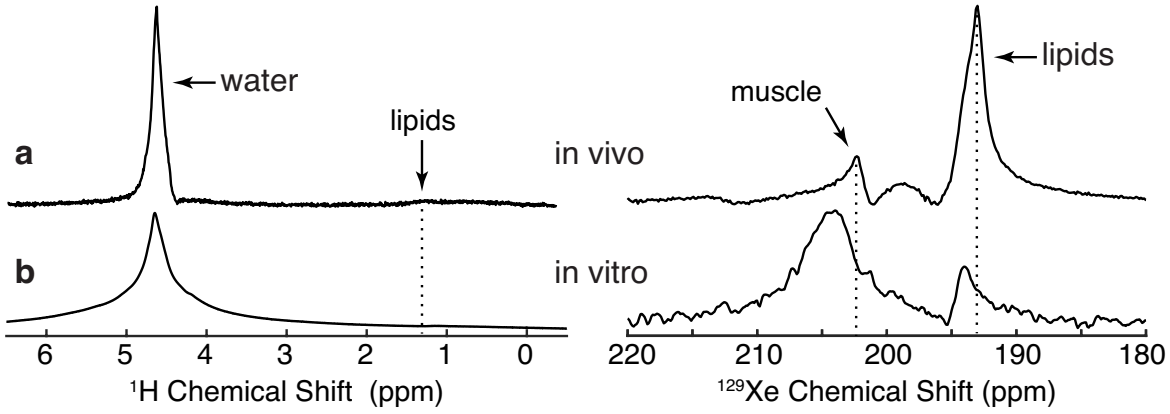

Figure 4.10: Comparison of *in vivo* and *in vitro* ^{1}H and DPXe muscle spectra. **a:** *In vivo* ^{1}H (left) and ^{129}Xe (right) muscle spectra. **b:** *In vitro* ^{1}H (left) and ^{129}Xe (right) muscle spectra acquired with a sample of excised muscle placed under 2.86 atm of xenon gas. Note that all spectra were acquired by optimizing shim conditions for the water protons. The use of a 3 atm xenon pressure for the *in vitro* studies produced a downfield shift of the DPXe lipid peak, as expected based on the previously reported pressure dependence of this peak[146]. Likewise, the muscle DPXe peak *in vitro* is shifted downfield from the *in vivo* peak by approximately 1.5 ppm, most likely because of a pressure dependence of the DPXe muscle peak (see Figure 4.12) and *post mortem* changes in muscular structure and/or chemistry. A very broad peak centered at around 198.8 ppm can also be seen in the DPXe spectrum.

Because the peak at 193 ppm can be confidently assigned to xenon dissolved in lipids, the peak at 202.5 ppm and the broad peak at 198.8 ppm, the only other peaks seen in the spectra from the rat leg and not seen in the spectra from excised adipose tissue, can only be assigned to xenon dissolved in muscle. *In vitro*, the peak at 202.5 ppm appears to be much broader and shifted slightly downfield, while the broad peak at 198.8 ppm was only visible in the spectrum acquired from excised mouse muscle. These differences between the *in vivo* and *in vitro* muscle spectra may be due to *post mortem* changes in tissue structure and composition.

Similarly, by comparing the *in vivo* brain spectra to the spectra acquired *in vitro* from CSF samples, we can identify the peak at 194.9 ppm (downfield 192 ppm from the gas phase and 3.9 ppm from the major peak) observed in the rat head spectra as coming from CSF.

4.4 Discussion

To take full advantage of the sensitivity of the DPXe chemical shift to the chemical environment *in vivo* in tissues, a robust referencing system needs to be established. As showed by our simulations, the gas-phase peak represents a sub-optimal reference; when the DPXe peaks are referenced to the gas-phase peak, magnetic susceptibility gradients can produce apparent variation in the chemical shift values that make comparison between *in vivo* xenon spectra very difficult (see Table 4.2). In addition, considering that *in vivo*, in tissues, the chemical shift of DPXe resonances spans a range of $\sim$15 ppm, these variations prevent us from recognizing peaks originating from the same tissue/organ, or from exploiting the sensitivity of some of the DPXe chemical shifts to monitor important physiological parameters such as blood oxygenation[104, 149] or tissue temperature[146].

Magnetic susceptibility gradients can also negatively affect the apparent chemical shift of DPXe peaks, even within the same organ. A variation of approximately 2 ppm, similar to the one recently reported in the human head by Rao, *et al.* [122], was indeed computed just across the human brain. Although *in vivo* shimming is typically applied to reduce some

of these frequency variations, because shimming can only be optimized either for the gas phase or the dissolved phase, but not both, some of these frequency variations are expected to remain.

In this study, we showed that the effect of macroscopic susceptibility gradients can be mitigated by referencing the DPXe resonances to that of nearby water protons. By using water protons in close physical proximity as a reference for the DPXe peaks, consistent chemical shift values for the DPXe resonances were obtained. In addition, we could directly compare spectra acquired from different tissues/organs or spectra acquired *in vivo* with those acquired *in vitro*. These comparisons have proven to be indispensable to correctly identify the origin of common and uncommon xenon peaks in spectra acquired *in vivo*.

Specifically, in addition to the broad peak at 213-214 ppm, which is well-known to originate from xenon dissolved in red blood cells, we were able to identify three additional peaks: one around 193 ppm, one broad peak around 198.8 ppm, and one around 202.5 ppm. The first peak, which corresponds to the peak seen between 187 and 189 ppm in Mazzanti, *et al*. [108], Zhou, *et al*. [138], Nakamura, *et al*. [127], and Rao, *et al*. [122] in spectra acquired from rat and human heads, was previously attributed to non-brain tissue and jaw muscle. In this study, comparison of *in vivo* spectra with *in vitro* spectra chemical shift values obtained from xenon dissolved in adipose tissue clearly shows that this peak originates from regions outside the brain and, specifically, from xenon dissolved in subcutaneous fat. The chemical shift of this peak nicely matches the chemical shift previously measured for xenon dissolved in adipose tissue in our lab[109], as well as the major peak seen from brown adipose tissue in humans during stimulation of thermogenesis[111] (see Table 4.6).

Not surprisingly, this peak is very broad or can appear to be split in multiple components, when shimming conditions are optimized for the water signal[122]. For example, Figure 4.11 shows a comparison of ^{1}H and DPXe spectra in the rat liver with shimming conditions optimized for water and then fat. When shimmed on water, the DPXe spectrum presents only a broad resonance for ^{129}Xe dissolved in fat since the magnetic field in these compartments is

Table 4.6: Comparison of chemical shift values of DPXe in rat white adipose tissue at 31°C as reported in Zhang, *et al.* [146] and as recalculated using the method presented in this work.[a]

Ratio γ_H/γ_{Xe}	Fictitious ^{1}H Reference (MHz)	Fictitious DPXe Reference (MHz)	DPXe (MHz)	**Water-ref DPXe CS (ppm)**
3.6152 (Zhang, *et al.*)	499.7822039 (methylene shifted to +1.3 ppm)	138.2453734	138.26852987	**166.2**
3.61529502 (this work)	499.7845279 (water on resonance)	138.2416995	138.26852987	**194.1**

[a]For chemical shift values reported in Zhang, *et al.* the values γ_{Xe}=11.777 MHz/T and γ_H=42.576 MHz/T were used for the ^{129}Xe and ^{1}H gyromagnetic ratios, whereas the current work uses the values γ_{Xe}=11.7767392 MHz/T and γ_H=42.5763866 MHz/T. The difference in the precision of the values used accounts for the difference in the proton-referenced chemical shift values at 31°C.

distorted. When shimmed on fat, the DPXe spectrum reveals ^{129}Xe dissolved in multiple compartments, with some likely outside the volume of interest since the splitting is not observed in the localized ^{1}H spectrum. Additionally, the 0.2 ppm/°C temperature-induced upfield shift seen in one of the rats is consistent with the temperature-induced shift of xenon dissolved in adipose tissue used previously for *in vivo* temperature imaging in mice[146]. The small frequency variations seen in this peak across the *in vivo* spectra are more likely indicative of a temperature gradient present in the anesthetized rat. For example, the same peak appears to have a small upfield shift in the spectrum collected from the rat leg, which was placed right next to the heating hose inside the magnet. *In vitro* experiments, where temperature could be more precisely controlled and shimming conditions optimized for the methylene peak, place the lipid DPXe peak more accurately at 193.8 ppm at 31°C (see Table 4.7).

The identification of the peak at 193 ppm as a peak originating from xenon dissolved in adipose tissue leads to the identification of the two peaks at 202.5 ppm and 198.8 ppm as originating from muscle tissue. While the peak at 202.5 ppm, elsewhere reported at 199-200 ppm downfield from the gas-phase resonance, was previously identified as originating

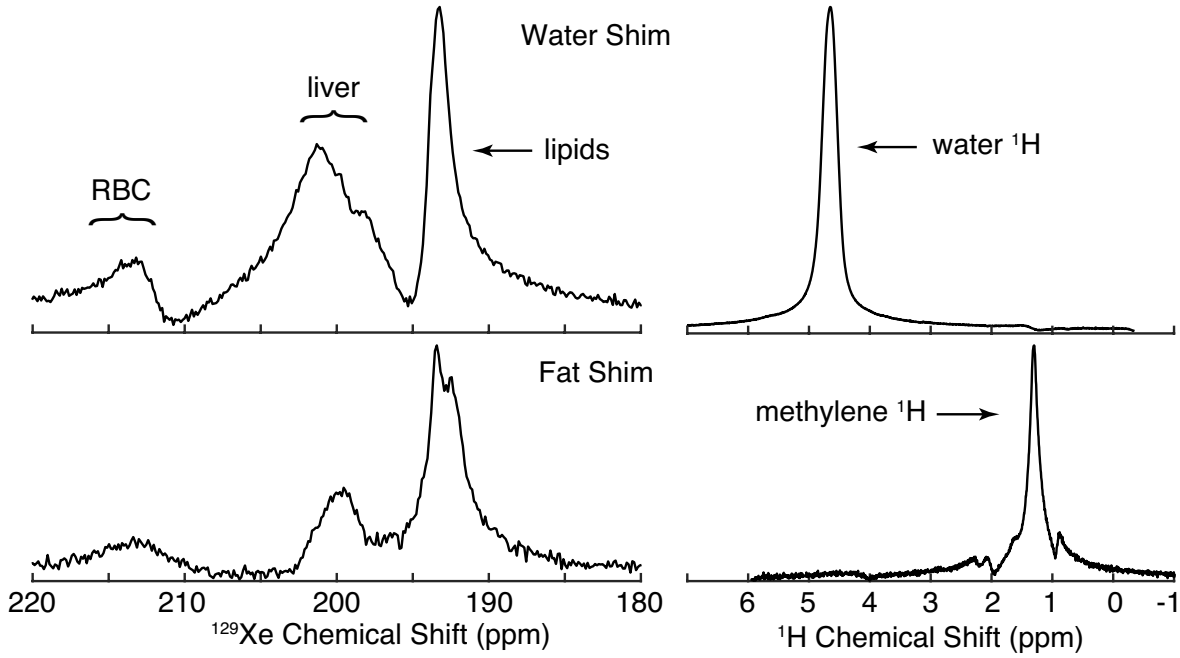

Figure 4.11: Comparison of ^{1}H PRESS spectra and single-pulse acquisition DPXe spectra in a rat liver, with shimming conditions optimized either for water (top) or fat (bottom) signal. For the ^{1}H PRESS spectra (right), narrow bandwidth refocusing pulses were used to suppress the fat (water) signal in the top (bottom) spectrum. Shimming conditions were found to strongly affect the shape of the DPXe spectrum. We believe that the splitting of the peak at 193 ppm found when shimming on the fat proton signal is most likely due to the presence of different lipid compartments in which xenon dissolves. Since this splitting is not observed in the ^{1}H PRESS spectrum obtained from the shimmed voxel, one could speculate that, while one peak originates from xenon spins dissolved in the lipid compartments within the shimmed voxel, the other peak originates from xenon dissolved in the surrounding fat tissues.

Table 4.7: Comparison of lipid peaks from *in vivo* and *in vitro* experiments.[a]

Animal	**Organ**	**Lipid CS (ppm)**	**FWHM (ppm)**	**RMS error (%)**
rat 1	brain	193.14	0.52	17.20
	kidney	193.04	1.03	7.96
	liver	193.23	1.19	5.94
	muscle	193.16	1.65	5.48
rat 2	brain	193.02	0.56	7.80
	kidney	193.31	1.03	9.11
	liver	193.28	1.16	8.30
	muscle	194.07	1.29	7.52
rat 3	brain	193.00	0.55	9.10
	kidney	193.38	0.93	6.63
	liver	191.32	2.01	5.94
	liver	193.22	0.90	5.94
	muscle	194.12	1.82	6.86
rat 4	brain	193.35	0.67	10.20
***in vitro* tissue sample**	**Xe pressure (atm)**	**Lipid CS (ppm)**	**FWHM (ppm)**	**RMS error (%)**
olive oil	1.30	193.91	0.21	2.53
rat WAT	1.03	193.79	0.61	3.58
rat muscle	6.35	194.15	2.40	3.23
rat muscle/WAT	$\sim$3	193.75	0.04	2.30
rat WAT	1.00	193.77	0.36	5.06
rat WAT	0.50	193.75	0.35	3.91

[a]Comparison of lipid peaks from *in vivo* and *in vitro* experiments. All lipid peaks were fit with a Voigt profile in MATLAB using an iterative least-squares algorithm. RMS error indicates the RMS difference, in percent, between the fitted Voigt lineshape and data in the fitted spectral region. Some *in vivo* regions were composed of a main peak with a sizable shoulder on the upfield side of the peak, likely from contributions outside of the shimmed ROI. Most likely, small temperature gradients present across the anesthetized rat body also contributed to the small variation in the chemical shift of the lipid peak.

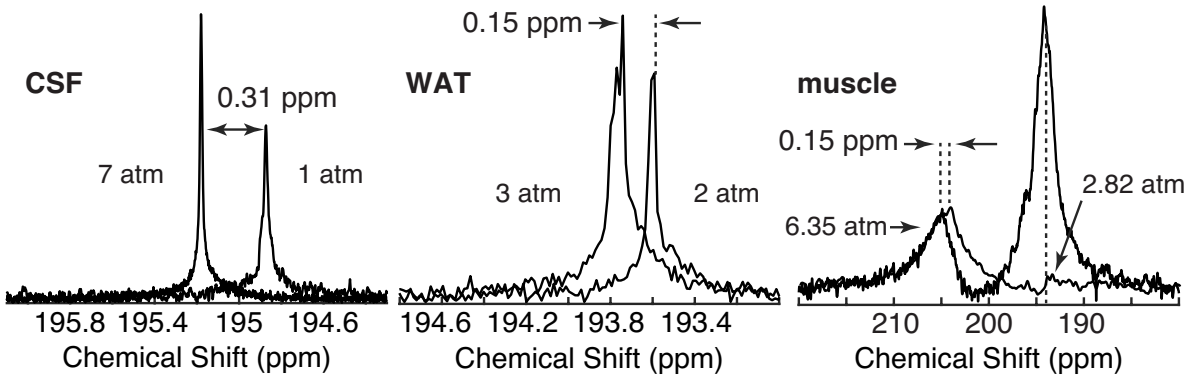

Figure 4.12: Pressure-induced frequency shift measured *in vitro* for xenon dissolved in human CSF, rat WAT, and rat muscle. The pressure-induced shift of the DPXe chemical shift seems to strongly depend on the tissue in which xenon dissolves. For example, the average shift seen in CSF was only about 0.05 ppm/atm, whereas in muscle it was about 0.27 ppm/atm.

from xenon dissolved in interstitial fluid, plasma, fat tissue, and jaw muscle[122, 126], the peak at 198.8 ppm has never been reported. Because these are the only two peaks seen in the rat leg spectrum, along with the peaks attributed to xenon dissolved in fat and RBC, we can confidently assign these two peaks to xenon dissolved in muscle tissue, although a contribution from xenon dissolved in plasma for the 198.8 ppm peak cannot be excluded.

The peak at 194.9 ppm corresponds to the peak observed between 191 and 194 ppm and assigned to white matter plus blood plasma in Kershaw, *et al*. [126], and between 192 and 192.7 ppm and assigned to white matter in Rao, *et al*. [122]. Comparison of *in vitro* spectra acquired in CSF samples and *in vivo* rat head spectra strongly suggests that this peak originates or has contribution from xenon dissolved in CSF. This peak, which *in vivo* can derive from passive diffusion of xenon across the blood-CSF barrier, was indeed visible only in voxels located within the brain that contained the lateral ventricles in our rat head CSI studies and in the human head CSI studies by Rao, *et al*. [122]. Naturally, the assignment of the peak at 194.9 ppm to xenon dissolved in CSF raises the question of where the peak corresponding to xenon dissolved in white matter is. Unfortunately, high-resolution spectroscopy studies of excised brain tissue, which were tried in our lab, could not help in this case because spectra from excised brain tissue presented a single, very broad resonance frequency line. This resonance frequency line, like the resonance frequency of xenon dissolved

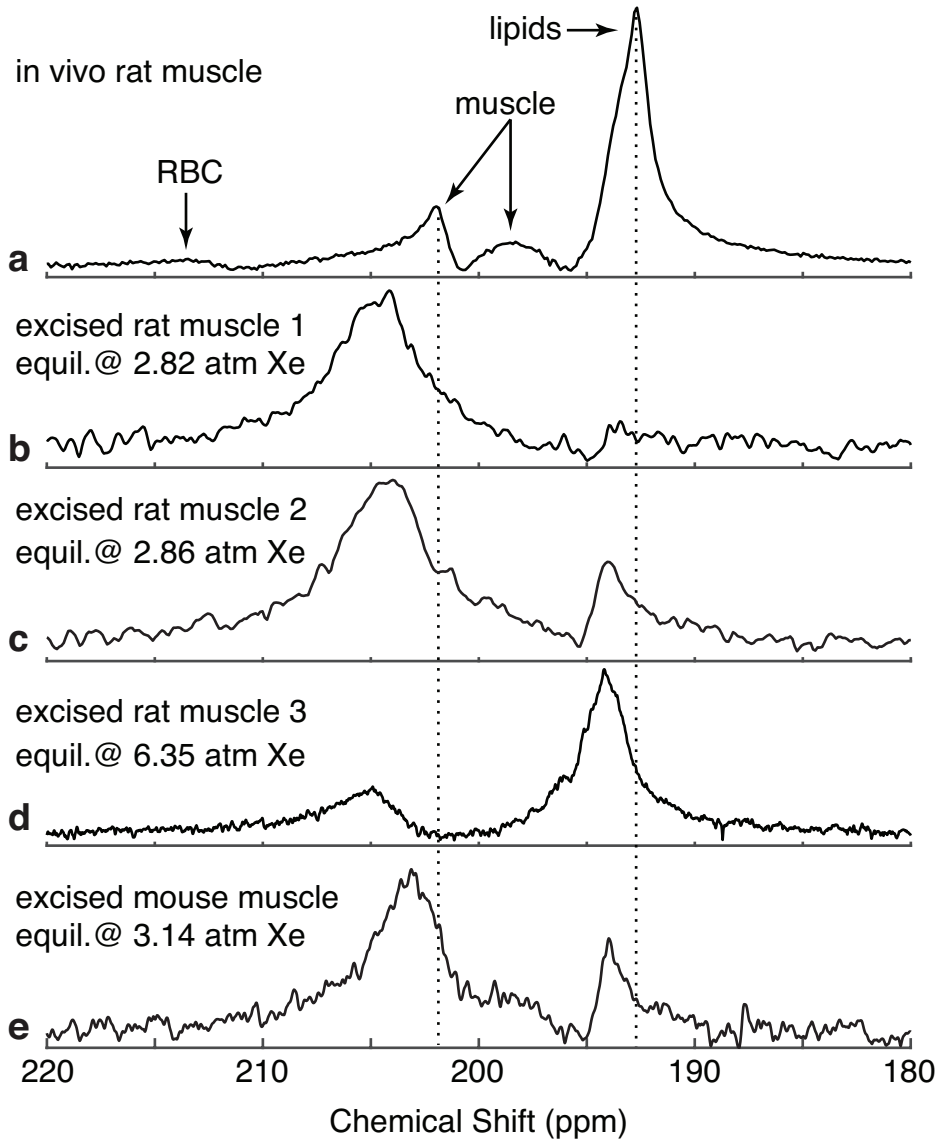

Figure 4.13: Comparison of (a) DPXe spectrum obtained *in vivo* from rat muscle, to DPXe spectra obtained from excised muscle tissue from different rats euthanized with CO_2 (b-d) and from a mouse euthanized with pentobarbital (e). The *in vivo* spectrum clearly shows 4 peaks: one from xenon dissolved in RBC, one from xenon dissolved in lipids (interestingly, *in vivo*, this peak is shifted slightly upfield, possibly because the temperature of the rat leg, situated close to the heating hose, was slightly higher than the rat rectal temperature), and two from xenon dissolved in muscle. These two peaks are extensively broadened in the *in vitro* spectra and have a slightly higher chemical shift, possibly due to a *post mortem* change in tissue structure and/or chemistry. Also, given that the broad peak at 198.8 ppm is about 15 ppm upfield from the RBC, based on the previous literature report, we cannot exclude some contribution from xenon dissolved in plasma.

in excised muscle, was much broader than the frequency lines observed in the corresponding ^{1}H spectra, indicating possible fast exchange of xenon dissolved in different compartments whose structure and/or chemistry was probably compromised *post mortem* during excision (Figures 4.12 and 4.13).

4.5 Conclusions

Macroscopic susceptibility gradients produce large shifts in the apparent chemical shift of DPXe resonances and prevent correct identification and assignment of peaks that can be found in xenon spectra acquired from different animals or organs. By referencing the DPXe chemical shift to that of nearby water protons, we can remove the effect of macroscopic susceptibility gradients and obtain consistent chemical shift values for xenon signals originating from the same organ or tissue compartments. Such a referencing system allows us to compare directly chemical shift values obtained *in vivo* to those obtained *in vitro* from excised tissue or biological samples, and to identify correctly the origin of several peaks observed *in vivo*.

CHAPTER 5: DEPENDENCIES OF LIPID-DISSOLVED XENON CHEMICAL SHIFT

Results in this section have been published in the journal *Magnetic Resonance in Medicine*.[1]

5.1 Introduction

Temperature, one of the most fundamental physical properties of matter, is extremely hard to measure non-invasively *in vivo*. The temperature dependence of the resonance frequency of water protons (PRF) is linear between 25°C and 110°C with a slope of -0.01 ppm/°C [150, 151]. In high resolution NMR spectroscopy, one can leverage this temperature dependence to track accurately temperature changes[152] as well as to calibrate variable temperature control systems for future experiments[153, 154].

Since the temperature dependence of the chemical shift of water protons is nearly independent of tissue type[155], it has been used *in vivo* to monitor changes in temperature in tissues[155, 156]. This method is known as the proton resonance frequency shift method, or PRFS.

If the water ^{1}H frequency is referenced to an internal temperature-insensitive frequency, absolute temperature can be measured. This method has been successfully applied in the brain where N-acetylaspartate (NAA) serves as the temperature-insensitive reference for water protons[157–163] (see literature review in Ref. [164] for comparison of non-human *in vivo* and phantom *in vitro* studies).

[1]Antonacci MA, Zhang L, Degan S, Erdmann D, Branca RT. Calibration of methylene-referenced lipid-dissolved xenon frequency for absolute MR temperature measurements. *Magnetic Resonance in Medicine* 2019; 81:765-772. DOI: 10.1002/mrm.27441.

The PRFS has likewise been applied to monitor relative temperature change during high-intensity focused ultrasound thermal ablation of cancerous tumors[165] in the breast[166, 167], liver[168–171], and kidney[171–173]. However, precise absolute temperature measurements are difficult in regions outside the brain for a number of reasons: First, even for relative temperature measurements, an internal signal that is robust to temperature change must be present; Second, shimming conditions *in vivo* result in spectral line widths orders of magnitude wider than in high resolution NMR; Finally, magnetic susceptibility gradients *in vivo* can distort line shapes to the point where uncertainty in the peak centroid overshadows the shift due to temperature change. This effect can even be magnified in the presence of fat, as the magnetic susceptibility of fat is temperature dependent, making magnetic susceptibility gradients also temperature dependent[174].

Nowhere are these effects more prominent than in lipid-rich regions like brown adipose tissue, where lipid droplets of various sizes are dispersed in the cell cytoplasm[146, 175]. Although some have used the methylene signal from the lipids as a useful temperature-insensitive reference for water protons, the difference in magnetic susceptibility between the lipid and water compartments, along with the relatively strong temperature dependence of the magnetic susceptibility of fat[176], produce local magnetic field gradients that result in a temperature inaccuracy of several degrees Celsius[135, 146, 164, 174, 177–179]. As a result, it is not surprising that very different temperature calibrations of the water-methylene resonance frequency have been reported over the years[180–182]. Although at the macroscopic level one could think of using shim gradients to rectify the effect of magnetic susceptibility gradients, in practice this can only be done either for the water or the lipid compartment, but not for both (see Figure 5.1, for example).

Recently, it was shown that the resonance frequency of ^{129}Xe dissolved in adipose tissue (AT), also called lipid-dissolved ^{129}Xe (LDX), had a strong linear temperature dependence (-0.2 ppm/°C) in the physiologically-relevant temperature range of 25-45°C [109, 178] and higher[183]. It was also suggested that, by referencing the LDX frequency to that of the

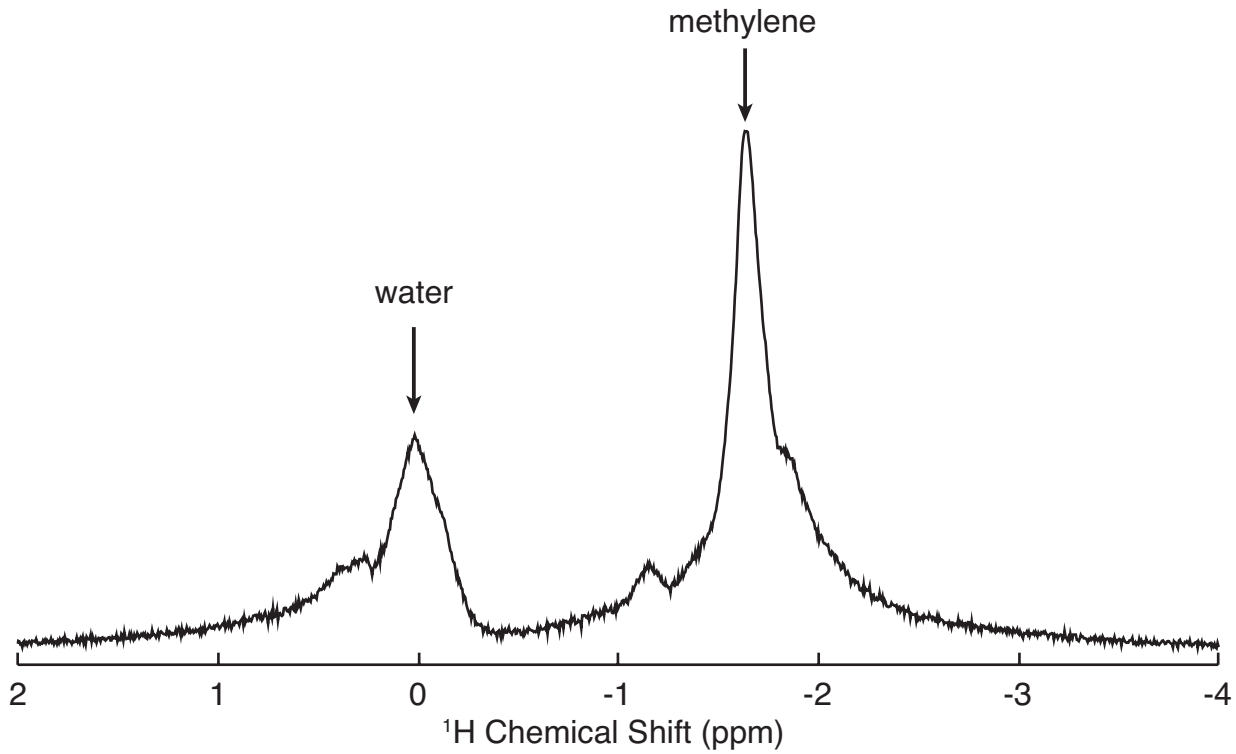

Figure 5.1: *In vivo* localized ^{1}H spectrum from the supraclavicular brown adipose tissue depot of a human subject. Notice how the methylene peak could be made relatively narrow and symmetric (*i.e.* the magnetic field in the lipid compartments is *more* uniform), whereas the water peak is broad and distorted (*i.e.* the magnetic field in the water compartments is *less* uniform). Motion from the subject's breathing further complicates the field correction procedure.

temperature-insensitive methylene protons in a volume in which xenon dissolves, absolute temperature information could be obtained[178]. Absolute temperature measurements could be valuable not only for calibration of more conventional MR thermometry methods used to monitor temperature during hyperthermia treatment of lipid-containing tumors[184], but also for the detection of thermogenic activity of brown adipose tissue (BAT), a tissue specialized in heat production that is currently being considered as a good target for the treatment of obesity and diabetes[185]. Considering that the LDX signal is the primary signal observed *in vivo* in hyperpolarized ^{129}Xe spectra of rodent[109] and human[111] BAT, measurements of absolute temperature by LDX could provide a direct window to BAT thermogenic activity which, so far, can only be detected indirectly via infrared thermography[186, 187]. However, because previous studies have reported differences in the chemical shift of xenon dissolved in different kinds of oils[81, 183], and considering that BAT temperature needs to be measured with an accuracy better than 1°C, the scope of this work was to investigate whether the methylene-referenced LDX (rLDX) signal also had a dependence on lipid composition that could affect the precision with which absolute temperature measurements can be made.

5.2 Temperature Dependence of the ^{129}Xe Chemical Shift

The temperature dependence of dissolved-phase ^{129}Xe has been observed experimentally and reported in the literature for various solvents since the 1980s[81]. Quantitative predictions for the chemical shift of ^{129}Xe in a given environment are often made by running detailed molecular dynamics[79, 82, 188–190] or quantum Monte Carlo[79, 191, 192] simulations of the thermodynamics of the system. However, a good qualitative understanding of the temperature dependence of the ^{129}Xe chemical shift in solution can be reached through a simplified quantum mechanical model of a ^{129}Xe atom trapped inside a rigid compartment. This section describes a simple model for the ^{129}Xe chemical shift when the atom is trapped inside a rigid cage, and then uses this model to explain the observed ^{129}Xe chemical shift's temperature dependence in the dissolved state.

A theoretical explanation for the origin of the chemical shift's temperature dependence of ^{129}Xe inside a rigid micropore was given by T.T.P. Cheung[193]. We begin here with a summary of Cheung's derivation. As we have already seen, the chemical shift of ^{129}Xe originates from the change in local magnetic field (deshielding) at the ^{129}Xe nucleus by surrounding atoms and molecules. In the dilute limit (*i.e.* no xenon–xenon interactions), the observed chemical shift $\delta_o(T)$ of ^{129}Xe depends on the potential $U(\vec{r})$ between the xenon atom and the surface of the micropore and the isotropic ^{129}Xe chemical shift $\delta(\vec{r})$, and is given by the canonical ensemble average:

$$\delta_o(T) = \frac{\int_V d\vec{r}\ \delta(\vec{r})\ \exp(-U(\vec{r})/kT)}{\int_V d\vec{r} \exp(-U(\vec{r})/kT)}, \tag{5.1}$$

where V is the volume of the micropore. The potential energy between a xenon atom and the atoms that make up the wall of the micropore can be modeled by the Lennard-Jones potential:

$$U_{L-J}(r) = -4\epsilon \left[\left(\frac{a}{r}\right)^6 - \left(\frac{a}{r}\right)^{12} \right], \tag{5.2}$$

where a is the sum of the van der Waals radii of the xenon and micropore surface atoms and ϵ is the depth of the potential well. The total potential, then, would be the pairwise sum of the potentials between the single xenon atom and all of the surface atoms in the micropore. For simplicity, consider the case of two parallel infinite sheets of identical atoms with center to center separation R enclosing a xenon atom (see Figure 5.2) with a being the sum of the van der Waals radii of the xenon and pore atoms. Integration over both sheets results in a potential given by

$$U(y) = -2(2\pi\epsilon n/5) \left[\frac{5(R/2a - y/a)^6 - 2}{(R/2a - y/a)^{10}} + \frac{5(R/2a + y/a)^6 - 2}{(R/2a + y/a)^{10}} \right], \tag{5.3}$$

where $-R/2 < y < R/2$ and n is the number of micropore surface atoms in the area a^2. In this case, the potential is solely a function of position in the y direction. $U(y)$ is plotted in Figure 5.3 for various ratios of R to a. Cheung points out that Kromhout and Linder[194]

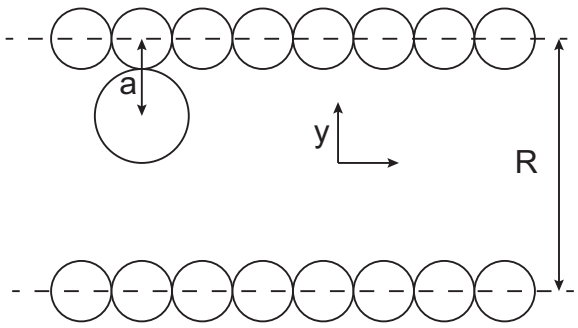

Figure 5.2: Diagram of a simple model of a micropore consisting of two infinite parallel planes of atoms separated by a distance R. The distance a is the sum of the xenon and pore wall atom van der Waals radii.

applied quantum mechanical perturbation theory to show that in closed-shell atoms, like xenon, chemical shift is proportional to the van der Waals interaction energy $W(\vec{r})$:

$$\delta(\vec{r}) = -cW(\vec{r}). \tag{5.4}$$

For the case of xenon and a surface atom, the first term of Equation (5.2) gives the van der Waals interaction energy. If we repeat the integration over both infinite layers with just this first term, we can rewite Equation (5.4) as

$$\delta(y) = 2\pi\epsilon nc \left[\frac{1}{(R/2a - y/a)^4} + \frac{1}{(R/2a + y/a)^4} \right]. \tag{5.5}$$

Importantly, Cheung notes that the potentials shown in Figure 5.3 are qualitatively similar to the case of xenon in a spherical micropore (see Figure 2 in Ref. [91]). Note also that for values of $R/a > 2.4$ the interaction potential begins to develop a bump at $y/a = 0$ and to split into two potential wells. Thus there are two discernible cases with very different dynamics: In one case, the micropore is small and on the order of the size of the xenon van der Waals diameter ($R/a < 2.4$), while in the other case the pore is large relative to the xenon van der Waals diameter ($R/a > 2.4$).

In the current work, we would like to consider xenon in solution rather than in a rigid cage and can leverage the first case ($R/a < 2.4$) of the model just described to explain

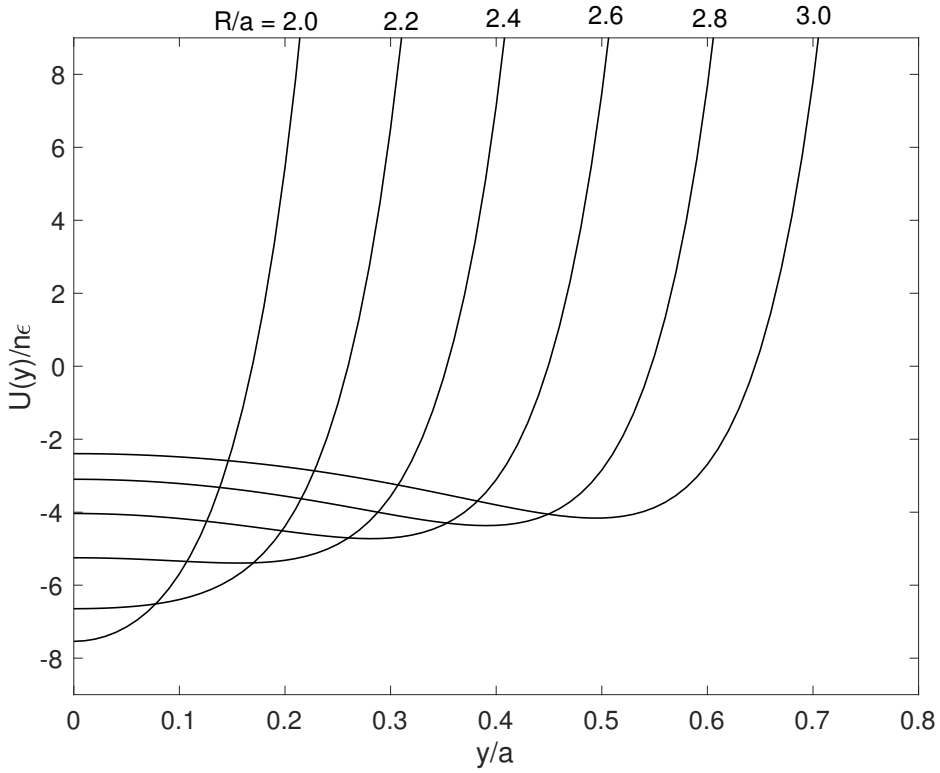

Figure 5.3: Plot of the potential function $U(y)$ (Equation 5.3) for xenon trapped between two infinite parallel sheets of atoms vs. position for various ratios of R to a.

the temperature dependence of dissolved-phase ^{129}Xe. Jameson, *et al.* [79] have studied the chemical shift of ^{129}Xe dissolved in liquids with molecular dynamics simulations that agree well with experimental results. In their work, they describe the system of xenon dissolved into a liquid in the dilute limit as a xenon atom "surrounded by a dynamic cage of solvent molecules." Unlike the rigid cage of micropores, solvent cages will change size as the temperature, and hence the density, of the solvent changes. As temperature increases, density decreases and solvent cages increase in volume, leaving ^{129}Xe more screened by its atomic electron cloud and thus with a reduced chemical shift. Jameson, *et al.* report that molecular dynamics simulations of ^{129}Xe dissolved in various liquids (water, alkanes, and perfluorooctyl bromide) show a corresponding decrease in ^{129}Xe chemical shift[79]. Experimental evidence of the reduction of ^{129}Xe chemical shift with increasing temperatures has indeed been found for ^{129}Xe dissolved in these liquids[79, 81, 195, 196]. To show that the temperature-induced decrease in density, thus increase in free volume available to ^{129}Xe, was the primary cause for the reduction in chemical shift, Jameson, *et al.* repeated their simulations holding the liquid density constant. In this case, the average ^{129}Xe chemical shift was left unchanged to within error demonstrating that change in density is the primary mechanism causing ^{129}Xe chemical shift to change with temperature.

The analytical model developed by Cheung can now be used to illustrate the inverse temperature dependence of the ^{129}Xe chemical shift if, instead of a rigid micropore, we assume a flexible solvent cage that expands with increasing temperature. This means that the length R in the denominator of Equation (5.5) would increase and the resulting average chemical shift $\delta(y)$ would decrease, and *vice versa*.

5.3 Materials and Methods

5.3.1 Sample Preparation

Samples of neat triglycerides (triolein (18:1), trielaidin (18:1T), trilinolein (18:2), trilinoelaidin (18:2T), tripalmitolein (16:1), and tripalmitelaidin (16:1T) (number of carbons:number of double carbon bonds, where T indicates *trans* isomers)), were obtained from NuChek Prep, Inc, Elysian, MN, while neat corn and olive oils were obtained from Sigma-Aldrich and whole kernel, unrefined coconut oil from Dr. Bronner's (www.drbronner.com). Rat and mouse AT samples were excised from the animals immediately following euthanasia. All animal studies were performed under protocols approved by the Institutional Animal Care and Use Committee at the University of North Carolina at Chapel Hill. Human AT samples were obtained after de-identification from 6 patients undergoing abdominoplasty/panniculectomy surgery. The surgically removed tissue was rapidly transported to a sterile hood for dissection of the AT using forceps and surgical scissors. The AT was then transported on ice to the facility housing the NMR spectrometer and samples were immediately prepared.

For NMR measurements, all samples were placed in a high-pressure NMR tube (Daedalus Innovations, LLC, Aston, Pennsylvania, USA) connected to a home-built vacuum pump system. Samples were frozen in liquid nitrogen, evacuated with a rotary pump, and thawed. This process was repeated 3 times to ensure that all oxygen was removed from the sample. Each sample was then equilibrated for 24 hours with >86% isotopically enriched ^{129}Xe gas to a pressure of about 1 atm in order to avoid Xe-Xe chemical shift contributions[178].

5.3.2 High-resolution NMR spectroscopy

Prepared oil, triglyceride and tissue samples were all studied by high-resolution NMR on a 500 MHz spectrometer (Varian NMR Systems, Palo Alto, California, USA). Samples were equilibrated for about 1 hour in the spectrometer at temperatures of approximately 25°C, 30°C, 35°C, and 40°C. Temperatures were maintained by a variable temperature controller

and calibrated with an accuracy of 0.1°C at the beginning of each spectroscopy experiment using a 100% methanol temperature standard.

All samples were manually shimmed using up to the 7th order z shim and 4th order x and y shims. Proton spectra were acquired before and after ^{129}Xe spectra in order to confirm consistent conditions throughout the ^{129}Xe acquisition. Proton spectra were acquired with a center frequency (CF) of 499.7828127 MHz, repetition time (TR) of 6 s, spectral width (SW) of 5998 Hz, 11996 points, 16 averages, and 6° flip angle. The proton TR was chosen to ensure full relaxation of triglyceride protons, since the proton spectra were also used to measure fat saturation, as described below. ^{1}H T_1 and T_2 measurements were also performed on the triglyceride peaks of interest in one human AT sample at 37°C and the data were processed on the spectrometer using VNMRJ software (Varian). ^{129}Xe spectra were acquired with a CF of 138.2672519 MHz, TR=26 s, SW=60015 Hz, 120030 points, 36 averages, and 46° flip angle.

5.3.3 Measurement of Triglyceride Saturation by ^{1}H NMR

For all samples, lipid saturation was measured as described in Refs. [197] and [198]. Briefly, the total unsaturated fatty acid (FA) content was calculated using the integrated areas of the spectral peaks of the allylic protons (A, at 2.03 ppm) and protons α to COO (B, at 2.25 ppm; αCOO). Unsaturated FA fraction was determined by

$$f_{unsat} = \frac{1}{2}\frac{A}{B}, \tag{5.6}$$

where the factor of 1/2 accounts for there being twice as many allylic protons than αCOO protons in each FA chain. Then, the fraction of saturated FAs was calculated from

$$f_{sat} = 1 - f_{unsat}. \tag{5.7}$$

5.3.4 Spectral Analysis and Estimation of Uncertainties

Proton spectra were processed by first applying an automatic phase correction method implemented in MATLAB (MathWorks, Natick, MA, USA)[199]. Both phased proton and magnitude ^{129}Xe spectra were fit in MATLAB using a non-linear, iterative algorithm to either Lorentzian or Voigt line shape models that incorporated linear or quadratic baseline correction[200]. Uncertainties in the methylene peak position were estimated from the fit results. Uncertainties in the measurement of triglyceride and neat oil saturation by ^{1}H NMR were calculated as the standard deviation of the measured saturation values at all temperatures. The uncertainties in saturation for human samples were calculated by adding in quadrature the maximum variation of measured saturation in pure triglyceride samples to the standard deviation of measured saturation values for the human samples at each temperature.

Temperature measurements by rLDX chemical shift were performed as described in previous work[178, 201]. Briefly, the water frequency, assumed to be 3.5 ppm downfield from the measured methylene frequency, was scaled by 3.61529502 (*i.e.* by the ratio of the gyromagnetic ratios of ^{1}H and ^{129}Xe) to find a fictitious 0 ppm reference for the rLDX chemical shift.

In order to calibrate accurately the temperature dependence of the rLDX chemical shift, each chemical shift measurement was plotted as a function of the sample temperature calibrated on the NMR spectrometer as described above. The final data were fitted to a linear model by the method described in Ref. [202] in order to appropriately weight the experimental uncertainties in temperature and chemical shift at each data point. The uncertainty of the final temperature calibration curve was calculated by first rearranging the rLDX chemical shift versus temperature fit to solve for temperature (see Figure 5.5 below), and then propagating, in quadrature, the standard errors in the calibrated temperature coefficient, chemical shift offset, and typical experimental chemical shift uncertainty of 0.02 ppm in the rLDX spectrum.

5.4 Results

5.4.1 Lipid Saturation by ^{1}H spectroscopy

The T_1 and T_2 values for the allylic protons were measured to be 0.629±0.007 s and 0.176±0.005 s, and for the αCOO protons were 0.672±0.021 s and 0.178±0.004 s, respectively. No T_1 or T_2 corrections were needed for quantitative analysis as observed $T_2^\star$ values were less than 0.035 s. Saturation values for all samples measured are shown in Table 5.1. Variations in measured saturation uncertainties in the human AT samples are the result of variations in the achievable field homogeneity, which led to varying degrees of overlap between the adjacent allylic and αCOO peaks.

Table 5.1: Fraction of saturated fatty acids in each sample as measured by ^{1}H NMR and corresponding rLDX frequency at 37°C.

Sample	Known fraction of saturated fatty acids	Measured fraction of saturated fatty acids	Uncertainty	rLDX frequency at 37°C (ppm)
18:1	0.00	0.010	0.015	192.51±0.02
18:2	0.00	-0.005	0.013	194.37±0.02
16:1	0.00	0.007	0.012	192.06±0.02
18:1T	0.00	-0.005	0.021	193.20±0.02
18:2T	0.00	-0.023	0.007	195.94±0.02
16:1T	0.00	0.007	0.024	192.80±0.02
Olive Oil	—	0.152	0.004	192.57±0.02
Corn Oil	—	0.129	0.009	193.57±0.03
Coconut Oil	—	0.966	0.006	188.73±0.02
Human AT 1	—	0.29	0.10	192.51±0.02
Human AT 2	—	0.25	0.09	192.60±0.02
Human AT 3	—	0.27	0.06	192.45±0.02
Human AT 4	—	0.24	0.02	192.54±0.02
Human AT 5	—	0.30	0.03	192.50±0.02
Human AT 6	—	0.19	0.09	192.56±0.02

5.4.2 ^{129}Xe Chemical Shift Dependence on Lipid Saturation in Neat Triglycerides and Oils

Plots of the rLDX chemical shift versus temperature in neat triglyceride and oil samples are shown in Figure 5.4. Although all of the triglycerides analyzed were unsaturated, substantial variation in the chemical shift offset is observed with varying hydrocarbon chain length, number of double bonds, and isomer. In the neat vegetable oil samples, the chemical shift offset seems also to vary with the degree of lipid saturation. Based on the measurements in pure unsaturated triglycerides, the chemical shift offset most likely depends on the composition of the unsaturated triglycerides in each of these oils (see the Discussion section below).

5.4.3 Absolute Methylene-referenced, Lipid-dissolved ^{129}Xe Temperature Calibrations in Human Adipose Tissue

Plots of the rLDX chemical shift versus temperature in AT samples collected from 6 different subjects, along with results from mouse and rat AT samples, are shown in Figure 5.5. Within the physiologically-relevant temperature range, the rLDX chemical shift is linear and the model best fit for the human data is δ =(-0.2058±0.0010 ppm/°C)×T+(200.15±0.03 ppm) when accounting for the individual measurement uncertainties, as described above. Rearranging and propagating the model standard errors, the temperature measurement by rLDX chemical shift is accurate to within 0.3°C.

5.4.4 Comparison with ^{1}H-methylene Absolute Thermometry

Lastly, we analyzed the accuracy of temperature estimation performed by using the previously reported relation between the ^{1}H-methylene frequency separation and temperature[180, 181] that have also been used *in vivo* to directly measure absolute temperature in human AT. Table 5.2 presents temperature measurements performed on human AT sample 6 at 5 different temperatures using the ^{1}H-methylene chemical shift separation method in the high-resolution NMR spectrometer. Interestingly, even under well-controlled conditions (thermally

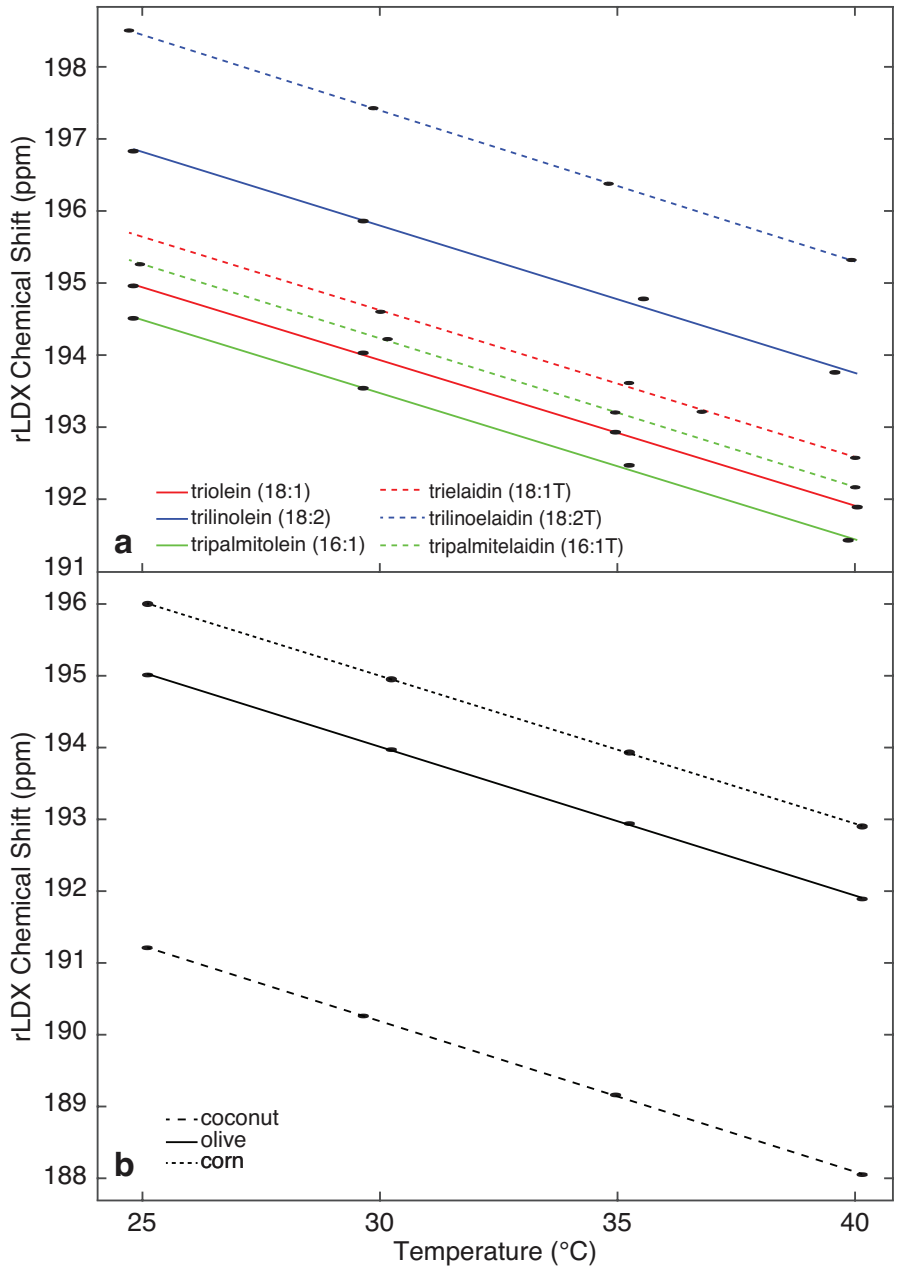

Figure 5.4: Plots of rLDX chemical shift versus sample temperature for neat (a) triglycerides and (b) vegetable oils. Experimental uncertainties for each measurement are indicated by elliptical regions around each point. Best fits for rLDX chemical shift curves for 18:1, 18:2, and 16:1 samples are (-0.2021±0.0025 ppm/°C)×T+(199.99±0.08 ppm), (-0.2045±0.0025 ppm/°C)×T+(201.93±0.08 ppm), and (-0.2031±0.0025) ppm/°C ×T+(199.57±0.08 ppm), respectively. Best fits for 18:1T, 18:2T, and 16:1T are (-0.2042±0.0042 ppm/°C)×T+(200.76±0.15 ppm), (-0.2101±0.0027 ppm/°C)×T+(203.71±0.09 ppm), and (-0.2066±0.0027 ppm/°C)×T+(200.44±0.09 ppm), respectively. Best fits for coconut, olive, and corn oils are (-0.2097±0.0026 ppm/°C)×T+(196.49±0.08 ppm), (-0.2073±0.0026 ppm/°C)×T+(200.24±0.09 ppm), and (-0.2059±0.0032 ppm/°C)×T+(201.18±0.11 ppm), respectively.

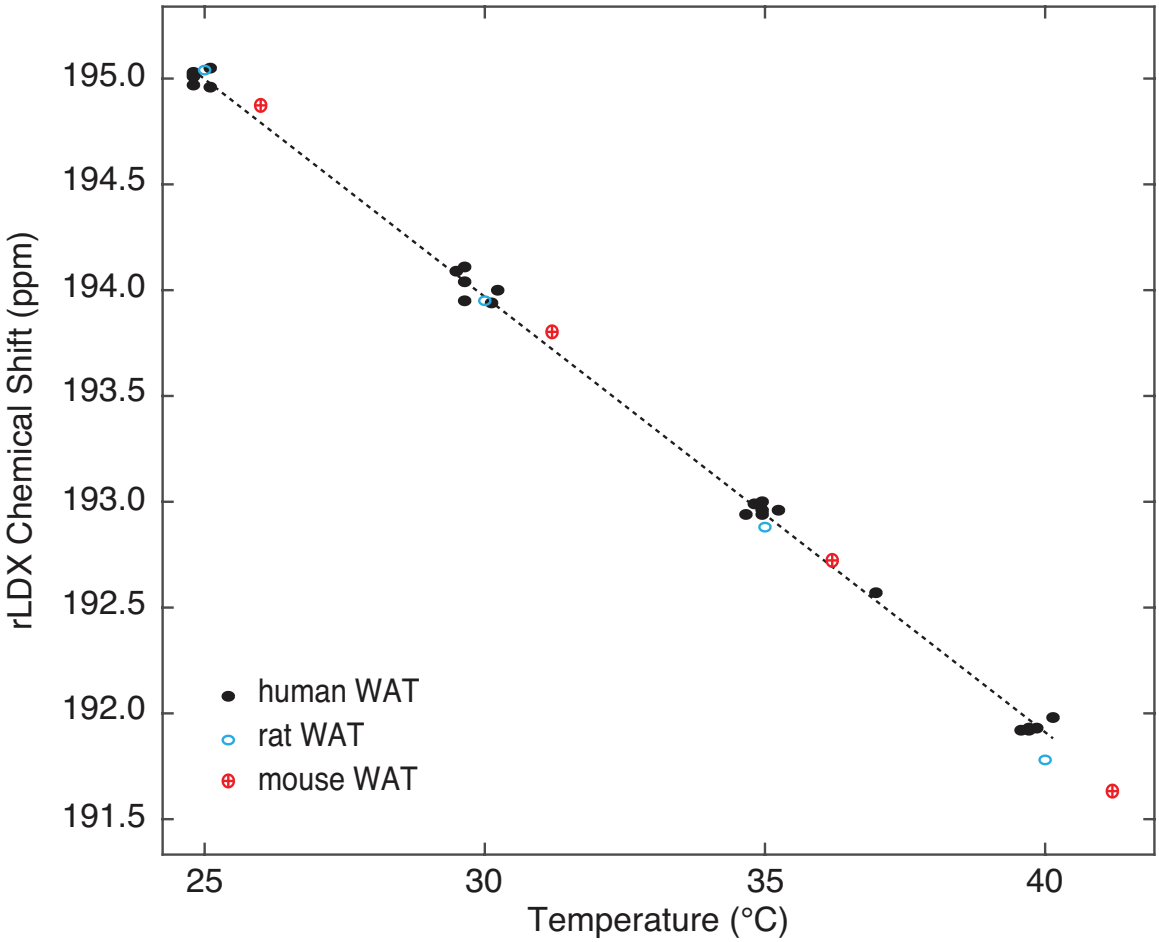

Figure 5.5: Plot of rLDX chemical shift versus temperature for all human AT samples, and comparison with rat and mouse AT samples. Experimental uncertainties for each measurement are represented by elliptical shaded regions. The fitted curve takes into account the experimental uncertainties at each point in both temperature and rLDX chemical shift resulting in a temperature dependence of (-0.2058±0.0010 ppm/°C)×T + (200.15±0.03 ppm) for human WAT. The absolute temperature calibration uncertainty, calculated by propagating the standard error in the temperature coefficient and chemical shift offset, and assuming an experimental rLDX chemical shift uncertainty of 0.02 ppm, is less than 0.3°C within the physiologically-relevant temperature range. The rat and mouse rLDX chemical shift temperature dependences are (-0.2170±0.0026 ppm/°C)×T+(200.47±0.09 ppm) and (-0.2135±0.0033 ppm/°C)×T+(200.44±0.11 ppm), respectively.

Table 5.2: Absolute temperature measurement values as obtained in human AT sample 6 by using the ^{1}H-methylene chemical shift temperature calibrations previously reported in the literature.

Sample temperature (±0.1°C)	^{1}H-CH_2 chemical shift separation (ppm)	Temperature (°C) (Kuroda[180])	Temperature (°C) (Hernando[181])	Temperature (°C) (rLDX method)
25.1	3.445	28.5±0.8	27.9±1.0	24.8±0.2
30.2	3.370	34.1±0.2	34.8±0.2	29.9±0.2
35.2	3.319	37.9±0.2	39.5±0.2	34.9±0.3
37.0	3.338	36.4±0.2	37.8±0.2	36.8±0.3
39.9	3.280	40.7±0.2	43.1±0.2	39.9±0.3

equilibrated and relatively homogeneous AT sample), the measured absolute temperature can vary from the calibrated sample temperature by over 4°C, depending on which ^{1}H-methylene chemical shift separation calibration is used.

5.5 Discussion

The rLDX chemical shift studies of triglycerides and neat oils clearly show that the rLDX chemical shift and its temperature dependence varies with the type of oil/triglyceride analyzed. The temperature dependence for triglycerides is close to -0.20 ppm/°C, whereas for neat oils it is slightly higher and close to -0.21 ppm/°C. Although the oils examined here have a wide range of lipid saturations, with high saturation producing lower rLDX chemical shift values, a bare dependence of rLDX chemical shift on the degree of lipid saturation does not seem to be sufficient to explain the observed variations in the chemical shift offset. We therefore examined the dependence of the rLDX chemical shift on other factors that varied between samples, including density, fraction of medium-chained fatty acids (6-12 C atoms), fraction of double carbon bonds (FDCB), and average hydrocarbon chain length (AHCL), as shown in Figure 5.6. Using literature values for the composition of the neat oils[203, 204]

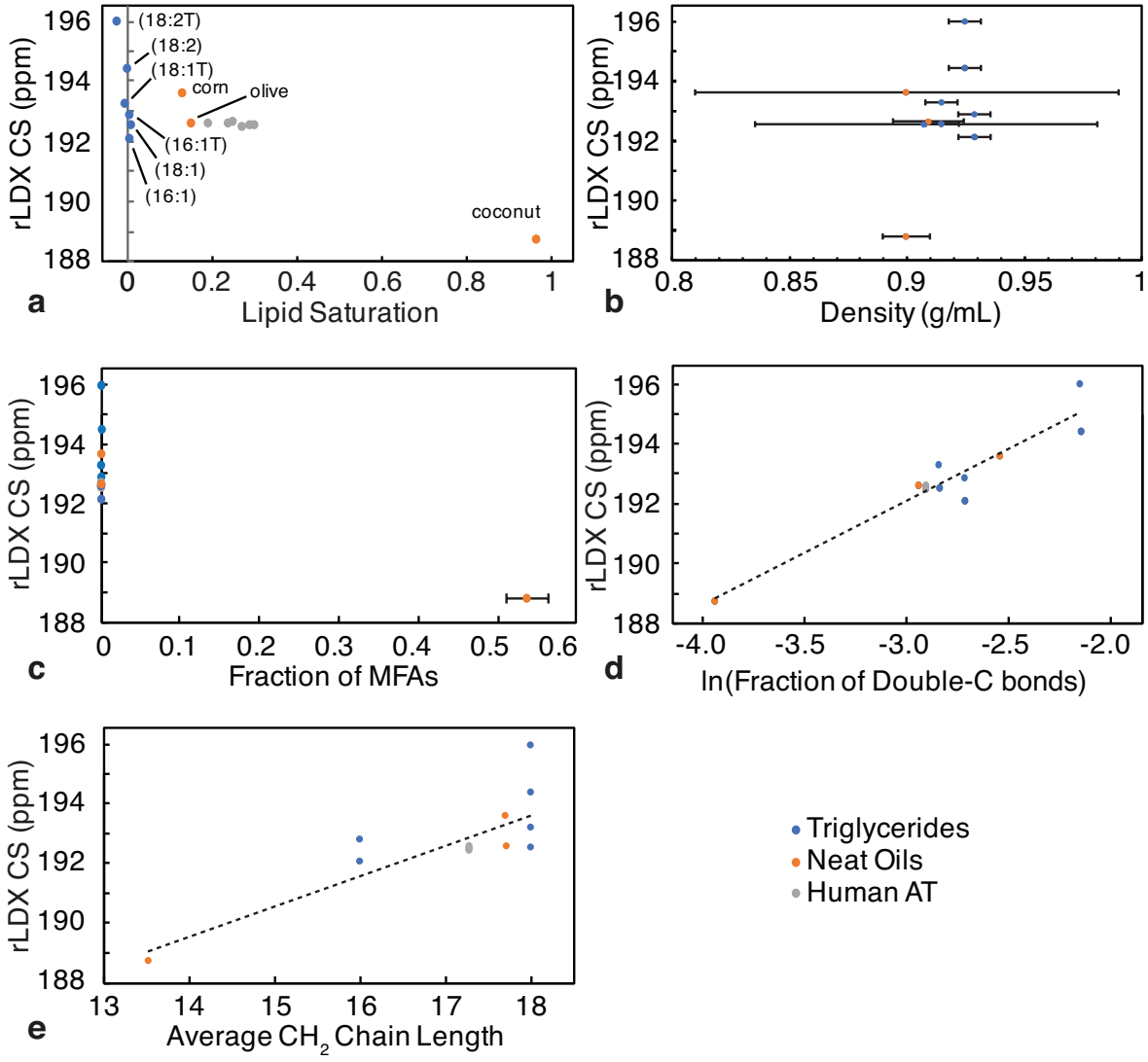

Figure 5.6: Plots of rLDX chemical shift at 37°C versus (a) lipid saturation, (b) density, (c) fraction of medium-chain fatty acids, (d) ln of the fraction of double-carbon bonds (FDCB), and (e) average hydrocarbon chain length (AHCL). FDCB and AHCL are calculated as described above. Fit lines for (d) and (e) are 3.470ln(FDCB)+202.48 ppm and 1.017(AHCL)+175.31 ppm, with R^2 values of 0.906 and 0.654, respectively. Error bars are omitted from (a) for clarity; values are given in Table 5.1.

and human AT[205], FDCB was calculated by

$$FDCB = \frac{\sum_i f_i D_i}{\sum_i f_i B_i}, \tag{5.8}$$

where f_i is the fraction of component i in the sample, D_i is the number of double carbon bonds in component i, and B_i is the total number of bonds in the hydrocarbon chain of component i. Similarly, AHCL was calculated by

$$AHCL = \frac{\sum_i f_i A_i}{\sum_i f_i} \tag{5.9}$$

where A_i is the number of the carbon atoms in the hydrocarbon chain, and the denominator serves as a normalization factor for the human AT composition, of which only 94% of the components were reported[205]. Surprisingly, neither density nor fraction of medium-chained fatty acids show a clear correlation with rLDX chemical shift. On the other hand, both FDCB and AHCL seem to correlate with rLDX chemical shift (Figure 5.6d,e). This dependence is not surprising and consistent with the dependence on the methylene/methyl ratio previously found by Lim, *et al*. [206] for the chemical shift of xenon dissolved in n-alkanes at constant temperature. This dependence, as later described by Yuan, *et al*. [82], does not arise from a higher contribution of CH_2 than CH_3 to the xenon chemical shift, but to the fact that these measurements were made at a constant temperature rather than at constant thermodynamic state[79, 82]. The observed increase in chemical shift with the number of double bonds is likely due to the through-space intermolecular deshielding effect of the carbon-carbon double bond. Of course, a double bond also produces a kink in the molecule and an increase in the"void size" sampled by xenon that, in turn, should lead to a decrease in xenon chemical shift. These two effects (increase in void size and increase in deshielding effect in the presence of a double bond) drive the xenon chemical shift in opposite directions. However, the increase in chemical shift due to the deshielding effect of a carbon-carbon double bond seems to be greater than the decrease in chemical shift due to the increase in void size, as shown by

comparison of chemical shift values obtained in *cis* and *trans* configurations of triglycerides. For example, as can be seen in Figure 5.4a, the difference in chemical shift is more remarkable between the triolein and trilinolein, which have comparable void sizes but a different number of carbon-carbon double bonds, than between the triolein and trielaidin, which have different void sizes but the same number of double bonds. Of course, to separate quantitatively each of these contributions to the xenon chemical shift, molecular dynamics simulations should be performed.

Despite the variation in rLDX chemical shift among the triglycerides and neat oil samples found here, the rLDX chemical shift seems to be consistent across all human AT samples, reflecting the similar composition and saturation of human AT at the molecular level[205]. Furthermore, even the rodent AT samples agree reasonably well with the human results, despite that the composition of rodent AT is expected to vary from that of humans, primarily because of differences in diet. Interestingly, this consistency is similar to the consistency found for the temperature dependence of T_1 and T_2 of methylene and methyl protons[207] in bovine fat, porcine fat, olive oil and mayonnaise, *highlighting the high similarity of these samples at the molecular level*. In light of these results, it is reasonable to assume that even if a larger number of human AT samples were to be analyzed, no significant differences in rLDX chemical shift would be observed. This suggests that the rLDX chemical shift can indeed be used to obtain absolute temperature information *in vivo* with a precision of 0.3°C when using the rLDX temperature calibration obtained here.

Of course, *in vivo*, a subject's motion and broadening of the resonance frequency lines could decrease temperature accuracy; however, local shimming procedures performed on the methylene protons, coupled with a sequential acquisition of the ^{1}H and ^{129}Xe spectra, can minimize these effects. On the other hand, any effect due to shimming conditions or tissue microscopic structure is completely eliminated by referencing the LDX frequency to that of the nearby methylene protons in which xenon dissolves. This opens up the opportunity to measure directly absolute temperature in adipose tissues like BAT, where the major dissolved-

phase peak observed during cold exposure after inhalation of a single bag of hyperpolarized xenon originates from xenon dissolved in the lipids of BAT[111].

Since the linear dependence of the rLDX chemical shift, which arises from the linear decrease of solvent density with increasing temperature, is expected to exist for a much wider temperature range[183], application of rLDX thermometry for temperature calibration of current proton MR thermometry methods in lipid-rich tumors could be envisioned. As demonstrated here, microscopic susceptibility gradients generated at water-fat interfaces often degrade the precision with which absolute temperature can be measured using methylene-referenced PRF. In these spectra, the water and methylene peaks were well-resolved and well-fit at each temperature, and the peak centroids were determined with negligible uncertainty. Even so, the ^{1}H-methylene chemical shift separation temperature calibrations previously reported led to an absolute temperature error up to 4°C. While specific applications may exist where a 4°C precision is acceptable, such as monitoring of tissue temperature during hyperthermia treatment of cancers, for others, such as the quantification of BAT thermogenesis in humans, a higher degree of precision is necessary.

5.6 Conclusion

In this work, we analyzed the dependence of the rLDX frequency on lipid saturation, FDCB, and AHCL for different oil and human AT samples. Although the rLDX frequency seems to depend on both FDCB and AHCL, the small variation in FDCB and AHCL that exists across human AT samples does not significantly affect the rLDX chemical shift. By using the rLDX temperature calibration found in these studies, absolute human AT temperature can, under optimal conditions, be obtained directly from the rLDX frequency with a precision of 0.3°C. On the other hand, in similar samples, the proposed ^{1}H-methylene temperature calibrations seem to produce temperature errors of several degrees Celsius.

CHAPTER 6: MAGNETIC RESONANCE THERMOMETRY WITH HYPERPOLARIZED XENON REVEALS NOVEL THERMOGENESIS MECHANISMS

6.1 Introduction

One of the most interesting applications of dissolved-phase ^{129}Xe MRI explored in our lab is the detection of the thermogenic function of a tissue called brown adipose tissue (BAT). The function of BAT is of great interest in the biomedical research community as this tissue is a potential target for the treatment of obesity and type 2 diabetes[208].

Brown adipose tissue is a tissue specialized in non-shivering thermogenesis, a mechanism developed by mammals to defend core body temperature. In BAT this mechanism is mediated primarily by uncoupling protein 1 (UCP1). Specifically, UCP1 uncouples fatty acid oxidation from adenosine triphosphate production, leading to a futile metabolic process that results in increased heat production[209]. As such, the presence of UCP1 in brown adipocytes has been thought of as a necessary, although not sufficient, condition for BAT thermogenesis[210, 211].

One critical tool for studying non-shivering thermogenesis in BAT has been the development of UCP1 knockout (KO) mice[212]. The KO animal model has enabled studies aimed at identifying UCP1-independent adaptive thermogenic mechanisms. Specifically, work done in isolated brown adipocytes of wild-type (WT) and KO mice have shown only a transient small response to norepinephrine in brown adipocytes of KO animals, leading to the conclusion that no other adrenergically-induced thermogenic mechanism exists in brown adipocytes except that mediated by UCP1[213, 214]. More recent studies have suggested that alternative mechanisms of thermogenesis that are independent of UCP1 may exist in beige fat[215–217], white adipose tissue[218], and/or skeletal muscle mitochondria[219]. The major drawback of these studies is that UCP1-independent thermogenesis was assessed, in all cases, indirectly,

by either measurements of oxygen consumption in a controlled environment, fat oxidation in tissue suspensions, and/or increased adenosine monophosphate-activated protein kinase activity in dissected tissues.

In vivo, the most widely used technique to detect BAT thermogenesis is ^{18}F-fluorodeoxyglucose positron emission tomography[114, 182, 220–228], which traces glucose uptake by stimulated BAT. However, as was recently demonstrated, glucose uptake in BAT can occur with or without BAT thermogenesis[220, 223]. At the same time, absence of glucose uptake in BAT does not exclude the presence of BAT thermogenesis[221, 227].

The most direct way to determine whether UCP1-independent thermogenic mechanisms exist in BAT would be via direct measurements of the temperature of this tissue in intact KO animals. However, temperature measurements of tissues deep inside the body are notoriously very difficult. Optical techniques like near-infrared thermography[223, 229] have the advantage of being minimally invasive and cost-effective for large studies; however, these measurements assess BAT temperature only indirectly via superficial skin temperature measurements that do not have the necessary sensitivity and specificity to detect small temperature changes that may occur a few mm beneath the skin[230–234]. Furthermore, thermographic techniques are prone to artifacts from the environmental conditions under which these measurements are performed, even when a reference region is used for relative temperature measurements[235]. Wire thermistors[210] and thermocouples[216, 236] have also been used. While the use of these probes is relatively straightforward and enables good temporal resolution, improper probe placement and the relatively large heat capacity of these probes may prevent the detection of small, but important, tissue temperature changes that could occur in the intact tissue[237].

As discussed in Chapter 5, dissolved-phase ^{129}Xe thermometry can serve as a robust and accurate absolute temperature probe in lipid-rich tissues. By referencing the temperature-dependent chemical shift of lipid-dissolved xenon to the temperature-independent chemical shift of nearby lipid protons, frequency shifts induced by macro- and microscopic suscepti-

bility gradients can be fully removed to obtain absolute temperature information[238, 239]. Additionally, our group has demonstrated that xenon accumulates specifically in BAT during stimulation of thermogenesis, enabling direct observation of differences in BAT thermogenic activity between lean and obese mice[109]. Therefore, in this final chapter, absolute MR thermometry by lipid-dissolved, hyperpolarized ^{129}Xe (XeMRT) is used to measure directly BAT temperature *in vivo* in both WT and KO mice to assess whether other UCP1-independent thermogenic mechanisms also exist in BAT.

6.2 Materials and Methods

6.2.1 Animal Protocol

All experiments were conducted under protocols approved by the Institutional Animal Care and Use Committee at the University of North Carolina at Chapel Hill. A colony of UCP1 wild-type (WT) mice and UCP1 knockout (KO) mice was generated from a single breeding pair of UCP1 heterozygous mice purchased from Jackson Laboratory with a C57BL genetic background. Mice were housed at thermoneutral conditions (24°C) and fed a standard chow diet *ad libitum* until imaging. Mice were genotyped by polymerase chain reaction of mouse tail DNA.

For the MR temperature experiment, a total of 3 WT mice and 8 KO mice were used. For these studies, each mouse was anesthetized with an intraperitoneal injection of pentobarbital (Oak Pharmaceuticals, Lake Forest, Illinois, USA) at 75 mg/kg followed by intubation. An intraperitoneal catheter was placed to provide maintenance doses of pentobarbital (1/4 of the initial dose every 40 minutes), while a subcutaneous catheter was placed for norepinephrine injection (Levophed norepinephrine bitartrate, Hospira, Inc., Lake Forest, Illinois, USA) at a dose of 1 mg/kg. A sketch of the experimental setup is shown in Figure 6.1.

All imaging experiments were performed on a 9.4 T spectrometer (Bruker BioSpec 94/30, Bruker Biospin Corp., Billerica, Massachusetts, USA). For the experiment, anesthetized mice

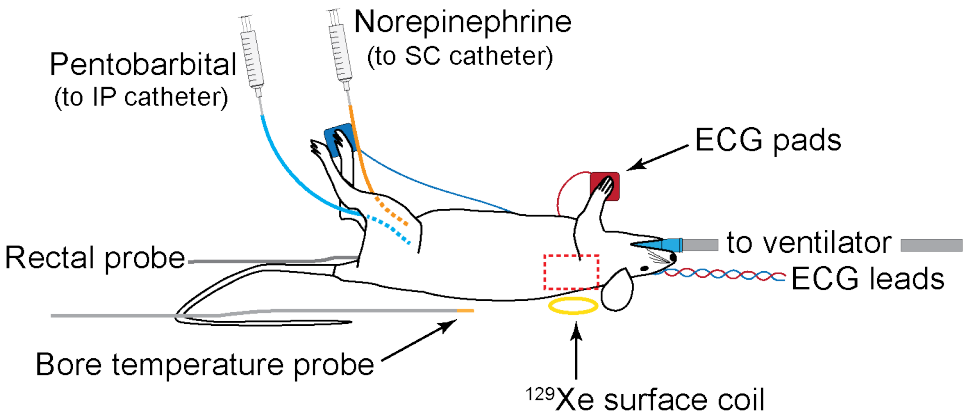

Figure 6.1: Following anesthesia, mice were placed on a small animal cradle with physiological monitoring by ECG and rectal probe, and were mechanically ventilated. A second temperature probe was placed next to the animal to monitor bore temperature. Pentobarbital and norepinephrine injections were administered *in situ* via intraperitoneal (IP) and subcutaneous (SC) catheters, respectively, attached to lines running out of the magnet bore to syringes. The red dashed line indicates the anatomical region of interest which also coincides with the sensitive region of the ^{129}Xe surface coil.

were placed supine on a 1 cm diameter ^{129}Xe surface coil (m2m Imaging Corp., Cleveland, Ohio, USA) with the sensitive region of the coil located above the interscapular BAT depot. The ^{129}Xe surface coil was then placed inside a 72 mm ^{1}H quadrature volume coil (Bruker Biospin Corp.), used to collect ^{1}H anatomical images and spectra, and positioned at the isocenter of the 9.4 T magnet. One animal was scanned with a 35 mm dual-tuned ^{1}H/^{129}Xe volume quadrature coil (m2m Imaging Corp.) used to acquire all spectra.

During the experiment, mice were mechanically ventilated using a homemade ventilator similar to one described in previous work[147] compatible with hyperpolarized ^{129}Xe gas at a tidal volume of 0.15 mL with 30-vol% O_2 and 70-vol% N_2. For ^{129}Xe measurements the N_2 volume was replaced with ^{129}Xe gas polarized to around 16%. Throughout the experiment, mouse heart rate was monitored via ECG with an MR-compatible physiological monitoring system (Small Animal Instruments, Stony Brook, New York, USA).

The spectrometer bore temperature was monitored by an MR-compatible thermocouple and maintained at 34°C ± 1°C by a forced-air heating system (Small Animal Instruments).

Mouse rectal temperature was monitored via an MR-compatible rectal probe (Temp 9500, Oakton Instruments, Vernon Hills, Illinois, USA). Once in place, anesthetized mice were equilibrated to bore temperature for about 30 minutes while anatomical images were acquired and a BAT volume of interest shimmed for field homogeneity as described below. Mouse rectal temperature after 30 minutes consistently stabilized around 34.5°C. Once equilibrated, periodic BAT and rectal temperature measurements were made using XeMRT and the rectal temperature probe, respectively. After the acquisition of 2-3 xenon spectra and rectal temperature data points, mice were injected with norepinephrine at a dose of 1 mg/kg. After norepinephrine injection, a series of XeMRT temperature measurements were performed every 3-10 minutes for the entire duration of BAT stimulation, which lasted up to about 40-50 minutes after subcutaneous norepinephrine injection. In some animals, a second norepinephrine injection was performed about one hour from the first injection. At the end of the experiment, mice were euthanized with an overdose of pentobarbital.

6.2.2 *In Vivo* ^{129}Xe Magnetic Resonance Thermometry

All MR scans were respiratory triggered to reduce motion artifacts. Anatomical axial ^{1}H scans were acquired with a multi-slice, multi-echo imaging sequence using a 30×30 mm^2 field of view, 256×128 matrix, 6 slices, 2 mm slice thickness, 20 ms echo time, 1 s repetition time, and 1 average. Volumes of interest containing primarily interscapular BAT were identified in the anatomical images and the signal selected from a localized point-resolved spectroscopy sequence (PRESS) was manually shimmed up to the second order using the ^{1}H methylene peak. The localized ^{1}H spectra were acquired immediately before and after the acquisition of ^{129}Xe spectra with 2048 complex points, 20 ppm bandwidth, 12 averages, 2 s repetition time, 18.2 ms echo time, and 400.321 MHz basic frequency. ^{129}Xe spectra were acquired either with a non-localized sequence (90°-acquisition sequence, with 4096 complex points, 500 ppm bandwidth, 110.7518 MHz basic frequency, 4 s repetition time, and 15 averages) or a localized stimulated echo acquisition mode sequence (STEAM, 4096 complex points, 500

ppm bandwidth, 110.7518 MHz basic frequency, 6 ms echo time, 7 ms mixing time, 3.5 s repetition time, and 20 averages). From each pair of ^{1}H and ^{129}Xe spectra, BAT absolute temperature T was calculated by using the previously determined temperature calibration for the chemical shift of lipid-dissolved ^{129}Xe [239]:

$$T = \frac{\delta_{CH_2,ref} - (200.15 \pm 0.03)ppm}{-(0.0058 \pm 0.0010)ppm/^{\circ}C}, \tag{6.1}$$

where $\delta_{CH_2,ref}$ is the methylene-referenced, lipid-dissolved ^{129}Xe chemical shift. This shift is calculated with respect to a fictitious 0 ppm reference derived from the ^{1}H spectra as detailed in Chapter 4.

In regions of strong magnetic susceptibility gradients, such as BAT, ill-defined peak shapes can result from the convolution of macro- and microscopic magnetic susceptibility and shimming gradients. As a result, typical post-processing procedures such as phasing, baseline correction, and peak-fitting of standard spectroscopic line shapes (*e.g.* Lorentzian, Lorentzian/Gaussian, Voigt) fail to estimate reliably the peak centroid and uncertainty. Therefore, two independent analyses were performed whereby ^{1}H and ^{129}Xe peak centroids were manually determined by two independent investigators from magnitude spectra. The average of the two peak centroids was then used to calculate the temperature, and half of the difference between the two values was used as the uncertainty.

6.2.3 Xenon-enhanced Computed Tomography

Xenon-enhanced computed tomography was used as described in previous studies[114] to directly assess the degree of xenon uptake in the activated BAT of both WT and KO phenotypes. For these experiments six animals, three WT mice and three KO mice, were anesthetized and intubated as described above and placed in the CT scanner (GE eXplore speCTZ/CT, General Electric Company, Waukesha, Wisconsin, USA). Animals were then injected with a 1 mg/kg dose of norepinephrine and ventilated with a tidal volume of 0.25 mL with 30-vol% O_2 and 70-vol% N_2 during non-enhanced CT scans. Scout CT scans were

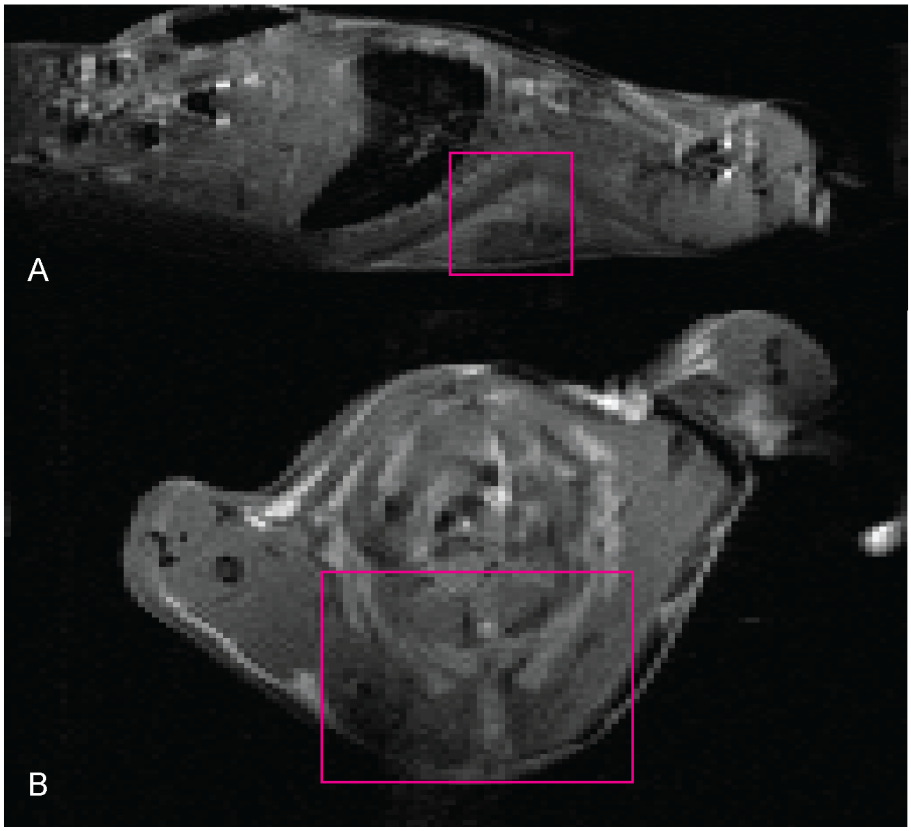

Figure 6.2: Anatomical ^{1}H images showing the shimmed region from which localized spectra were acquired. Representative sagittal (a) and axial (b) images of one KO mouse with the localized spectroscopy voxel outlined in magenta. The ^{129}Xe surface coil was located right beneath this region.

initiated immediately after norepinephrine injection, followed by non-enhanced and then xenon-enhanced CT scans. All CT scans were acquired with a tube peak voltage of 70 kVp, current of 50 mA, 220 views, and a resolution of 100 μm. Analysis of CT images was performed using VivoQuant software (Invicro, LLC, Boston, Massachusetts, USA).

6.3 Results

An example of anatomical ^{1}H images indicating the shimmed region from which localized spectra were acquired is shown in Figure 6.2. The interscapular BAT is clearly visible in these images as regions of hyperintensity centered within the volume of interest. A large volume ($\sim$ 4 cm^3) was selected to include the entire interscapular BAT depot that mostly

contributed to the observed ^{129}Xe signal detected with the surface coil located beneath the BAT depot. Examples of ^{1}H and ^{129}Xe spectra acquired from a KO animal are shown in Figure 6.3. Prior to norepinephrine injection, non-localized ^{129}Xe spectra contain broad signal components originating from non-fat tissues located primarily outside the shimmed area, whereas in localized xenon spectra most of the signal originates from fat-containing tissues that possibly include both BAT and surrounding white adipose tissue. As expected, given the short repetition times used in these sequences, in both spectra the intensity of the lipid-dissolved ^{129}Xe is too small to be quantified, preventing measurement of BAT temperature before stimulation. Right after stimulation of thermogenesis, an average 30-fold enhancement in the lipid-dissolved ^{129}Xe peak in the non-localized sequence enabled clear identification of the lipid-dissolved ^{129}Xe peak from BAT and measurement of its frequency.

Given the broad contribution of nearby ^{129}Xe peaks in the non-localized spectra at the lipid-dissolved xenon frequency, the 30-fold enhancement is clearly an underestimation of the actual signal enhancement that occurs as a result of the increased uptake of ^{129}Xe in BAT. The relative signal enhancement in the localized ^{129}Xe spectra more closely reflects the actual specific enhancement in xenon uptake in BAT; however, since the localized lipid-dissolved ^{129}Xe signal from BAT is not clearly visible pre-norepinephrine injection, the specific enhancement in BAT cannot be directly quantified. On the other hand, no significant differences were noted in the localized ^{1}H spectra.

While ^{129}Xe spectroscopy clearly indicates that the major xenon signal originates from lipid compartments, xenon-enhanced computed tomography (XECT) confirmed that these lipid compartments are lipid compartments in BAT. A selective radio density enhancement of over 200 Hounsfield units (HU) was observed in the BAT of KO mice, similar to the enhancement observed in WT mice (Figure 6.4) reported in previous work[114]. Thus, XECT confirmed negligible radio density enhancement from nearby muscle tissue or white adipose tissue, confirming that the lipid-dissolved xenon signal observed in ^{129}Xe spectra after norepinephrine stimulation derives from BAT.

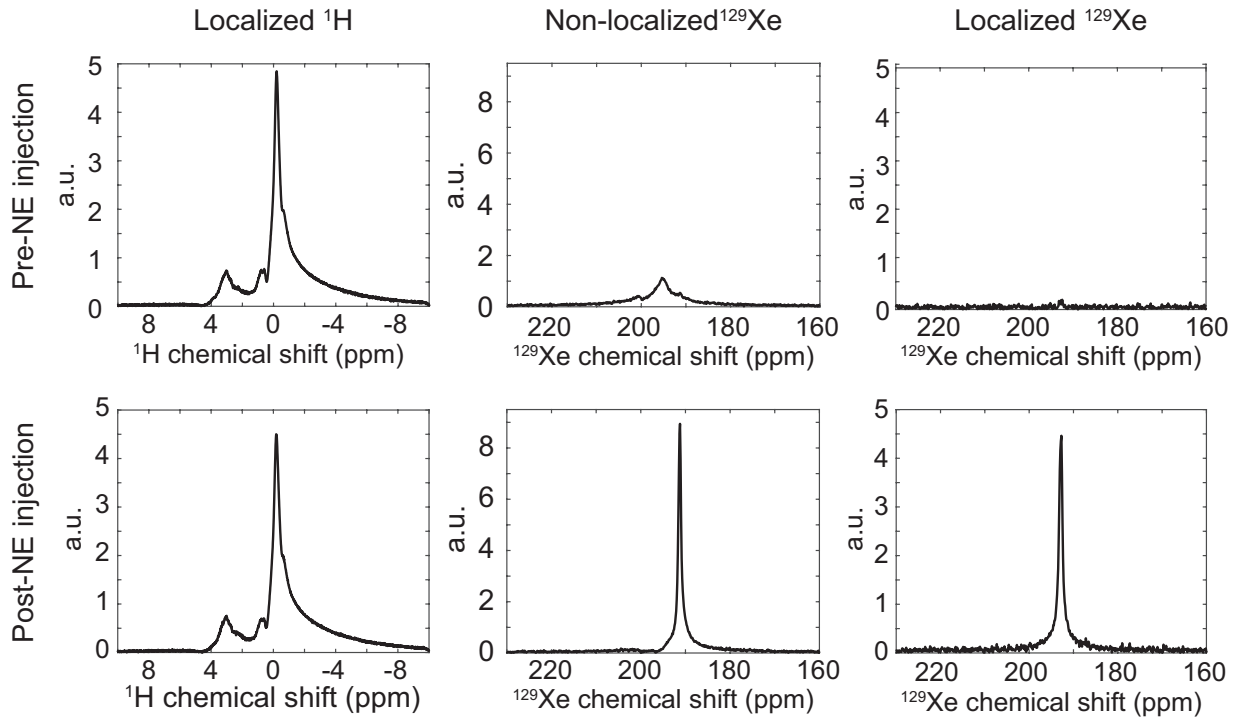

Figure 6.3: ^{1}H and ^{129}Xe spectra from a KO animal before and after norepinephrine injection. No changes are observed in the localized ^{1}H spectra before and after norepinephrine injection, whereas a large signal enhancement is observed in localized and non-localized ^{129}Xe spectra right after norepinephrine injection as a result of BAT activation and the shunting of blood to this tissue[114]. Unlike the non-localized xenon spectra, that before norepinephrine injection shows mainly broad signal components originating from non-fat regions outside the shimmed voxel, the localized ^{129}Xe spectra show only a very small signal component originating from lipid compartments before norepinephrine injection. In the xenon spectra, before norepinephrine, non-localized ^{129}Xe spectra showed contributions from regions outside of the BAT whereas localized ^{129}Xe spectra showed little or no signal in the BAT above noise. The ^{129}Xe chemical shifts are referenced to the spectrometer center frequency and the ^{129}Xe spectra are referenced to the methylene signal, as described in Chapters 4 and 5.

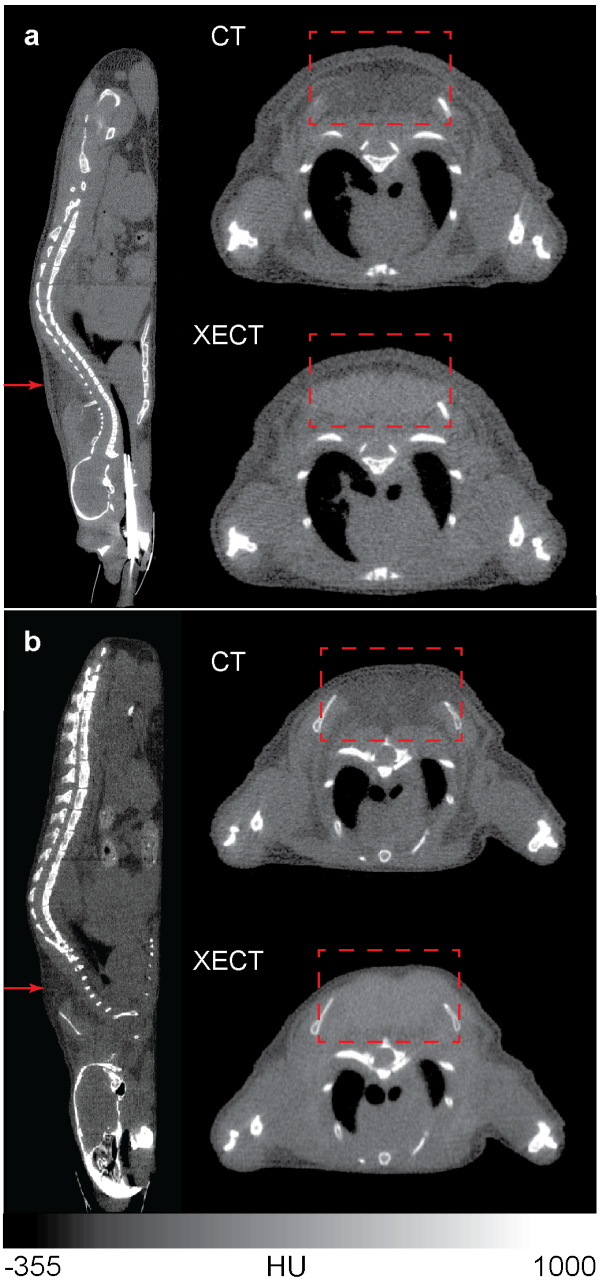

Figure 6.4: Non-enhanced and xenon-enhanced CT images of a WT and a KO mouse. **a:** Axial CT and xenon-enhanced CT (XECT) images of a WT mouse after norepinephrine injection, with a non-enhanced sagittal CT image indicating the location of the axial slice (red arrow). **b:** Axial CT and XECT images of a KO mouse after norepinephrine injection, with a non-enhanced sagittal CT image indicating the position of the axial slice (red arrow). In both WT and KO mice ventilation with xenon during norepinephrine stimulation resulted in a >200 HU enhancement in interscapular BAT (red dashed box).

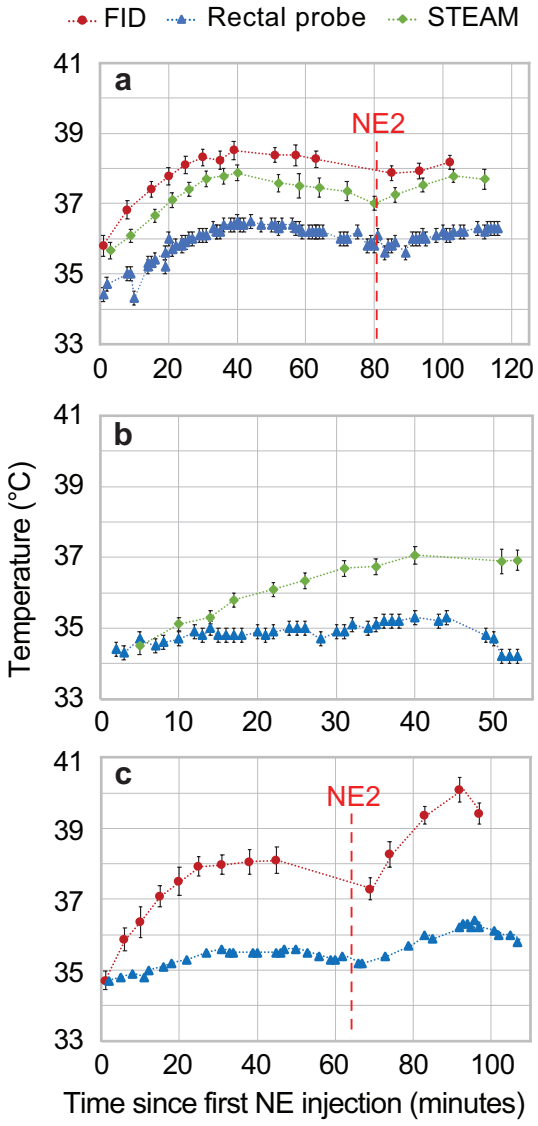

Figure 6.5: Temperature trends following the first norepinephrine injection for two KO mice and one WT mouse. Plots of rectal temperature (blue triangles) as well as BAT temperature as measured by XeMRT using a non-localized (red circles) and/or localized (green diamonds) ^{129}Xe sequence versus time following the first norepinephrine injection. Second norepinephrine injection times are indicated by the red dashed line and label "NE2". Animals (a) and (b) are KO mice and (c) is a WT mouse.

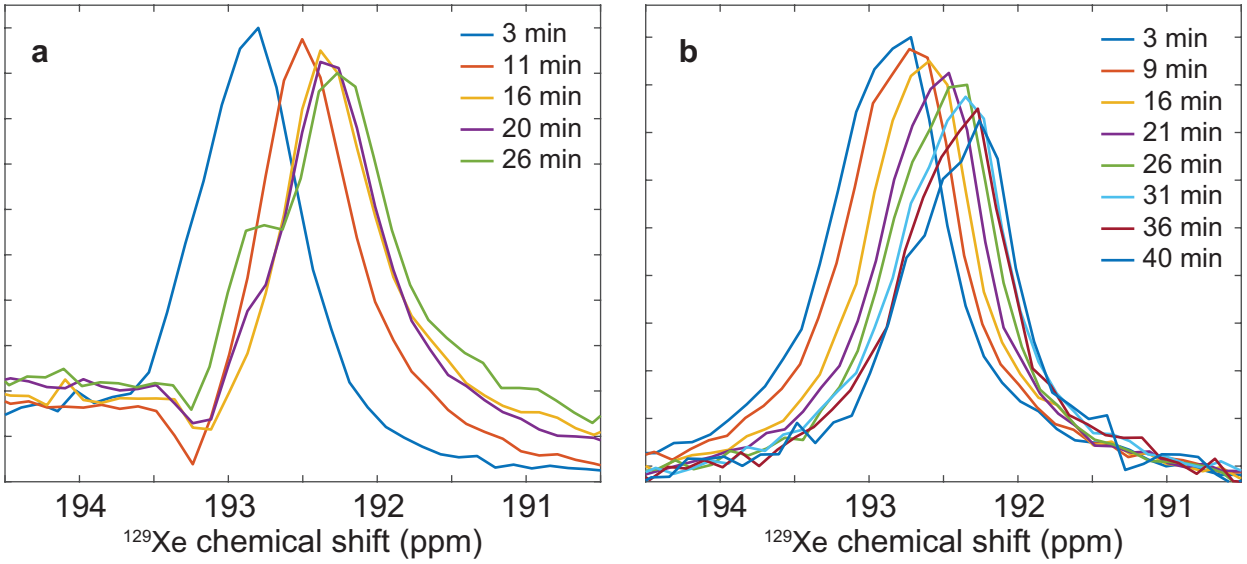

Figure 6.6: Example of lipid-dissolved ^{129}Xe spectra acquired in WT and KO mice following norepinephrine injection. Plots of lipid-dissolved ^{129}Xe spectra over time in (a) WT (non-localized) and (b) KO (localized) mice show the clear upfield shift of the lipid-dissolved ^{129}Xe chemical shift, indicating a clear increase in lipid temperature. Spectrum amplitudes are scaled for clarity.

An example of BAT temperature measurements obtained from KO and WT animals right after stimulation of thermogenesis by norepinephrine, when the lipid-dissolved ^{129}Xe frequency can be clearly identified and measured, is shown in Figure 6.5. An increase in BAT temperature following norepinephrine injection was observed in both KO and WT mouse phenotypes, regardless of gender. Figure 6.6 shows the remarkable temperature-induced drift of the lipid-dissolved ^{129}Xe peak used to measure BAT temperature changes. In both phenotypes BAT temperature increases steadily after norepinephrine injection for about 40-50 minutes, after which BAT stimulation ceases and the lipid-dissolved ^{129}Xe signal intensity returns to baseline levels, preventing further temperature measurements. Although the increase in BAT temperatures in WT mice was generally greater than in KO mice, in both phenotypes the increase in BAT temperature was higher than the increase in rectal temperature, suggesting that heat was generated in or near BAT. The KO animals that received a second norepinephrine injection after BAT activity ceased presented a further

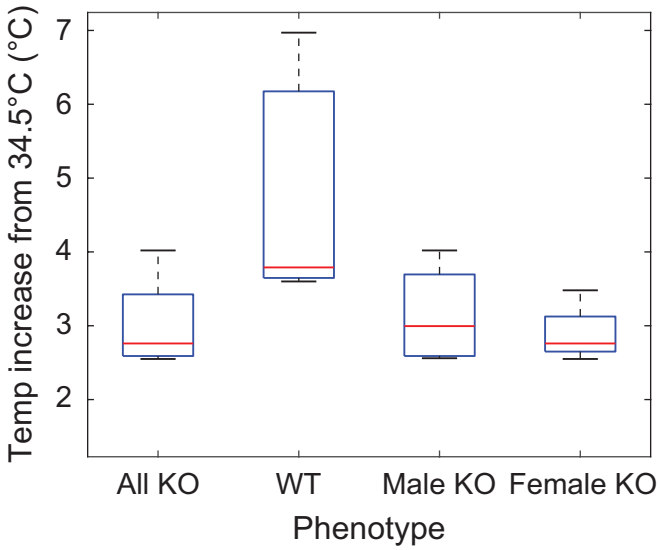

Figure 6.7: Box plots of maximum temperature increases above 34.5°C for all animals as measured by XeMRT following norepinephrine injection. The mean ± standard deviation for each group of animals is as follows: (3.0 ± 0.5)°C for all N=8 KO animals, (4.9 ± 1.9)°C for N=3 WT animals, (3.1 ± 0.7)°C for N=4 male KO animals, and (2.9 ± 0.4)°C for N=4 female KO animals.

increase in BAT temperature. A summary of the maximum temperature increase observed in WT and KO mice is provided in the box plot in Figure 6.7.

6.4 Discussion and Conclusion

In this study, we present evidence that the BAT of KO mice is thermogenically competent. Temperature measurements by XeMRT show that BAT temperature increases with norepinephrine stimulation, despite ablation of UCP1 (Figure 6.7). This result lends credence to other investigations that have suggested the possible existence of thermogenic mechanisms independent of UCP1[215–218, 221]. Specifically, in almost every KO mouse, the rate at which BAT temperature increases is faster than the rectal temperature. The same trends are observed in the WT mice, but are much more pronounced because of the presence and action of UCP1 in the BAT of these animals (Figure 6.5). This strongly suggests that some form of non-shivering thermogenesis, independent of UCP1, also takes place in or very near the BAT of KO mice.

Recent studies have also presented evidence for three possible UCP1-independent thermogenic mechanisms in brown adipocytes[211]: genetic evidence for creatine-regulated substrate cycling[215, 240]; genetic, physiological monitoring, and a series of *in vitro* assay evidence for calcium-dependent hydrolysis of adenosine triphosphate[216]; and core body temperature data for proton leak by uncoupling protein 3[241]. However, in each of the studies above, support for the existence of the given UCP1-independent thermogenic mechanism is limited to indirect evidence. *The current study, on the other hand, represents the first direct observation of UCP1-independent non-shivering thermogenesis in BAT* in vivo. It is important to note that this method reports directly on the temperature of brown adipocytes. These and other[114] experiments have clearly shown that, following norepinephrine injection, the lipid-dissolved signal observed in ^{129}Xe spectra originates exclusively from fat droplets contained within brown adipocytes. As such, these temperature measurements report directly on BAT cell temperature, which is expected to be higher than overall tissue temperature. Other MR-based techniques typically measure the average temperature in a given region of interest, which may contain other tissues and give rise to partial volume effects.

The thermometry technique used here can also provide absolute temperature measurements. It is important to note that, for accurate absolute temperature measurement in mice, where the sensitive region of small surface coils is still relatively large compare to the area of interest, localized spectroscopy sequences should be used. Prior to norepinephrine injection, other broad, dissolved-phase ^{129}Xe signals are indeed clearly visible in the non-localized spectrum, as shown in Figure 6.3. These peaks most likely originate from ^{129}Xe dissolved in blood plasma and in the lung parenchyma[128], which are anatomically close to the volume of interest and within the ^{129}Xe surface coil sensitive region. The localized ^{129}Xe spectra, on the other hand, do not contain contamination from anatomical regions outside of the volume of interest because of dephasing by the imaging gradients as well as mixing times that are much longer than the effective transverse relaxation time ($T_2^\star$) of these signals. In this study, absolute temperature measurements by the non-localized ^{129}Xe sequence suffer from

a systematic error that most likely results from: (1) signal contamination from other BAT regions outside of the volume of interest; and (2) a slight mismatch between the sensitive region of the ^{129}Xe surface coil and the shimmed region of the interscapular BAT. When large surface coils (relative to the region of interest) are used, as in this case, a localized spectroscopy sequence should be used to obtain a more reliable absolute temperature measurement. Nonetheless, the relative temperature changes measured using the non-localized spectroscopy sequence still reliably reveal the surprising increase in BAT temperature in KO animals following norepinephrine injection.

In summary, we have used XeMRT to observe norepinephrine-induced UCP1-independent non-shivering thermogenesis in mice.

CHAPTER 7: CONCLUSIONS

This dissertation described work that began with studies of ^{129}Xe depolarization mechanisms in continuous-flow spin-exchange optical pumping and proceeded through the development of a simple and robust ^{1}H referencing system for dissolved-phase ^{129}Xe magnetic resonance spectroscopy. The use of a ^{1}H reference for dissolved-phase ^{129}Xe frequencies enabled the identification of new dissolved-phase signals *in vivo* as well as the use of ^{129}Xe as an absolute temperature probe in adipose tissue. This final chapter reviews the major results presented and contributions to the field of ^{129}Xe magnetic resonance spectroscopy.

Chapter 2 described in detail the design and construction of both an ultra-low field NMR spectrometer and an optical spectrometer for use in studying continuous-flow SEOP. The ultra-low field NMR spectrometer is based on an in-house LabVIEW-controlled spectrometer that enables full customization of the NMR acquisition. In addition to monitoring ^{129}Xe polarization *in situ* in the polarizer optical cell, the spectrometer also incorporates an external trigger that can interface with our small animal ventilator and enables future *in vitro* and *in vivo* hyperpolarized ^{129}Xe studies. The optical spectrometer, similarly, was built to have a flexible resolution and bandwidth needed for atomic absorption spectroscopy measurements during continuous-flow SEOP.

The ultra-low field NMR and optical spectrometers were then used in Chapter 3 to study the effects of depolarization by dark Rb and to attempt to observe evidence of Rb nanoclusters during continuous-flow SEOP. While the optical absorption spectroscopy measurements were not sensitive enough to directly observe Rb_2 *in situ*, absorption measurements on a sealed Rb cell allowed us to set an upper limit of 8.3×10^{15} cm^{-3} for Rb_2 present during continuous-flow SEOP. In addition, we found that ^{129}Xe depolarization caused by dark Rb vapor in the outlet of the optical cell was not more than a few percent for typical collection parameters, but

could have more detrimental effects on final ^{129}Xe polarization at higher temperatures and lower flow rates.

Chapter 4 began by describing some of the *in vivo* applications of hyperpolarized ^{129}Xe gas and points to one of the major issues encountered in *in vivo* NMR spectroscopy experiments with hyperpolarized ^{129}Xe: the lack of a robust spectroscopic reference. We first examined the effects of magnetic susceptibility gradients on the traditional gas-phase referencing technique for ^{129}Xe MRS measurements. We showed that magnetic susceptibility gradients produce an apparent shift of dissolved-phase frequencies up to 3 ppm when the gas phase is used as a reference. This shift could be even higher when specific shimming conditions are used. We then proposed the use of the ^{1}H frequency as a spectroscopic reference standard for the dissolved-phase ^{129}Xe frequencies. This ^{1}H-based reference enabled direct comparison of *in vitro* high resolution ^{129}Xe spectra with *in vivo* dissolved-phase spectra to identify at least one new dissolved-phase peak in the rat head and to clarify two other peak assignments.

Chapter 5 investigated the dependence of the methylene-referenced ^{129}Xe signal on lipid composition and temperature, characterizing the temperature dependence of the lipid-dissolved ^{129}Xe chemical shift in human adipose tissue (δ=(-0.2058±0.0010 ppm/°C)×T +(200.15±0.03 ppm)). We showed that, while the ^{129}Xe chemical shift did depend strongly on triglyceride hydrocarbon chain length and the number of double carbon bonds, the natural variations in lipid composition between human samples did not significantly affect the absolute temperature calibration. The absolute temperature dependence of ^{129}Xe in rodent adipose tissue also agreed reasonably well with that in humans, enabling the use of the same temperature calibration for these species.

Finally, absolute ^{129}Xe MR thermometry was used in Chapter 6 to study brown adipose tissue activity in wild-type and UCP1 knockout mice genetically modified to be, presumably, incapable of generating heat in their brown adipose tissue. Surprisingly, by using hyperpolarized ^{129}Xe thermometry we were able to detect thermogenic activity in the brown adipose tissue of these mice. Following norepinephrine stimulation, UCP1 knockout mice

presented an average increase in brown adipose tissue temperature above equilibrium of (3.0±0.5)°C by ^{129}Xe MR thermometry. These temperature measurements demonstrate that ^{129}Xe MR thermometry is both sensitive to small temperature changes and robust against microscopic susceptibility gradients that can severely limit the accuracy of other MR thermometry methods.

As described in this dissertation, magnetic resonance spectroscopy based on dissolved-phase xenon NMR resonances shows great promise to become a powerful research tool to probe the molecular environment of tissues and organs. A number of avenues that build on the present work are currently being pursued in our group. These include the use of ^{129}Xe magnetic resonance thermometry to assess BAT thermogenic function in adult humans. This application is particularly exciting as current imaging modalities like ^{18}F-FDG-PET, ^{1}H-based MR thermometry, and infrared thermography are unable to reliably detect BAT thermogenesis in adult humans. The ability to directly monitor BAT thermogenesis in humans can provide new insights into the role that this tissue plays in the development of obesity and diabetes, as well as provide a more specific tool to assess the efficacy of anti-obesity therapies that directly target BAT function.

While our current polarization efficiency is fairly adequate for BAT thermometry in adult humans, for quantification of BAT mass, higher polarization levels, close to the theoretical maximum, would be needed. The ability to quantify BAT mass is of clinical relevance since the extent of BAT mass is determined by chronic BAT activity. Currently, 2D hyperpolarized ^{129}Xe MRI maps of BAT mass with an in-plane spatial resolution of 14 × 14 mm^2 can be obtained with a xenon polarization of only about 16%. Because resolution in MR images is not "diffraction limited" but "SNR limited", a four-fold increase in polarization would lead directly to a four-fold increase in resolution. Such an increase in polarization levels have been reported in the literature [242] and should be possible with the newer polarizer currently under construction in our lab.

Another promising future application of dissolved-phase hyperpolarized ^{129}Xe is as a contrast agent for molecular imaging. A number of biosensors used in combination with hyperpolarized ^{129}Xe have been demonstrated in the literature, but await full translation to *in vivo* applications. For example, the cage molecule cucurbit[6]uril can contain a single ^{129}Xe atom acquired from a surrounding pool of dissolved-phase ^{129}Xe. The chemical exchange of ^{129}Xe between the dissolved phase and the molecule, coupled with the large chemical shift difference between these two compartments, allows for a novel source of contrast that enables imaging of μM concentrations of the cage molecule. This technique is known as hyperpolarized ^{129}Xe chemical exchange saturation transfer (hyper-CEST). Furthermore, cage molecules like cucurbit[6]uril can be decorated with ligands that target specific chemical environments or cell receptors. One could then envision using such a molecule to target, for example, a particular type of cancer cell for imaging and treatment. More recently, nanoscale gas vesicles have been developed and used in conjunction with hyper-CEST. The major advantage of gas vesicles over cage molecules is that a single gas vesicle is able to host many ^{129}Xe atoms, thus leading to a further boost in MR sensitivity down to nM concentrations[243]. While these applications are still in the early stages of development, with the continued improvement of ^{129}Xe polarization efficiency and dissolved-phase ^{129}Xe MR methods, the full capability of these biosensors for molecular imaging could be realized in the near future.

REFERENCES

[1] Bloch F. Nuclear Induction. *Physical Review* 1946; 70:460–474.

[2] Purcell E, Torrey H, Pound R. Resonance Absorption by Nuclear Magnetic Moments in a Solid. *Physical Review* 1946; 69:37–38.

[3] Wuthrich K, "NMR of Proteins and Nuclei Acids". Wiley, New York, 1986.

[4] Lauterbur PC. Image Formation by Induced Local Interactions: Examples Employing Nuclear Magnetic Resonance. *Nature* 1973; 242:190–191.

[5] Damadian R. Tumor Detection by Nuclear Magnetic Resonance. *Science* 1971; 171:1151–1153.

[6] Mansfield P, Maudsley AA. Medical imaging by NMR. *British Journal of Radiology* 1977; 50:188–194.

[7] Fan I, KnappeGrüneberg S, Voigt J, Kilian W, Burghoff M, Stollfuss D, Schnabel A, Wübbeler G, Bodner O, Elster C, Seifert F, Trahms L. Direct measurement of the γHe/γXe ratio at ultralow magnetic field. *Journal of Physics: Conference Series* 2016; 723:012045.

[8] Levitt MH, "Spin Dynamics". John Wiley & Sons, Ltd, Chichester, UK, 2nd ed., 2008.

[9] Hoult D, Richards R. The signal-to-noise ratio of the nuclear magnetic resonance experiment. *Journal of Magnetic Resonance* 1976; 24:71–85.

[10] Haacke EM, Brown RW, Thompson MR, Venkatesan R, "Magnetic Resonance Imaging: Physical Principles and Sequence Design". John Wiley & Sons Ltd, 2nd ed., 2014.

[11] Wong GP, Tseng CH, Pomeroy VR, Mair RW, Hinton DP, Hoffmann D, Stoner RE, Hersman FW, Cory DG, Walsworth RL. A system for low field imaging of laser-polarized noble gas. *Journal of magnetic resonance (San Diego, Calif. : 1997)* 1999; 141:217–227.

[12] Bloembergen N, Purcell EM, Pound RV. Relaxation Effects in Nuclear Magnetic Resonance Absorption. *Physical Review* 1948; 73:679–712.

[13] Hahn EL. Spin Echoes. *Physical Review* 1950; 80:580–594.

[14] Hennig J. Echoes: how to generate, recognize, use or avoid them in MR-imaging sequences. Part I: Fundamental and not so fundamental properties of spin echoes. *Concepts in Magnetic Resonance* 1991; 3:179–192.

[15] Happer W. Optical Pumping. *Reviews of Modern Physics* 1972; 44:169–249.

[16] Walker TG, Happer W. Spin-exchange optical pumping of noble-gas nuclei. *Reviews of Modern Physics* 1997; 69:629–642.

[17] Appelt S, Baranga A, Erickson C, Romalis M, Young A, Happer W. Theory of spin-exchange optical pumping of 3He and 129Xe. *Physical Review A* 1998; 58:1412–1439.

[18] Wagshul M, Chupp TE. Optical Pumping of high-density Rb with a broadband dye laser and GaAlAs diode laser arrays: Application to 3He polarization. *Physical Review A* 1989; 40:4447.

[19] Driehuys B, Cates GD, Miron E, Sauer K, Walter DK, Happer W. High-volume production of laser-polarized 129Xe. *Applied Physics Letters* 1996; 69:1668.

[20] Saha I, Nikolaou P, Whiting N, Goodson BM. Characterization of violet emission from Rb optical pumping cells used in laser-polarized xenon NMR experiments. *Chemical Physics Letters* 2006; 428:268–276.

[21] Rosenberry Ma, Reyes JP, Tupa D, Gay TJ. Radiation trapping in rubidium optical pumping at low buffer-gas pressures. *Physical Review A* 2007; 75:1–6.

[22] Leawoods JC, Yablonskiy DA, Saam B, Gierada DS, Conradi MS. Hyperpolarized 3He gas production and MR imaging of the lung. *Concepts in Magnetic Resonance* 2001; 13:277–293.

[23] Chann B, Babcock E, Anderson LW, Walker TG. Measurements of 3He spin-exchange rates. *Physical Review A* 2002; 66:032703.

[24] Fink A, Brunner E. Optimization of continuous flow pump cells used for the production of hyperpolarized 129Xe: A theoretical study. *Applied Physics B* 2007; 89:65–71.

[25] Hersman FW, Ruset IC, Ketel S, Muradian I, Covrig SD, Distelbrink J, Porter W, Watt D, Ketel J, Brackett J, Hope A, Patz S. Large Production System for Hyperpolarized 129Xe for Human Lung Imaging Studies. *Academic Radiology* 2008; 15:683–692.

[26] Schrank G, Ma Z, Schoeck A, Saam B. Characterization of a low-pressure high-capacity 129Xe flow-through polarizer. *Physical Review A* 2009; 80:063424.

[27] Ma ZL, Sorte EG, Saam B. Collisional 3He and 129Xe Frequency Shifts in Rb-Noble-Gas Mixtures. *Physical Review Letters* 2011; 193005:11–14.

[28] Nikolaou P, Coffey AM, Walkup LL, Gust BM, Whiting N, Newton H, Muradyan I, Dabaghyan M, Ranta K, Moroz GD, Rosen MS, Patz S, Barlow MJ, Chekmenev EY, Goodson BM. XeNA: An automated 'open-source' 129Xe hyperpolarizer for clinical use. *Magnetic Resonance Imaging* 2014; 32:541–550.

[29] Nikolaou P, Coffey AM, Walkup LL, Gust BM, LaPierre CD, Koehnemann E, Barlow MJ, Rosen MS, Goodson BM, Chekmenev EY. A 3D-Printed High Power Nuclear Spin Polarizer. *Journal of the American Chemical Society* 2014; 136:1636–1642.

[30] Norquay G, Collier GJ, Rao M, Stewart NJ, Wild JM. 129Xe-Rb Spin-Exchange Optical Pumping with High Photon Efficiency. *Physical Review Letters* 2018; 121:153201.

[31] Chann B, Babcock E, Anderson L, Walker T. Skew light propagation in optically thick optical pumping cells. *Physical Review A* 2002; 66:1–3.

[32] Ruset I, Tsai L, Mair R, Patz S, Hrovat M, Rosen M, Muradian I, Ng J, Topulos G, Butler J, Walsworth R, Hersman F. A system for open-access 3He human lung imaging at very low field. *Concepts in Magnetic Resonance Part B: Magnetic Resonance Engineering* 2006; 29B:210–221.

[33] Norquay G, Parnell SR, Xu X, ParraRobles J, Wild JM. Optimized production of hyperpolarized 129Xe at 2 bars for in vivo lung magnetic resonance imaging. *Journal of Applied Physics* 2013; 113.

[34] Freeman MS, Emami K, Driehuys B. Characterizing and modeling the efficiency limits in large-scale production of hyperpolarized 129Xe. *Physical Review A* 2014; 90:023406.

[35] Kuzma NN, Patton B, Raman K, Happer W. Fast Nuclear Spin Relaxation in Hyperpolarized Solid 129Xe. *Physical Review Letters* 2002; 88:147602.

[36] Cates GD, Benton DR, Gatzke M, Happer W, Hasson KC, Newbury NR. Laser production of large nuclear-spin polarization in frozen xenon. *Physical Review Letters* 1990; 65:2591–2594.

[37] Burant A, Branca RT. Diffusion-mediated 129Xe gas depolarization in magnetic field gradients during continuous-flow optical pumping. *Journal of Magnetic Resonance* 2016; 273:124–129.

[38] Saam BT, Conradi MS. Low Frequency NMR Polarimeter for Hyperpolarized Gases. *Journal of Magnetic Resonance* 1998; 134:67–71.

[39] Asfour A. A new DAQ-based and versatile low-cost NMR spectrometer working at very-low magnetic field (4.5 mT): a palette of potential applications. In: *2008 IEEE Instrumentation and Measurement Technology Conference*, Victoria, Vancouver Island, British Colombia, 2008. pp. 697–701.

[40] Asfour A. A novel NMR instrument for the in-situ monitoring of the absolute polarization of laser-polarized 129Xe. *Journal of Biomedical Science and Engineering* 2010; 03:1099–1107.

[41] Asfour A. Low-Field NMR/MRI Systems Using LabVIEW and Advanced Data-Acquisition Techniques. *in* "Practical Applications and Solutions Using LabVIEW Software" (Folea S, Ed.), pp. 17–40. InTech, 2011.

[42] ClaasenVujčič T, Borsboom HM, Gaykema HJG, Mehlkopf T. Transverse low-field RF coils in MRI. *Magnetic Resonance in Medicine* 1996; 36:111–116.

[43] Carias MF, DominguezViqueria W, Santyr GE. Improving Signal-to-Noise Ratio of Hyperpolarized Noble Gas MR Imaging at 73.5 mT Using Multiturn Litz Wire Radiofrequency Receive Coils. *Concepts in Magnetic Resonance Part B: Magnetic Resonance Engineering* 2011; 39 B:37–42.

[44] Espy M, Matlashov A, Volegov P. SQUID-detected ultra-low field MRI. *Journal of Magnetic Resonance* 2013; 229:127–141.

[45] Sarracanie M, LaPierre CD, Salameh N, Waddington DEJ, Witzel T, Rosen MS. Low-Cost High-Performance MRI. *Scientific Reports* 2015; 5:15177.

[46] Michal CA. A low-cost spectrometer for NMR measurements in the Earth's magnetic field. *Measurement Science and Technology* 2010; 21:105902.

[47] Korchak SE, Kilian W, Mitschang L. Configuration and Performance of a Mobile 129Xe Polarizer. *Applied Magnetic Resonance* 2013; 44:65–80.

[48] Hersman FW, Distelbrink JH, Ketel S, Ketel J, Porter W, Watt D, Ruset IC. Chapter 5. Large Volume and Continuous Flow Hyperpolarization. *in* "Hyperpolarized 129Xe Magnetic Resonance", pp. 86–95. Royal Society of Chemistry, 2015.

[49] Zook AL, Adhyaru BB, Bowers CR. High capacity production of >65% spin polarized xenon-129 for NMR spectroscopy and imaging. *Journal of Magnetic Resonance* 2002; 159:175–182.

[50] Appelt S, Ünlü T, Zilles K, Shah NJ, BaerLang S, Halling H. Experimental studies of rubidium absolute polarization at high temperatures. *Applied Physics Letters* 1999; 75:427–429.

[51] Appelt S, Baranga ABA, Young AR, Happer W. Light narrowing of rubidium magnetic-resonance lines in high-pressure optical-pumping cells. *Physical Review A* 1999; 59:2078–2084.

[52] Nesmeyanov AN, "Vapor Pressure of the Elements". Academic Press, New York, 1964.

[53] Vdović S, Sarkisyan D, Pichler G. Absorption spectrum of rubidium and cesium dimers by compact computer operated spectrometer. *Optics Communications* 2006; 268:58–63.

[54] Beuc R, Movre M, Horvatic V, Vadla C, Dulieu O, Aymar M. Absorption spectroscopy of the rubidium dimer in an overheated vapor: An accurate check of molecular structure and dynamics. *Physical Review A* 2007; 75:032512.

[55] Newton H, Walkup LL, Whiting N, West L, Carriere J, Havermeyer F, Ho L, Morris P, Goodson BM, Barlow MJ. Comparative study of in situ N2 rotational Raman spectroscopy methods for probing energy thermalisation processes during spin-exchange optical pumping. *Applied Physics B: Lasers and Optics* 2014; 115:167–172.

[56] Budker D, Kimball DF, DeMille DP, "Atomic Physics: An Exploration through Problems and Solutions". Oxford University Press, Oxford, 2nd ed., 2008.

[57] Zheng HJ, Quan W, Liu X, Chen Y, Lu JX. Determination of Atomic Number Densities of 87Rb and 3He Based on Absorption Spectroscopy. *Chinese Physics Letters* 2014; 31:103203.

[58] Killian TJ. Thermionic Phenomena Caused By Vapors of Rubidium and Potassium. *Physical Review* 1926; 27:578–587.

[59] Shah NJ, Ünlü T, Wegener HP, Halling H, Zilles K, Appelt S. Measurement of rubidium and xenon absolute polarization at high temperatures as a means of improved production of hyperpolarized 129Xe. *NMR in Biomedicine* 2000; 13:214–219.

[60] Nikolaou P, Coffey AM, Ranta K, Walkup LL, Gust BM, Barlow MJ, Rosen MS, Goodson BM, Chekmenev EY. Multidimensional Mapping of Spin-Exchange Optical Pumping in Clinical-Scale Batch-Mode 129Xe Hyperpolarizers. *The Journal of Physical Chemistry B* 2014; 118:4809–4816.

[61] Whiting N, Nikolaou P, Eschmann NA, Barlow MJ, Lammert R, Ungar J, Hu W, Vaissie L, Goodson BM. Using frequency-narrowed, tunable laser diode arrays with integrated volume holographic gratings for spin-exchange optical pumping at high resonant fluxes and xenon densities. *Applied Physics B* 2012; 106:775–788.

[62] Freeman MS. "The Efficiency Limits of Spin Exchange Optical Pumping Methods of 129Xe Hyperpolarization: Implications for in vivo MRI Applications". Phd thesis, Duke University, 2015.

[63] Zeng X, Miron E, Van Wijngaarden WA, Schreiber D, Happer W. Wall relaxation of spin polarized 129Xe nuclei. *Physics Letters A* 1983; 96:191–194.

[64] Fujiwara H, Kimura A, Yanagawa Y, Kamiya T, Hattori M, Hiraga T. Relaxation Behavior of Laser-Polarized 129Xe Gas: Size Dependency and Wall Effect of the T1 Relaxation Time in Glass and Gelatin Bulbs. *Journal of Magnetic Resonance* 2001; 150:156–160.

[65] Ramsey NF. Magnetic Shielding of Nuclei in Molecules. *Physical Review* 1950; 78:699–703.

[66] Jameson CJ. Understanding NMR Chemical Shifts. *Annual Review of Physical Chemistry* 1996; 47:135–169.

[67] Cavalli A, Salvatella X, Dobson CM, Vendruscolo M. Protein structure determination from NMR chemical shifts. *Proceedings of the National Academy of Sciences* 2007; 104:9615–9620.

[68] Facelli JC, Ferraro MB. From NMR spectra to structure. *Concepts in Magnetic Resonance Part A* 2013; 42:261–289.

[69] Cherubini A, Bifone A. Hyperpolarised xenon in biology. *Progress in Nuclear Magnetic Resonance Spectroscopy* 2003; 42:1–30.

[70] Pietraiß T, Gaede HC. Optically Polarized 129Xe in NMR Spectroscopy. *Advanced Materials* 1995; 7:826–838.

[71] Jameson AK, Jameson CJ, Gutowsky HS. Density Dependence of 129Xe Chemical Shifts in Mixtures of Xenon and Other Gases. *The Journal of Chemical Physics* 1970; 53:2310–2321.

[72] Jameson CJ, Jameson AK, Cohen SM. Temperature and density dependence of 129Xe chemical shift in xenon gas. *The Journal of Chemical Physics* 1973; 59:4540–4546.

[73] Jameson CJ, Jameson AK, Cohen SM. Temperature and density dependence of 129Xe chemical shift in rare gas mixtures. *The Journal of Chemical Physics* 1975; 62:4224–4226.

[74] Acosta RH, Blümler P, Münnemann K, Spiess HW. Mixture and dissolution of laser polarized noble gases: Spectroscopic and imaging applications. *Progress in Nuclear Magnetic Resonance Spectroscopy* 2012; 66:40–69.

[75] Jokisaari J. NMR of noble gases dissolved in isotropic and anisotropic liquids. *Progress in Nuclear Magnetic Resonance Spectroscopy* 1994; 26:1–26.

[76] Lim YH, Nugara N, King AD. NMR chemical shifts of 129Xe dissolved in various oxygen and nitrogen substituted straight chain aliphatic compounds. *Applied Magnetic Resonance* 1995; 8:521–534.

[77] Patton B, Kuzma NN, Happer W. Chemical shift of hyperpolarized 129Xe dissolved in liquid nitrogen. *Physical Review B* 2001; 65:020404.

[78] Goodson BM. Nuclear magnetic resonance of laser-polarized noble gases in molecules, materials, and organisms. *Journal of Magnetic Resonance* 2002; 155:157–216.

[79] Jameson CJ, Sears DN, Murad S. Molecular dynamics averaging of Xe chemical shifts in liquids. *The Journal of Chemical Physics* 2004; 121:9581–9592.

[80] Barskiy DA, Coffey AM, Nikolaou P, Mikhaylov DM, Goodson BM, Branca RT, Lu GJ, Shapiro MG, Telkki Vv, Zhivonitko VV, Koptyug IV, Salnikov OG, Kovtunov KV, Bukhtiyarov VI, Rosen MS, Barlow MJ, Safavi S, Hall IP, Schröder L, Chekmenev EY. NMR Hyperpolarization Techniques of Gases. *Chemistry - A European Journal* 2017; 23:725–751.

[81] Miller KW, Reot NV, Uiterkampt AJMS, Stengle DP, Stengle TR, Williamson KL. Xenon NMR: Chemical shifts of a general anesthetic in common solvents, proteins, and membranes. *Proceedings of the National Academy of Sciences* 1981; 78:4946–4949.

[82] Yuan H, Murad S, Jameson CJ, Olson JD. Molecular Dynamics Simulations of Xe Chemical Shifts and Solubility in n-Alkanes. *The Journal of Physical Chemistry C* 2007; 111:15771–15783.

[83] Moller HE, Chawla MS, Chen XJ, Driehuys B, Hedlund LW, Wheeler CT, Johnson GA. Magnetic resonance angiography with hyperpolarized 129Xe dissolved in a lipid emulsion. *Magnetic Resonance in Medicine* 1999; 41:1058–1064.

[84] Venkatesh AK, Zhao L, Balamore D, Jolesz FA, Albert MS. Evaluation of carrier agents for hyperpolarized xenon MRI. *NMR in Biomedicine* 2000; 13:245–252.

[85] Duhamel G, Choquet P, Leviel JL, Steibel J, Lamalle L, Julien C, Kober F, Grillon E, Derouard J, Décorps M, Ziegler A, Constantinesco A. In vivo 129Xe NMR in rat brain during intra-arterial injection of hyperpolarized 129Xe dissolved in a lipid emulsion. *Comptes Rendus de l'Académie des Sciences - Series III - Sciences de la Vie* 2000; 323:529–536.

[86] Chen RY, Fan FC, Kim S, Jan KM, Usami S, Chien S. Tissue-blood partition coefficient for xenon: temperature and hematocrit dependence. *Journal of Applied Physiology: Respiratory, Environmental and Exercise Physiology* 1980; 49:178–83.

[87] Cleveland ZI, Cofer GP, Metz G, Beaver D, Nouls J, Kaushik SS, Kraft M, Wolber J, Kelly KT, McAdams HP, Driehuys B. Hyperpolarized 129Xe MR Imaging of Alveolar Gas Uptake in Humans. *PLoS ONE* 2010; 5:e12192.

[88] Zhou X. Hyperpolarized Noble Gases as Contrast Agents. *in* "Methods in Molecular Biology", pp. 189–204. Springer Science+Business Media, 2011.

[89] Sase S, Takahashi H, Shigefuku R, Ikeda H, Kobayashi M, Matsumoto N, Suzuki M. Measurement of blood flow and xenon solubility coefficient in the human liver by xenon-enhanced computed tomography. *Medical Physics* 2012; 39:7553.

[90] Isbister W, Schofield P, Torrance H. Measurement of the Solubility of Xenon-133 in Blood and Human Brain. *Physics in Medicine & Biology* 1965; 10:243–250.

[91] Ripmeester JA, Ratcliffe CI. Application of xenon-129 NMR to the study of microporous solids. *The Journal of Physical Chemistry* 1990; 94:7652–7656.

[92] Huang SJ, Huh S, Lo PS, Liu SH, Lin VS, Liu SB. Hyperpolarized 129Xe NMR investigation of multifunctional organic/inorganic hybrid mesoporous silica materials. *Physical Chemistry Chemical Physics* 2005; 7:3080–3087.

[93] Farina M, Mauri M, Patriarca G, Simonutti R, Klasson KT, Cheng HN. 129Xe NMR studies of morphology and accessibility in porous biochar from almond shells. *RSC Advances* 2016; 6:103803–103810.

[94] Weiland E, SpringuelHuet MA, Nossov A, Gédéon A. 129Xenon NMR: Review of recent insights into porous materials. *Microporous and Mesoporous Materials* 2016; 225:41–65.

[95] Trepte K, Schwalbe S, Schaber J, Krause S, Senkovska I, Kaskel S, Brunner E, Kortus J, Seifert G. Theoretical and experimental investigations of 129Xe NMR chemical shift isotherms in metal-organic frameworks. *Physical Chemistry Chemical Physics* 2018; 20:25039–25043.

[96] Xu S, Li X, Sun C, Zheng A, Zhang W, Han X, Liu X, Bao X. Mapping the dynamics of methanol and xenon co-adsorption in SWNTs by in situ continuous-flow hyperpolarized 129Xe NMR. *Physical Chemistry Chemical Physics* 2019; 21:3287–3293.

[97] Mugler JP, Driehuys B, Brookeman JR, Cates GD, Berr SS, Bryant RG, Daniel TM, De Lange EE, Downs JH, Erickson CJ, Happer W, Hinton DP, Kassel NF, Maier T, Phillips CD, Saam BT, Sauer KL, Wagshul ME. MR imaging and spectroscopy using hyperpolarized 129Xe gas: Preliminary human results. *Magnetic Resonance in Medicine* 1997; 37:809–815.

[98] Möller HE, Chen X, Chawla MS, Driehuys B, Hedlund LW, Johnson G. Signal Dynamics in Magnetic Resonance Imaging of the Lung with Hyperpolarized Noble Gases. *Journal of Magnetic Resonance* 1998; 135:133–143.

[99] Mugler JP, Altes TA, Ruset IC, Dregely IM, Mata JF, Miller GW, Ketel S, Ketel J, Hersman FW, Ruppert K. Simultaneous magnetic resonance imaging of ventilation distribution and gas uptake in the human lung using hyperpolarized xenon-129. *Proceedings of the National Academy of Sciences* 2010; 107:21707–21712.

[100] Robertson SH, Virgincar RS, Bier EA, He M, Schrank GM, Smigla RM, Rackley C, McAdams HP, Driehuys B. Uncovering a third dissolved-phase 129Xe resonance in the human lung: Quantifying spectroscopic features in healthy subjects and patients with idiopathic pulmonary fibrosis. *Magnetic Resonance in Medicine* 2017; 78:1306–1315.

[101] Qing K, Ruppert K, Jiang Y, Mata JF, Miller GW, Shim YM, Wang C, Ruset IC, Hersman FW, Altes Ta, Mugler JP. Regional mapping of gas uptake by blood and tissue in the human lung using hyperpolarized xenon-129 MRI. *Journal of Magnetic Resonance Imaging* 2014; 39:346–359.

[102] Cleveland ZI, Virgincar RS, Qi Y, Robertson SH, Degan S, Driehuys B. 3D MRI of impaired hyperpolarized 129Xe uptake in a rat model of pulmonary fibrosis. *NMR in Biomedicine* 2014; 27:1502–1514.

[103] Ruppert K, Altes TA, Mata JF, Ruset IC, Hersman FW, Mugler JP. Detecting pulmonary capillary blood pulsations using hyperpolarized xenon-129 chemical shift saturation recovery (CSSR) MR spectroscopy. *Magnetic Resonance in Medicine* 2016; 75:1771–1780.

[104] Norquay G, Leung G, Stewart NJ, Wolber J, Wild JM. 129Xe chemical shift in human blood and pulmonary blood oxygenation measurement in humans using hyperpolarized 129Xe NMR. *Magnetic Resonance in Medicine* 2017; 77:1399–1408.

[105] Kern AL, Gutberlet M, Qing K, Voskrebenzev A, Klimeš F, Kaireit TF, Czerner C, Biller H, Wacker F, Ruppert K, Hohlfeld JM, VogelClaussen J. Regional investigation of lung function and microstructure parameters by localized 129Xe chemical shift saturation recovery and dissolved-phase imaging: A reproducibility study. *Magnetic Resonance in Medicine* 2019; 81:13–24.

[106] Norquay G, Wolber J, Wild JM. Chapter 20. 129Xe Chemical Shift and Spin-Lattice Relaxation Dependences on Blood Oxygenation. *in* "Hyperpolarized 129Xe Magnetic Resonance", pp. 365–391. Royal Society of Chemistry, 2015.

[107] Kilian W, Seifert F, Rinneberg H. Dynamic NMR spectroscopy of hyperpolarized 129Xe in human brain analyzed by an uptake model. *Magnetic Resonance in Medicine* 2004; 51:843–847.

[108] Mazzanti ML, Walvick RP, Zhou X, Sun Y, Shah N, Mansour J, Gereige J, Albert MS. Distribution of hyperpolarized xenon in the brain following sensory stimulation: Preliminary MRI findings. *PLoS ONE* 2011; 6.

[109] Branca RT, He T, Zhang L, Floyd CS, Freeman M, White C, Burant A. Detection of brown adipose tissue and thermogenic activity in mice by hyperpolarized xenon MRI. *Proceedings of the National Academy of Sciences* 2014; 111:18001–18006.

[110] Fox MS, Couch MJ, Albert MS. Chapter 22. Magnetic Resonance Imaging of the Brain using Hyperpolarized 129Xe. *in* "Hyperpolarized 129Xe Magnetic Resonance" (Reimer P, Parizel PM, Meaney JFM, Stichnoth FA, Eds.), pp. 407–425. Royal Society of Chemistry, Berlin, Heidelberg, 2015.

[111] Branca RT, Zhang L, Burant A, Katz L, McCallister A. Detection of human brown adipose tissue by MRI with hyperpolarized Xe-129 gas and validation by FDG-PET/MRI. In: *Proceedings of the International Society of Magnetic Resonance in Medicine*, Singapore, 2016. p. 1054.

[112] Miller GW, Cates GD, Keder D, Altes TA, Mata JF, Qing K, Ruset I, Hersman FW, Mugler JP. Dynamic Spectroscopy of Dissolved-Phase Xenon-129 in the Human Kidney. In: *Proceedings of the International Society of Magnetic Resonance in Medicine*, Honolulu, 2017. p. 1182.

[113] Li T, Hane FT, LawrenceDewar JM, Hassan A, Granberg K, Pellizzari RM, Plata JA, Albert MS. Using Hyperpolarized 129Xe MRI to Detect Impaired Cerebral Perfusion in Human Brain with Alzheimer's Disease. In: *Proceedings of the International Society of Magnetic Resonance in Medicine*, Honolulu, 2017. p. 0487.

[114] Branca RT, McCallister A, Yuan H, Aghajanian A, Faber JE, Weimer N, Buchanan R, Floyd CS, Antonacci M, Zhang L, Burant A. Accurate quantification of brown adipose tissue mass by xenon-enhanced computed tomography. *Proceedings of the National Academy of Sciences* 2018; 115:174–179.

[115] Chang YV, Quirk JD, Ruset IC, Atkinson JJ, Hersman FW, Woods JC. Quantification of human lung structure and physiology using hyperpolarized 129Xe. *Magnetic Resonance in Medicine* 2014; 71:339–344.

[116] Bier EA, Robertson SH, Schrank GM, Rackley C, Mammarappallil JG, Rajagopal S, McAdams HP, Driehuys B. A protocol for quantifying cardiogenic oscillations in dynamic 129Xe gas exchange spectroscopy: The effects of idiopathic pulmonary fibrosis. *NMR in Biomedicine* 2018; p. e4029.

[117] Qing K, Mugler J, Chen Q. WE-FG-206-07: Assessing the Lung Function of Patients with Non-Small Cell Lung Cancer Using Hyperpolarized Xenon-129 Dissolved-Phase MRI. *Medical Physics* 2016; 43:3832–3832.

[118] Kaushik SS, Freeman MS, Yoon SW, Liljeroth MG, Stiles JV, Roos JE, Michael Foster WS, Rackley CR, McAdams HP, Driehuys B. Measuring diffusion limitation with a perfusion-limited gas–Hyperpolarized 129Xe gas-transfer spectroscopy in patients with idiopathic pulmonary fibrosis. *Journal of Applied Physiology* 2014; 117:577–585.

[119] Stewart NJ, Norquay G, Griffiths PD, Wild JM. Feasibility of human lung ventilation imaging using highly polarized naturally abundant xenon and optimized three-dimensional steady-state free precession. *Magnetic Resonance in Medicine* 2015; 74:346–352.

[120] Liu Z, Araki T, Okajima Y, Albert M, Hatabu H. Pulmonary hyperpolarized noble gas MRI: Recent advances and perspectives in clinical application. *European Journal of Radiology* 2014; 83:1282–1291.

[121] Zhou X, Sun Y, Mazzanti M, Henninger N, Mansour J, Fisher M, Albert M. MRI of stroke using hyperpolarized 129Xe. *NMR in Biomedicine* 2011; 24:170–175.

[122] Rao M, Stewart NJ, Norquay G, Griffiths PD, Wild JM. High resolution spectroscopy and chemical shift imaging of hyperpolarized 129Xe dissolved in the human brain in vivo at 1.5 tesla. *Magnetic Resonance in Medicine* 2016; 75:2227–2234.

[123] Burant A, Zhang L, McCallister A, Branca RT. In Vivo Temperature Imaging Using Lipid-dissolved Hyperpolarized Xenon-129. In: *Proceedings of 56th Experimental Nuclear Magnetic Resonance Conference*, Pacific Grove, 2015. p. 87.

[124] Norquay G, Stewart NJ, Wild JM. Evaluation of 129Xe-RBC signal dynamics and chemical shift in the cardiopulmonary circuit using hyperpolarized 129Xe NMR. In: *Proceedings of the International Society of Magnetic Resonance in Medicine*, Honolulu, 2017. p. 3327.

[125] Swanson SD, Rosen MS, Coulter KP, Welsh RC, Chupp TE. Distribution and dynamics of laser-polarized 129Xe magnetization in vivo. *Magnetic Resonance in Medicine* 1999; 42:1137–1145.

[126] Kershaw J, Nakamura K, Kondoh Y, Wakai A, Suzuki N, Kanno I. Confirming the existence of five peaks in 129Xe rat head spectra. *Magnetic Resonance in Medicine* 2007; 57:791–797.

[127] Nakamura K, Kondoh Y, Wakai A, Kershaw J, Wright D, Kanno I. 129Xe spectra from the heads of rats with and without ligation of the external carotid and pterygopalatine arteries. *Magnetic Resonance in Medicine* 2005; 53:528–534.

[128] Virgincar RS, Robertson SH, Nouls J, Degan S, Schrank GM, He M, Driehuys B. Establishing an accurate gas phase reference frequency to quantify 129Xe chemical shifts in vivo. *Magnetic Resonance in Medicine* 2017; 77:1438–1445.

[129] Jameson CJ, Keith Jameson A. Density dependence of 129Xe N.M.R. chemical shifts in O2 and NO. *Molecular Physics* 1971; 20:957–959.

[130] Jameson CJ, Jameson AK, Cohen SM. 129Xe contact shift in oxygen gas. *Molecular Physics* 1975; 29:1919–1927.

[131] Marques JP, Bowtell R. Application of a fourier-based method for rapid calculation of field inhomogeneity due to spatial variation of magnetic susceptibility. *Concepts in Magnetic Resonance Part B: Magnetic Resonance Engineering* 2005; 25:65–78.

[132] Bhagwandien R, Moerland M, Bakker C, Beersma R, Lagendijk J. Numerical analysis of the magnetic field for arbitrary magnetic susceptibility distributions in 3D. *Magnetic Resonance Imaging* 1994; 12:101–107.

[133] Truong TK, Clymer BD, Chakeres DW, Schmalbrock P. Three-dimensional numerical simulations of susceptibility-induced magnetic field inhomogeneities in the human head. *Magnetic Resonance Imaging* 2002; 20:759–770.

[134] Collins CM, Yang B, Yang QX, Smith MB. Numerical calculations of the static magnetic field in three-dimensional multi-tissue models of the human head. *Magnetic Resonance Imaging* 2002; 20:413–424.

[135] Dewal RP, Yang QX. Volume of interest-based fourier transform method for calculation of static magnetic field maps from susceptibility distributions. *Magnetic Resonance in Medicine* 2016; 75:2473–2480.

[136] Duhamel G, Choquet P, Grillon E, Lamalle L, Leviel JL, Ziegler A, Constantinesco A. Xenon-129 MR imaging and spectroscopy of rat brain using arterial delivery of hyperpolarized xenon in a lipid emulsion. *Magnetic Resonance in Medicine* 2001; 46:208–212.

[137] Wakai A, Kershaw J, Nakamura K, Iida H, Tamura H, Kondoh Y, Kanno I. Magnetic Resonance Spectra of Hyperpolarized 129Xe in Human Blood and Living Rat Chest. *Magnetic Resonance in Medical Sciences* 2003; 2:189–194.

[138] Zhou X, Mazzanti ML, Chen JJ, Tzeng YS, Mansour JK, Gereige JD, Venkatesh AK, Sun Y, Mulkern RV, Albert MS. Reinvestigating hyperpolarized 129Xe longitudinal relaxation time in the rat brain with noise considerations. *NMR in Biomedicine* 2008; 21:217–225.

[139] Fedorov A, Beichel R, KalpathyCramer J, Finet J, FillionRobin JC, Pujol S, Bauer C, Jennings D, Fennessy F, Sonka M, Buatti J, Aylward S, Miller JV, Pieper S, Kikinis R. 3D Slicer as an image computing platform for the Quantitative Imaging Network. *Magnetic Resonance Imaging* 2012; 30:1323–1341.

[140] Kazhdan M, Hoppe H. Screened poisson surface reconstruction. *ACM Transactions on Graphics* 2013; 32:1–13.

[141] Cignoni P, Callieri M, Corsini M, Dellepiane M, Ganovelli F, Ranzuglia G. MeshLab: an Open-Source Mesh Processing Tool. *Sixth Eurographics Italian Chapter Conference* 2008; pp. 129–136.

[142] Schenck JF. The role of magnetic susceptibility in magnetic resonance imaging: MRI magnetic compatibility of the first and second kinds. *Medical Physics* 1996; 23:815–850.

[143] Jackson JD, "Classical Electrodynamics". John Wiley & Sons, Inc., Hoboken, 3rd ed., 1999.

[144] Zangwill A, "Modern Electrodynamics". Cambridge University Press, New York, 2013.

[145] Kuchel PW, Bulliman BT. Perturbation of homogeneous magnetic fields by isolated single and confocal spheroids. Implications for NMR spectroscopy of cells. *NMR in Biomedicine* 1989; 2:151–160.

[146] Zhang L, Burant A, McCallister A, Zhao V, Koshlap KM, Degan S, Antonacci M, Branca RT. Accurate MR thermometry by hyperpolarized 129Xe. *Magnetic Resonance in Medicine* 2017; 78:1070–1079.

[147] Nouls J, Fanarjian M, Hedlund L, Driehuys B. A constant-volume ventilator and gas recapture system for hyperpolarized gas MRI of mouse and rat lungs. *Concepts in Magnetic Resonance Part B: Magnetic Resonance Engineering* 2011; 39B:78–88.

[148] Bashir A, Yablonskiy DA. Natural linewidth chemical shift imaging (NL-CSI). *Magnetic Resonance in Medicine* 2006; 56:7–18.

[149] Norquay G, Leung G, Stewart NJ, Tozer GM, Wolber J, Wild JM. Relaxation and exchange dynamics of hyperpolarized 129Xe in human blood. *Magnetic Resonance in Medicine* 2015; 74:303–311.

[150] Schneider WG, Bernstein HJ, Pople JA. Proton Magnetic Resonance Chemical Shift of Free (Gaseous) and Associated (Liquid) Hydride Molecules. *The Journal of Chemical Physics* 1958; 28:601–607.

[151] Muller N, Reiter RC. Temperature Dependence of Chemical Shifts of Protons in Hydrogen Bonds. *The Journal of Chemical Physics* 1965; 42:3265–3269.

[152] Kuroda K. Temperature Monitoring Using Chemical Shift. *in* "eMagRes", Vol. 5, pp. 1121–1130. American Cancer Society, 2016.

[153] Van Geet AL. Calibration of the methanol and glycol nuclear magnetic resonance thermometers with a static thermistor probe. *Analytical Chemistry* 1968; 40:2227–2229.

[154] Van Geet AL. Calibration of methanol nuclear magnetic resonance thermometer at low temperature. *Analytical Chemistry* 1970; 42:679–680.

[155] Rieke V, Butts Pauly K. MR thermometry. *Journal of Magnetic Resonance Imaging* 2008; 27:376–390.

[156] van der Graaf M. In vivo magnetic resonance spectroscopy: basic methodology and clinical applications. *European Biophysics Journal* 2010; 39:527–540.

[157] Cady EB, D'Souza PC, Penrice J, Lorek A. The estimation of local brain temperature by in vivo 1H magnetic resonance spectroscopy. *Magnetic Resonance in Medicine* 1995; 33:862–867.

[158] Thrippleton MJ, Parikh J, Harris BA, Hammer SJ, Semple SIK, Andrews PJD, Wardlaw JM, Marshall I. Reliability of MRSI brain temperature mapping at 1.5 and 3 T. *NMR in Biomedicine* 2014; 27:183–190.

[159] Weis J, Covaciu L, Rubertsson S, Allers M, Lunderquist A, Ahlström H. Noninvasive monitoring of brain temperature during mild hypothermia. *Magnetic Resonance Imaging* 2009; 27:923–932.

[160] Bainbridge A, Kendall GS, Vita ED, Hagmann C, Kapetanakis A, Cady EB, Robertson NJ. Regional neonatal brain absolute thermometry by 1H MRS. *NMR in Biomedicine* 2013; 26:416–423.

[161] Sone D, Ikegaya N, Takahashi A, Sumida K, Ota M, Saito T, Kimura Y, Matsuda H, Sato N. Noninvasive detection of focal brain hyperthermia related to continuous epileptic activities using proton MR spectroscopy. *Epilepsy Research* 2017; 138:1–4.

[162] Mintzopoulos D, Ratai EM, He J, Gonzalez RG, Kaufman MJ. Simian immunodeficiency virus transiently increases brain temperature in rhesus monkeys: detection with magnetic resonance spectroscopy thermometry. *Magnetic Resonance in Medicine* 2019; 00:1–9.

[163] Zhu M, Bashir A, Ackerman JJ, Yablonskiy DA. Improved calibration technique for in vivo proton MRS thermometry for brain temperature measurement. *Magnetic Resonance in Medicine* 2008; 60:536–541.

[164] BabourinaBrooks B, Simpson R, Arvanitis TN, Machin G, Peet AC, Davies NP. MRS thermometry calibration at 3T: Effects of protein, ionic concentration and magnetic field strength. *NMR in Biomedicine* 2015; 28:792–800.

[165] Hectors SJ, Jacobs I, Moonen CT, Strijkers GJ, Nicolay K. MRI methods for the evaluation of high intensity focused ultrasound tumor treatment: Current status and future needs. *Magnetic Resonance in Medicine* 2016; 75:302–317.

[166] Merckel LG, Knuttel FM, Deckers R, van Dalen T, Schubert G, Peters NHGM, Weits T, van Diest PJ, Mali WPTM, Vaessen PHHB, van Gorp JMHH, Moonen CTW, Bartels LW, van den Bosch MAAJ. First clinical experience with a dedicated MRI-guided high-intensity focused ultrasound system for breast cancer ablation. *European Radiology* 2016; 26:4037–4046.

[167] Deckers R, Merckel LG, Denis de Senneville B, Schubert G, Köhler M, Knuttel FM, Mali WPTM, Moonen CTW, van den Bosch MAAJ, Bartels LW. Performance analysis of a dedicated breast MR-HIFU system for tumor ablation in breast cancer patients. *Physics in Medicine and Biology* 2015; 60:5527–5542.

[168] Wijlemans JW, de Greef M, Schubert G, Bartels LW, Moonen CT, van den Bosch MA, Ries M. A Clinically Feasible Treatment Protocol for Magnetic Resonance-Guided High-Intensity Focused Ultrasound Ablation in the Liver. *Investigative Radiology* 2015; 50:24–31.

[169] Bour P, Marquet F, Ozenne V, Toupin S, Dumont E, Aubry JF, LepetitCoiffe M, Quesson B. Real-time monitoring of tissue displacement and temperature changes during MR-guided high intensity focused ultrasound. *Magnetic Resonance in Medicine* 2017; 78:1911–1921.

[170] Zachiu C, Denis de Senneville B, Dmitriev ID, Moonen CTW, Ries M. A framework for continuous target tracking during MR-guided high intensity focused ultrasound thermal ablations in the abdomen. *Journal of Therapeutic Ultrasound* 2017; 5:27.

[171] Quesson B, Laurent C, Maclair G, de Senneville BD, Mougenot C, Ries M, Carteret T, Rullier A, Moonen CT. Real-time volumetric MRI thermometry of focused ultrasound ablation in vivo: a feasibility study in pig liver and kidney. *NMR in Biomedicine* 2011; 24:145–153.

[172] van Breugel JMM, de Greef M, Wijlemans JW, Schubert G, van den Bosch MAAJ, Moonen CTW, Ries MG. Thermal ablation of a confluent lesion in the porcine kidney with a clinically available MR-HIFU system. *Physics in Medicine & Biology* 2017; 62:5312–5326.

[173] Eranki A, Farr N, Partanen A, Sharma KV, Rossi CT, Rosenberg AZ, Kim A, Oetgen M, Celik H, Woods D, Yarmolenko PS, Kim PC, Wood BJ. Mechanical fractionation of tissues using microsecond-long HIFU pulses on a clinical MR-HIFU system. *International Journal of Hyperthermia* 2018; 34:1213–1224.

[174] Sprinkhuizen SM, Konings MK, van der Bom MJ, Viergever MA, Bakker CJG, Bartels LW. Temperature-induced tissue susceptibility changes lead to significant temperature errors in PRFS-based MR thermometry during thermal interventions. *Magnetic Resonance in Medicine* 2010; 64:1360–1372.

[175] McCallister D, Zhang L, Burant A, Katz L, Branca RT. Effect of microscopic susceptibility gradients on chemical-shift-based fat fraction quantification in supraclavicular fat. *Journal of Magnetic Resonance Imaging* 2019; 49:141–151.

[176] Sprinkhuizen SM, Bakker CJG, Ippel JH, Boelens R, Viergever MA, Bartels LW. Temperature dependence of the magnetic volume susceptibility of human breast fat tissue: an NMR study. *Magnetic Resonance Materials in Physics, Biology and Medicine* 2012; 25:33–39.

[177] Baron P, Deckers R, Bouwman JG, Bakker CJG, de Greef M, Viergever MA, Moonen CTW, Bartels LW. Influence of water and fat heterogeneity on fat-referenced MR thermometry. *Magnetic Resonance in Medicine* 2016; 75:1187–1197.

[178] Zhang L. "Temperature Dependence of the Chemical Shift of Lipid-dissolved 129Xe and Its Applications in MR Thermometry". PhD thesis, University of North Carolina at Chapel Hill, 2017.

[179] Poorter JD. Noninvasive MRI thermometry with the proton resonance frequency method: Study of susceptibility effects. *Magnetic Resonance in Medicine* 1995; 34:359–367.

[180] Kuroda K, Mulkern R, Oshio K, Panych L, Nakai T, Moriya T, Okuda S, Hynynen K, Joles F. Temperature mapping using the water proton chemical shift: Self-referenced method with echo-planar spectroscopic imaging. *Magnetic Resonance in Medicine* 2000; 43:220–225.

[181] Hernando D, Sharma SD, Kramer H, Reeder SB. On the confounding effect of temperature on chemical shift-encoded fat quantification. *Magnetic Resonance in Medicine* 2014; 72:464–470.

[182] Koskensalo K, Raiko J, Saari T, Saunavaara V, Eskola O, Nuutila P, Saunavaara J, Parkkola R, Virtanen KA. Human Brown Adipose Tissue Temperature and Fat Fraction Are Related to Its Metabolic Activity. *The Journal of Clinical Endocrinology & Metabolism* 2017; 102:1200–1207.

[183] Venkatesh AK, Hong KS, Kubatina L, Sun Y, Mulkern R, Ferenc A, Albert MS. Using dynamic hyperpolarized xenon MR to measure brain perfusion. *Proceedings of the International Society of Magnetic Resonance in Medicine* 2001; 9:951.

[184] Germain D, Chevallier P, Laurent A, SaintJalmes H. MR monitoring of tumour thermal therapy. *Magma: Magnetic Resonance Materials in Physics, Biology, and Medicine* 2001; 13:47–59.

[185] Nedergaard J, Cannon B. The Changed Metabolic World with Human Brown Adipose Tissue: Therapeutic Visions. *Cell Metabolism* 2010; 11:268–272.

[186] Cypess AM, Haft CR, Laughlin MR, Hu HH. Brown Fat in Humans: Consensus Points and Experimental Guidelines. *Cell Metabolism* 2014; 20:408–415.

[187] Lee P, Ho KKY, Lee P, Greenfield JR, Ho KKY, Greenfield JR. Hot fat in a cool man: infrared thermography and brown adipose tissue. *Diabetes, Obesity and Metabolism* 2011; 13:92–93.

[188] Yuan H, Jameson CJ, Gupta SK, Olson JD, Murad S. Prediction of Henry's constants of xenon in cyclo-alkanes from molecular dynamics simulations. *Fluid Phase Equilibria* 2008; 269:73–79.

[189] Pollack GL, Kennan RP, Himm JF, Stump DR. Diffusion of xenon in liquid alkanes: Temperature dependence measurements with a new method. Stokes-Einstein and hard sphere theories. *The Journal of Chemical Physics* 1990; 92:625–630.

[190] Jameson CJ. The Xenon Chemical Shift and Chemical Shift Anisotropy. *in* "Hyperpolarized 129Xe Magnetic Resonance", chapter 2, pp. 16–48. RSC Publishing, 2015.

[191] Jameson CJ, Stueber D. The nuclear magnetic resonance line shapes of Xe in the cages of clathrate hydrates. *Journal of Chemical Physics* 2004; 120:10200–10214.

[192] Stueber D, Jameson CJ. The chemical shifts of Xe in the cages of clathrate hydrate structures I and II. *Journal of Chemical Physics* 2004; 120:1560–1571.

[193] Cheung TTP. Temperature Dependence of 129Xe NMR of Xenon in Microporous Solids. *The Journal of Physical Chemistry* 1995; 99:7089–7095.

[194] Kromhout RA, Linder B. The effect of dispersion interaction on nuclear magnetic shielding. *Journal of Magnetic Resonance (1969)* 1969; 1:450–463.

[195] Stengle TR, Reo NV, Williamson KL. Nuclear magnetic resonance solvent shifts of xenon. A test of the reaction field model. *The Journal of Physical Chemistry* 1981; 85:3772–3775.

[196] Wolber J, Rowland IJ, Leach MO, Bifone A. Perfluorocarbon emulsions as intravenous delivery media for hyperpolarized xenon. *Magnetic Resonance in Medicine* 1999; 41:442–449.

[197] Ren J, Dimitrov I, Sherry AD, Malloy CR. Composition of adipose tissue and marrow fat in humans by 1H NMR at 7 Tesla. *Journal of Lipid Research* 2008; 49:2055–2062.

[198] Strobel K, van den Hoff J, Pietzsch J. Localized proton magnetic resonance spectroscopy of lipids in adipose tissue at high spatial resolution in mice in vivo. *Journal of Lipid Research* 2008; 49:473–480.

[199] Bao Q, Feng J, Chen L, Chen F, Liu Z, Jiang B, Liu C. A robust automatic phase correction method for signal dense spectra. *Journal of Magnetic Resonance* 2013; 234:82–89.

[200] O'Haver T. Command-line peak fitter for time-series signals, 2016.

[201] Antonacci M, Burant A, Wagner W, Branca RT. Depolarization of nuclear spin polarized 129Xe gas by dark rubidium during spin-exchange optical pumping. *Journal of Magnetic Resonance* 2017; 279:60–67.

[202] York D, Evensen NM, Martnez ML, De Basabe Delgado J. Unified equations for the slope, intercept, and standard errors of the best straight line. *American Journal of Physics* 2004; 72:367–375.

[203] Hovorková P, Laloučková K, Skivanová E. Determination of in vitro antibacterial activity of plant oils containing medium-chain fatty acids against Gram-positive pathogenic and gut commensal bacteria. *Czech Journal of Animal Science* 2018; 63:119–125.

[204] Cui Y, Hao P, Liu B, Meng X. Effect of traditional Chinese cooking methods on fatty acid profiles of vegetable oils. *Food Chemistry* 2017; 233:77–84.

[205] Hodson L, Skeaff CM, Fielding BA. Fatty acid composition of adipose tissue and blood in humans and its use as a biomarker of dietary intake. *Progress in Lipid Research* 2008; 47:348–380.

[206] Lim YH, King AD. NMR chemical shifts of xenon-129 dissolved in liquid n-alkanes and their mixtures. *The Journal of Physical Chemistry* 1993; 97:12173–12177.

[207] Kuroda K, Iwabuchi T, Obara M, Honda M, Saito K, Imai Y. Temperature dependence of relaxation times in proton components of fatty acids. *Magnetic Resonance in Medicine* 2011; 10:177–83.

[208] Luo L, Liu M. Adipose tissue in control of metabolism. *Journal of Endocrinology* 2016; 231:R77–R99.

[209] Cannon B, Nedergaard J. Brown Adipose Tissue: Function and Physiological Significance. *Physiological Reviews* 2004; 84:277–359.

[210] Inokuma Ki, OguraOkamatsu Y, Toda C, Kimura K, Yamashita H, Saito M. Uncoupling Protein 1 Is Necessary for Norepinephrine-Induced Glucose Utilization in Brown Adipose Tissue. *Diabetes* 2005; 54:1385–1391.

[211] Chouchani ET, Kazak L, Spiegelman BM. New Advances in Adaptive Thermogenesis: UCP1 and Beyond. *Cell Metabolism* 2019; 29:27–37.

[212] Enerbäck S, Jacobsson A, Simpson EM, Guerra C, Yamashita H, Harper ME, Kozak LP. Mice lacking mitochondrial uncoupling protein are cold-sensitive but not obese. *Nature* 1997; 387:90–94.

[213] Matthias A, Ohlson KBE, Fredriksson JM, Jacobsson A, Nedergaard J, Cannon B. Thermogenic Responses in Brown Fat Cells Are Fully UCP1-dependent. *Journal of Biological Chemistry* 2000; 275:25073–25081.

[214] Nedergaard J, Matthias A, Golozoubova V, Jacobsson A, Cannon B. UCP1: The original uncoupling protein - and perhaps the only one? *Journal of Bioenergetics and Biomembranes* 1999; 31:475–491.

[215] Kazak L, Chouchani ET, Jedrychowski MP, Erickson BK, Shinoda K, Cohen P, Vetrivelan R, Lu GZ, LaznikBogoslavski D, Hasenfuss SC, Kajimura S, Gygi SP, Spiegelman BM. A Creatine-Driven Substrate Cycle Enhances Energy Expenditure and Thermogenesis in Beige Fat. *Cell* 2015; 163:643–655.

[216] Ikeda K, Kang Q, Yoneshiro T, Camporez JP, Maki H, Homma M, Shinoda K, Chen Y, Lu X, Maretich P, Tajima K, Ajuwon KM, Soga T, Kajimura S. UCP1-independent signaling involving SERCA2b-mediated calcium cycling regulates beige fat thermogenesis and systemic glucose homeostasis. *Nature Medicine* 2017; 23:1454–1465.

[217] Bradley CA. Adipose tissue: Noncanonical beige fat thermogenesis. *Nature Reviews Endocrinology* 2017; 14:2–2.

[218] Ukropec J, Anunciado RP, Ravussin Y, Hulver MW, Kozak LP. UCP1-independent Thermogenesis in White Adipose Tissue of Cold-acclimated Ucp1-/- Mice. *Journal of Biological Chemistry* 2006; 281:31894–31908.

[219] Shabalina IG, Hoeks J, Kramarova TV, Schrauwen P, Cannon B, Nedergaard J. Cold tolerance of UCP1-ablated mice: A skeletal muscle mitochondria switch toward lipid oxidation with marked UCP3 up-regulation not associated with increased basal, fatty

acid- or ROS-induced uncoupling or enhanced GDP effects. *Biochimica et Biophysica Acta (BBA) - Bioenergetics* 2010; 1797:968–980.

[220] Jeanguillaume C, Metrard G, Ricquier D, Legras P, Bouchet F, Lacoeuille F, Hindre F, Morel O, Rakotonirina H. Visualization of Activated BAT in Mice, with FDG-PET and Its Relation to UCP1. *Advances in Molecular Imaging* 2013; .

[221] Olsen JM, Csikasz RI, Dehvari N, Lu L, Sandström A, Öberg AI, Nedergaard J, StoneElander S, Bengtsson T. β3-Adrenergically induced glucose uptake in brown adipose tissue is independent of UCP1 presence or activity: Mediation through the mTOR pathway. *Molecular Metabolism* 2017; 6:611–619.

[222] Sampath SC, Sampath SC, Bredella MA, Cypess AM, Torriani M. Imaging of Brown Adipose Tissue: State of the Art. *Radiology* 2016; 280:4–19.

[223] Hankir MK, Kranz M, Keipert S, Weiner J, Andreasen SG, Kern M, Patt M, Klöting N, Heiker JT, Brust P, Hesse S, Jastroch M, Fenske WK. Dissociation Between Brown Adipose Tissue 18F-FDG Uptake and Thermogenesis in Uncoupling Protein 1-Deficient Mice. *Journal of Nuclear Medicine* 2017; 58:1100–1103.

[224] Crandall JP, O JH, Gajwani P, Leal JP, Mawhinney DD, Sterzer F, Wahl RL. Measurement of Brown Adipose Tissue Activity Using Microwave Radiometry and 18F-FDG PET/CT. *Journal of Nuclear Medicine* 2018; 59:1243–1248.

[225] Gifford A, Towse TF, Walker RC, Avison MJ, Welch EB. Characterizing active and inactive brown adipose tissue in adult humans using PET-CT and MR imaging. *American Journal of Physiology - Endocrinology And Metabolism* 2016; 311:E95–E104.

[226] Cypess AM, Lehman S, Williams G, Tal I, Rodman D, Goldfine AB, Kuo FC, Palmer EL, Tseng YH, Doria A, Kolodny GM, Kahn CR. Identification and Importance of Brown Adipose Tissue in Adult Humans. *New England Journal of Medicine* 2009; 360:1509–1517.

[227] Blondin DP, Labbé SM, Noll C, Kunach M, Phoenix S, Guérin B, Turcotte ÉE, Haman F, Richard D, Carpentier AC. Selective Impairment of Glucose but Not Fatty Acid or Oxidative Metabolism in Brown Adipose Tissue of Subjects With Type 2 Diabetes. *Diabetes* 2015; 64:2388–2397.

[228] Ouellet V, Labbé SM, Blondin DP, Phoenix S, Guérin B, Haman F, Turcotte EE, Richard D, Carpentier AC. Brown adipose tissue oxidative metabolism contributes to energy expenditure during acute cold exposure in humans. *Journal of Clinical Investigation* 2012; 122:545–552.

[229] Crane JD, Mottillo EP, Farncombe TH, Morrison KM, Steinberg GR. A standardized infrared imaging technique that specifically detects UCP1-mediated thermogenesis in vivo. *Molecular Metabolism* 2014; 3:490–494.

[230] El Hadi H, Frascati A, Granzotto M, Silvestrin V, Ferlini E, Vettor R, Rossato M. Infrared thermography for indirect assessment of activation of brown adipose tissue in lean and obese male subjects. *Physiological Measurement* 2016; 37:N118–N128.

[231] Gatidis S, Schmidt H, Pfannenberg CA, Nikolaou K, Schick F, Schwenzer NF. Is It Possible to Detect Activated Brown Adipose Tissue in Humans Using Single-Time-Point Infrared Thermography under Thermoneutral Conditions? Impact of BMI and Subcutaneous Adipose Tissue Thickness. *PLoS ONE* 2016; 11:e0151152.

[232] Haq T, Crane JD, Kanji S, Gunn E, Tarnopolsky MA, Gerstein HC, Steinberg GR, Morrison KM. Optimizing the methodology for measuring supraclavicular skin temperature using infrared thermography; implications for measuring brown adipose tissue activity in humans. *Scientific Reports* 2017; 7:11934.

[233] Jang C, Jalapu S, Thuzar M, Law PW, Jeavons S, Barclay JL, Ho KK. Infrared thermography in the detection of brown adipose tissue in humans. *Physiological Reports* 2014; 2:e12167.

[234] Ang QY, Goh HJ, Cao Y, Li Y, Chan SP, Swain JL, Henry CJ, Leow MKS. A new method of infrared thermography for quantification of brown adipose tissue activation in healthy adults (TACTICAL): a randomized trial. *The Journal of Physiological Sciences* 2017; 67:395–406.

[235] Law J, Morris DE, IzziEngbeaya C, Salem V, Coello C, Robinson L, Jayasinghe M, Scott R, Gunn R, Rabiner E, Tan T, Dhillo WS, Bloom S, Budge H, Symonds ME. Thermal Imaging Is a Noninvasive Alternative to PET/CT for Measurement of Brown Adipose Tissue Activity in Humans. *Journal of Nuclear Medicine* 2018; 59:516–522.

[236] Jeong JH, Chang JS, Jo YH. Intracellular glycolysis in brown adipose tissue is essential for optogenetically induced nonshivering thermogenesis in mice. *Scientific Reports* 2018; 8:1–14.

[237] Meyer CW, Ootsuka Y, Romanovsky AA. Body Temperature Measurements for Metabolic Phenotyping in Mice. *Frontiers in Physiology* 2017; 8:520.

[238] Antonacci MA, Zhang L, Burant A, McCallister D, Branca RT. Simple and robust referencing system enables identification of dissolved-phase xenon spectral frequencies. *Magnetic Resonance in Medicine* 2018; 80:431–441.

[239] Antonacci MA, Zhang L, Degan S, Erdmann D, Branca RT. Calibration of methylene-referenced lipid-dissolved xenon frequency for absolute MR temperature measurements. *Magnetic Resonance in Medicine* 2019; 81:765–772.

[240] Kazak L, Chouchani ET, Lu GZ, Jedrychowski MP, Bare CJ, Mina AI, Kumari M, Zhang S, Vuckovic I, LaznikBogoslavski D, Dzeja P, Banks AS, Rosen ED, Spiegelman BM. Genetic Depletion of Adipocyte Creatine Metabolism Inhibits Diet-Induced Thermogenesis and Drives Obesity. *Cell Metabolism* 2017; 26:660–671.e3.

[241] Riley CL, Dao C, Kenaston MA, Muto L, Kohno S, Nowinski SM, Solmonson AD, Pfeiffer M, Sack MN, Lu Z, Fiermonte G, Sprague JE, Mills EM. The complementary and divergent roles of uncoupling proteins 1 and 3 in thermoregulation. *The Journal of Physiology* 2016; 594:7455–7464.

[242] Ruset IC, Ketel S, Hersman FW. Optical pumping system design for large production of hyperpolarized 129Xe. *Physical Review Letters* 2006; 96:8–11.

[243] Farhadi A, Ho G, Kunth M, Ling B, Lakshmanan A, Lu GJ, Bourdeau RW, Schröder L, Shapiro MG. Recombinantly expressed gas vesicles as nanoscale contrast agents for ultrasound and hyperpolarized MRI. *AIChE Journal* 2018; 64:2927–2933.